What can the reflection of neutrons reveal about the structure of hard and soft condensed matter?

C.F.Majkrzak
Center for Neutron Research
National Institute of Standards and Technology

National School on X-Ray and Neutron Scattering, ORNL, 19 June 2019

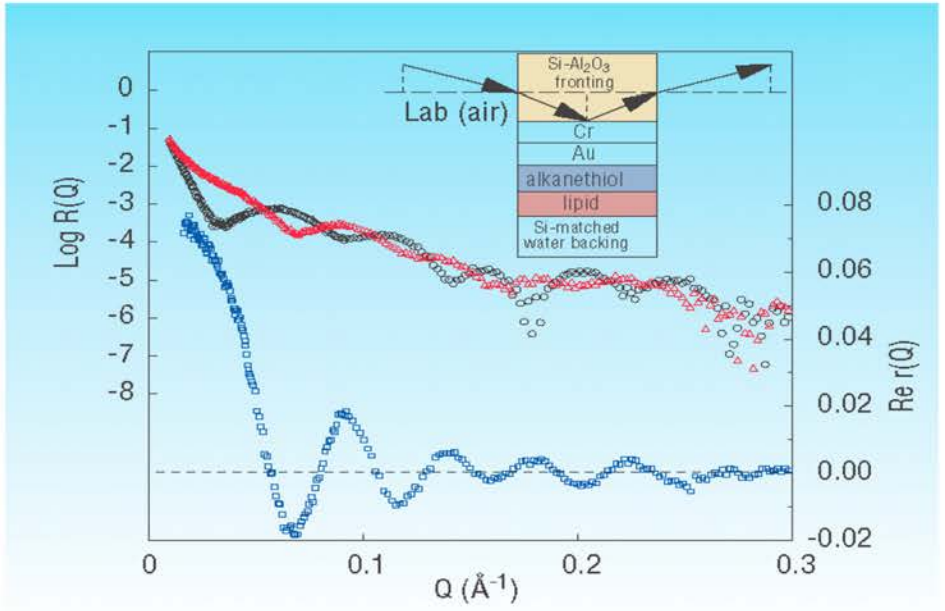

FIGURE 2. Reflectivity curves for the thin film system depicted schematically in the inset, one for a Si fronting (red triangles), the other for Al_2O_3 (black circles). The curve in the lower part of the figure (blue squares) is the real part of the complex reflection amplitude for the films obtained from the reflectivity curves by the method described in the text.

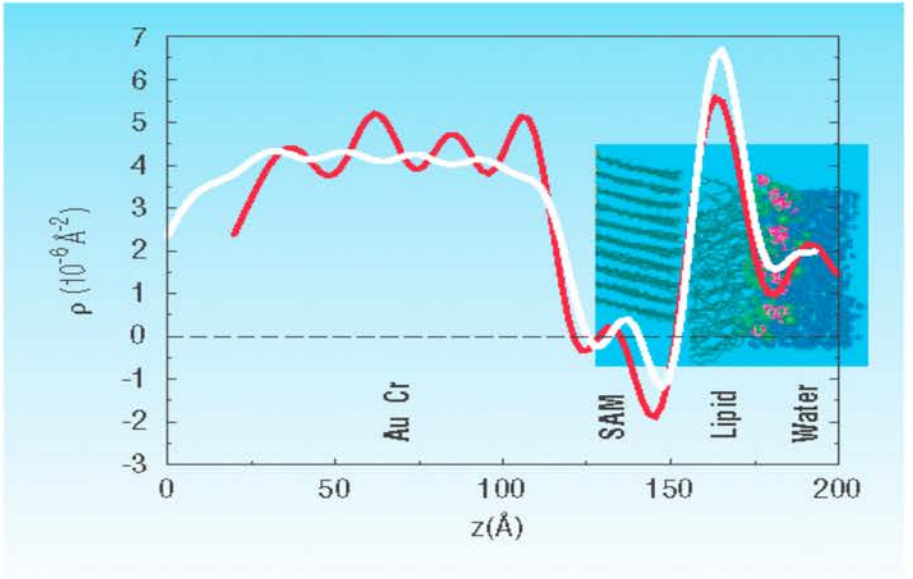

FIGURE 3. SLD profile (red line) resulting from a direct inversion of the Re r of Fig. 2 compared with that predicted by a molecular dynamics simulation (white line) as discussed in the text. The headgroup for the Self-Assembled-Monolayer (SAM) at the Au surface in the actual experiment was ethylene oxide and was not included in the simulation but, rather, modelled separately as part of the Au. Also, the Cr-Au layer used in the model happened to be 20 Å thicker than that actually measured in the experiment.

A common theme – trying to see structure in objects at very small length scales --

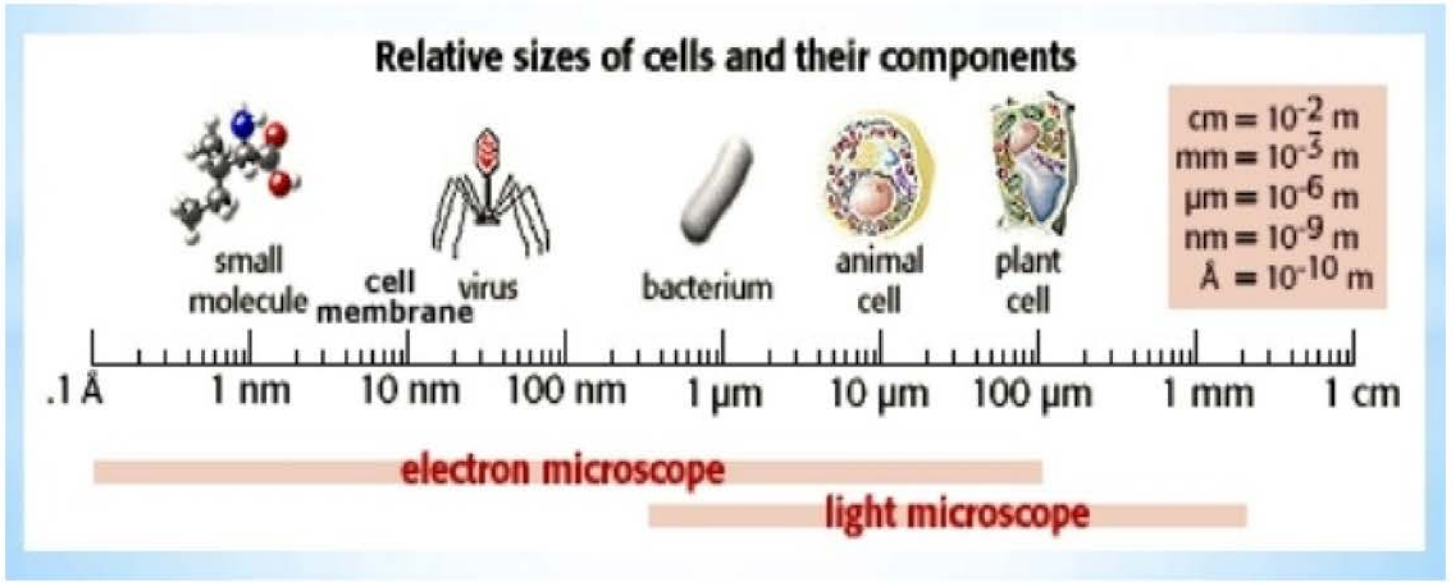

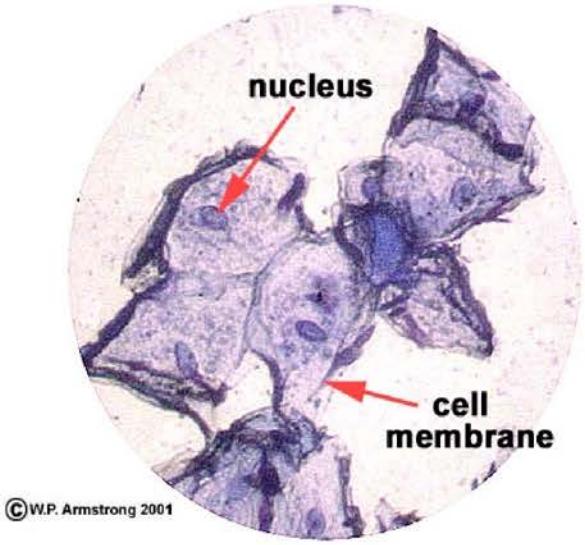

(Wikipedia EM)

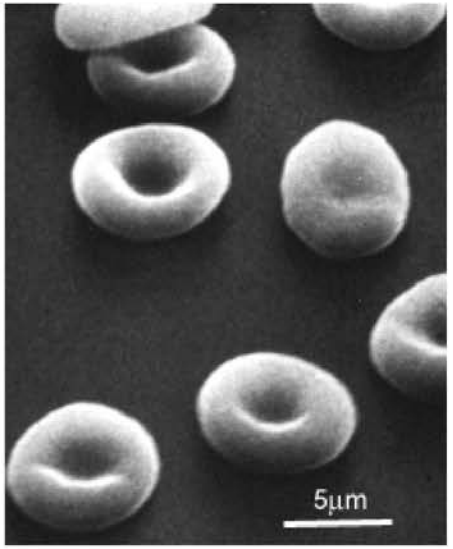

(red blood cells Leeds)

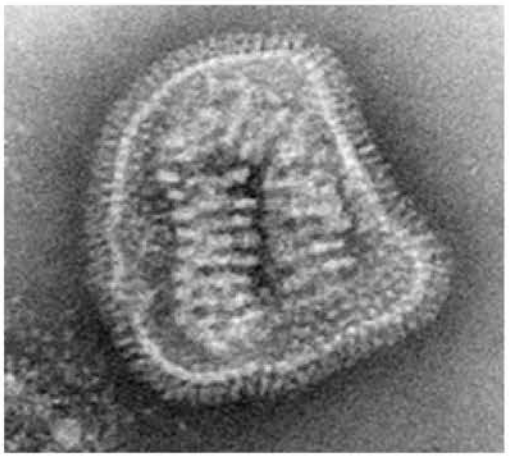

(virus ASU)

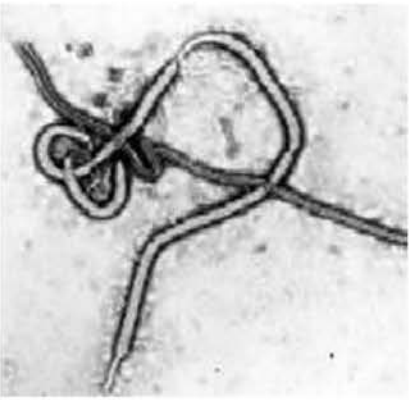

(Ebola UTMB)

From real space images and geometrical optics to wave behavior and diffraction patterns:

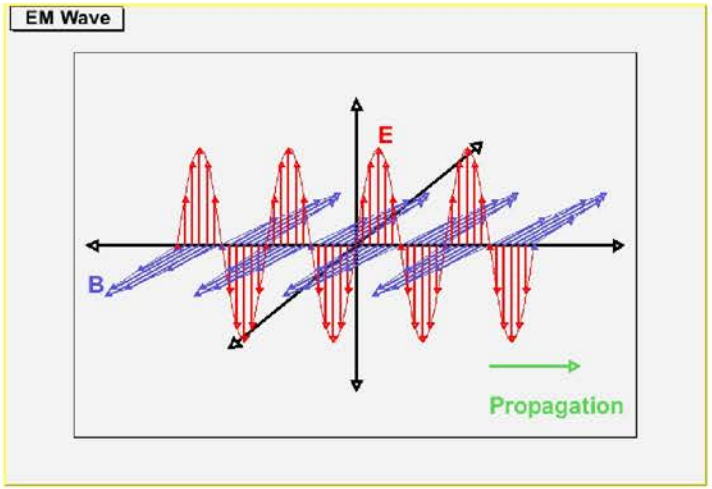

(physics.indiana.edu)

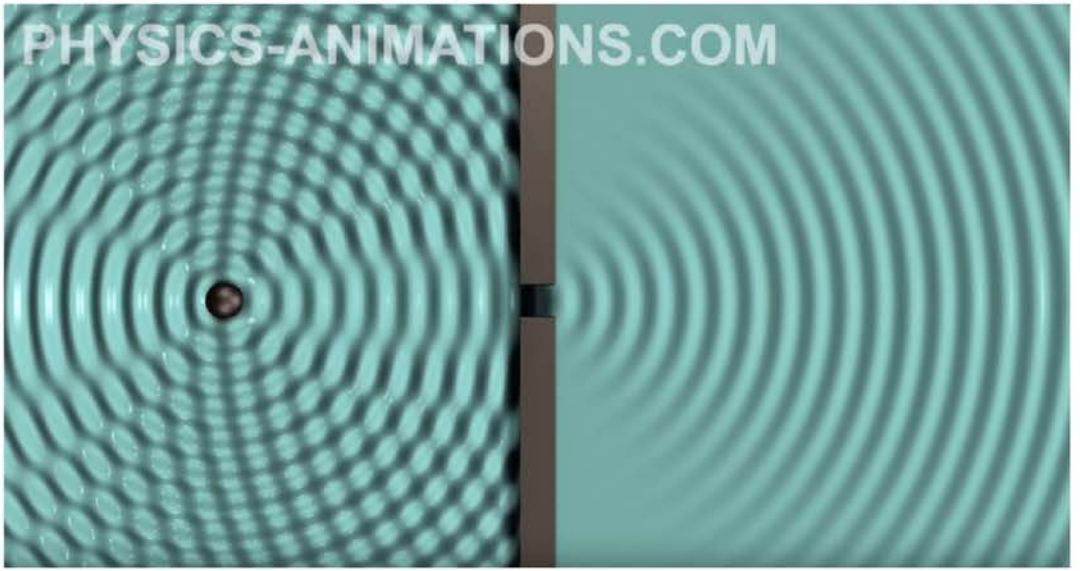

$$r(k) = [4\pi/(i2k_z S)] \int \Psi(\mathbf{k})\, \rho(\mathbf{r})\, e^{i\mathbf{k}\cdot\mathbf{r}}\, d^3r$$

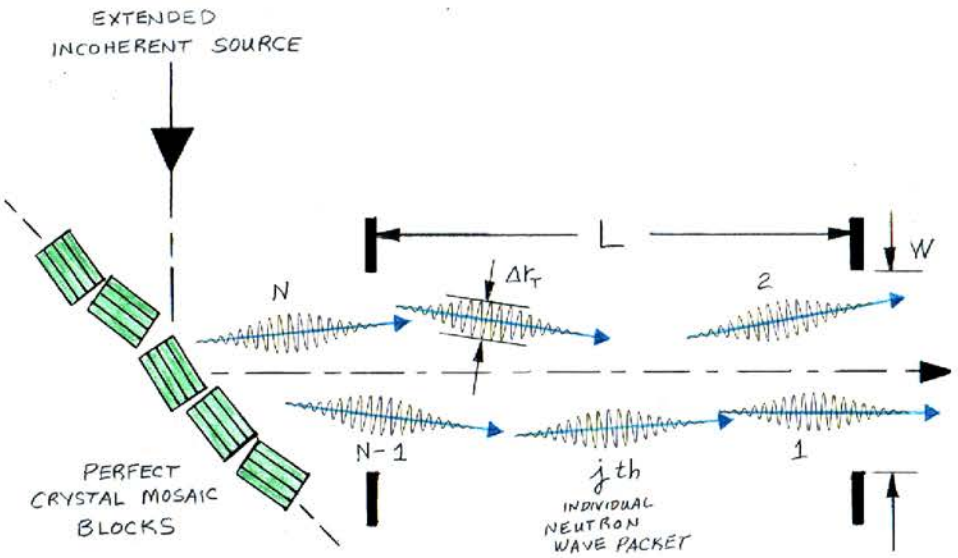

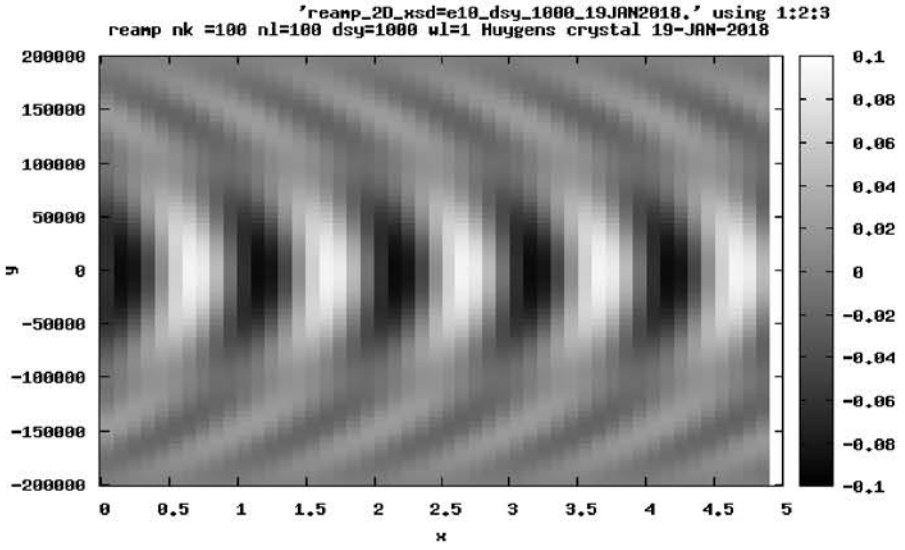

the neutron wave packet – a particle probe with a built-in ruler

Diffraction examples --

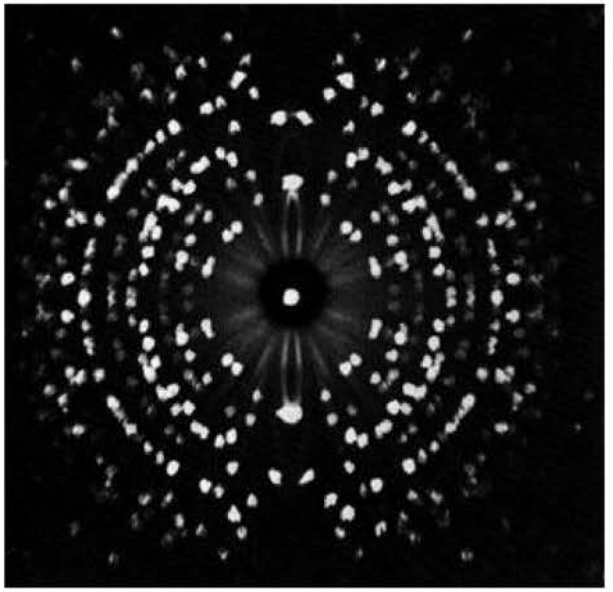

(H.J. Milledge)

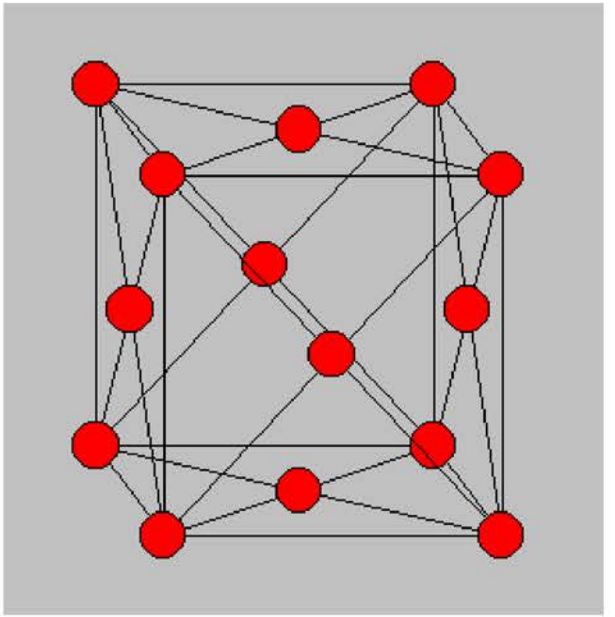

(colorado.edu)

(Pea.Lectin.einstein.cclrc.ac.uk)

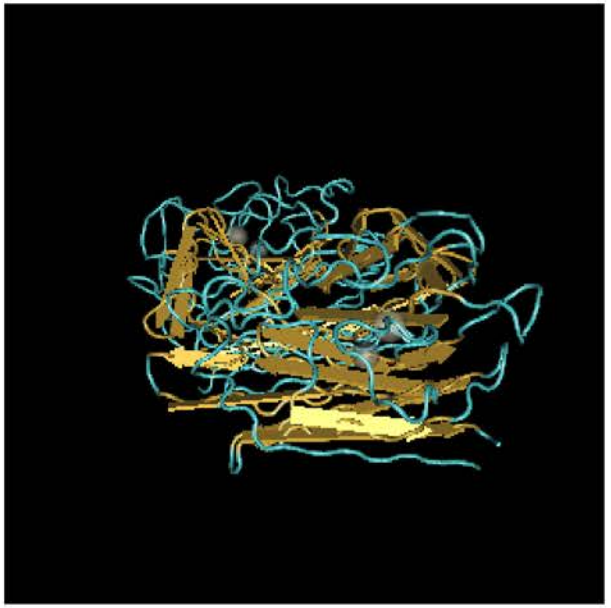

(prasthofer pea lectin)

Neutron Reflectometry and Diffraction from Layered Media

Advances in the preparation of thin films helped create a specialized configuration for elastic neutron diffraction at low momentum transfers from layered matter at glancing angles of incidence – neutron reflectometry. Early work in this area was pioneered by by a number of people at different institutions, including Gian Felcher (ANL), Bob Thomas, Jeff Penfold, Adrian Rennie (Oxford), John Hayter, Giovanna Fragneto (ILL), John White, Bernard Farnoux (Saclay), Jarek Majewski (LANL), Greg Smith, Bill Hamilton and others. For a review of the early history, see, for example, *The application of the specular reflection of neutrons to the study of surfaces and interfaces*, J Penfold and R K Thomas 1990 J. Phys.: Condens. Matter 2 1369, *The Origins of Neutron Reflectometry*, C.F. Majkrzak and J. Penfold, Neutron News Volume 21, Issue 1, 2010, and *Neutron Scattering Studies of Surfaces and Interfaces*, C.F. Majkrzak and G.P. Felcher, MRS Bulletin Volume: 15 Issue: 11 Pages: 65-72 NOV 1990.

<> Fundamentals of the Theory

<> Basic Experimental Methods

<> Practical Applications

- **Soft Condensed Matter**
- **Hard Condensed Matter**

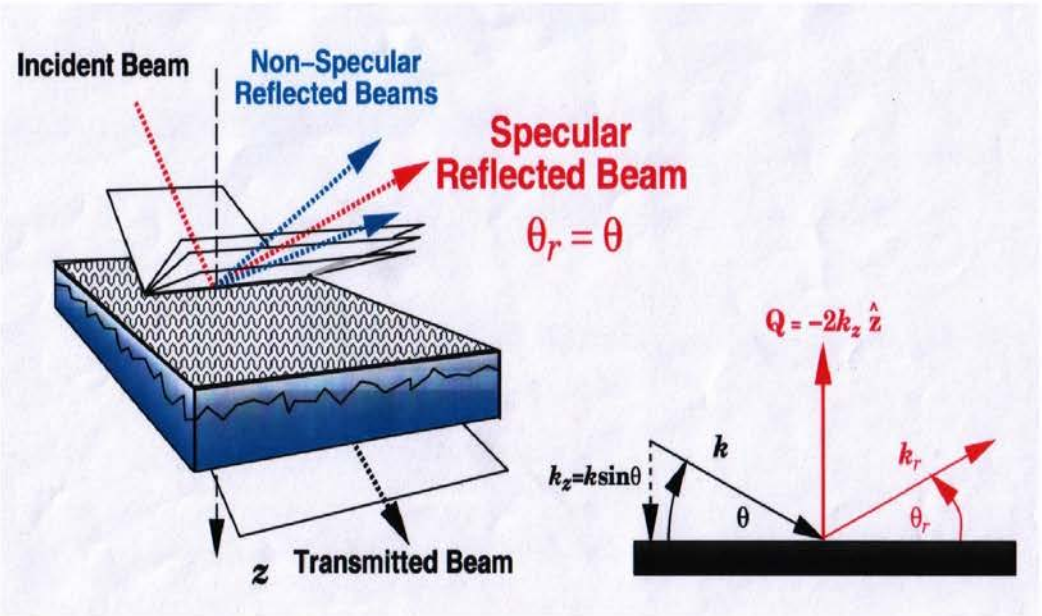

(figure thanks to Norm Berk)

$$\text{Reflectivity} = \frac{\text{Number of reflected neutrons}}{\text{Number of incident neutrons}} = |r|^2$$

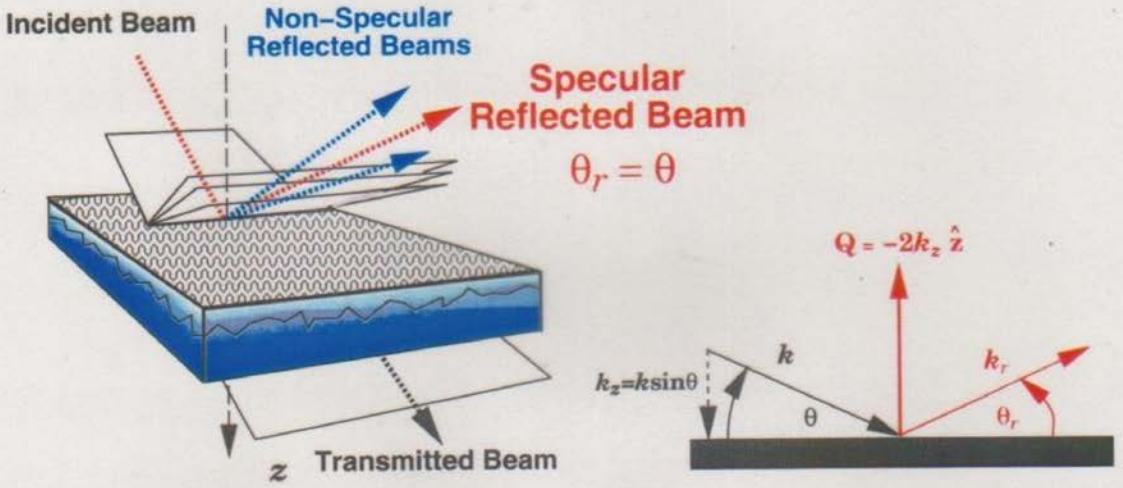

Specular reflection: $\overline{\rho}(z) = \langle \rho(x,y,z) \rangle_{xy}$

Non–Specular reflection: $\Delta\rho(x,y,z) = \rho(x,y,z) - \overline{\rho}(z)$

(AFTER N.F.BERK ET AL.)

Principal Uses and Advantages of Neutron Reflectometry (NR):

* For the specular condition, provides the chemical (isotopic) scattering length density (SLD) depth profile along the surface normal with a spatial resolution approaching half a nanometer.

* With polarized neutrons, provides the *vector* magnetization depth profile of a ferromagnetic material.

* Isotopic contrast, particularly applicable to hydrogen and deuterium.

* A non-destructive probe which can penetrate macroscopic distances through single crystalline substrates, making possible reflection studies of films in contact with liquids within a closed cell.

* As a consequence of the relatively weak interaction between the neutron and material, a remarkably accurate theoretical description of the reflection process and quantitative analysis of the data is possible, although the Born approximation is often not valid and an “exact” or “dynamical” formulation is required.

* NR is an established probe of the nanometer scale structure of both hard and soft condensed matter lamellar systems of interest in physics, chemistry, biology, and polymer and materials science

Why is specular neutron reflectometry so special?

<> Neutron reflectometry (NR) is a valuable probe of the structure of both hard and soft condensed matter in thin film or multilayered form -- particularly for hydrogenous and magnetic materials. NR can see *beneath* the surface and provide quantitative structural information from *everywhere within* the film on a nanometer scale.

<> Both “forward” and “inverse” scattering problems for specular neutron reflection are mathematically solvable, exactly, from first-principles quantum theory. The mathematically unique solutions are thus far only possible in one dimension and for non-absorbing potentials of finite extent.

<> Phase-sensitive neutron specular reflectometry, employing references, enables direct inversion of composite reflectivity data sets to yield a unique scattering length density depth profile for an “unknown” film of interest, without fitting or any adjustable parameters.

<> The spatial resolution and accuracy of the SLD profile thereby obtained is limited only by the statistical uncertainty in the measured reflected intensities and truncation of the reflectivity data sets at the maximum value of wavevector transfer attainable.

Importance of Sample System Preparation

> The great success in using neutron reflection/diffraction to study thin film systems of hard condensed matter, in particular the structures and fundamental interactions in magnetic materials, is largely due to the ability to tailor, with atomic-layer accuracy and precision, single-crystalline, layered sandwiches and superlattices (using vapor deposition techniques such as molecular beam epitaxy in ultra-high vacuum). Advances in film deposition techniques and lithography continue at a remarkable rate.

> Similarly, neutron reflectometry in principle can be applied as a probe to further our understanding of the structure and function of molecules in lipid membranes, of relevance in biology and bioengineering, when comparable control over the fabrication of model systems is achieved. Great progress has been made toward realizing this goal in practice. However, we are still at a relatively early stage of development in our ability to engineer soft condensed matter films on atomic and nanometer scales. Progress can be expected as efforts in creating and manipulating membrane / molecular systems accelerates.

> Employing phase-sensitive methods in reflectivity measurements ensures a unique scattering length density (SLD) depth profile. Additional application of hydrogen / deuterium substitution techniques and comparison with molecular dynamics calculations assures a correspondingly high degree of certainty of obtaining an unambiguous chemical composition depth profile.

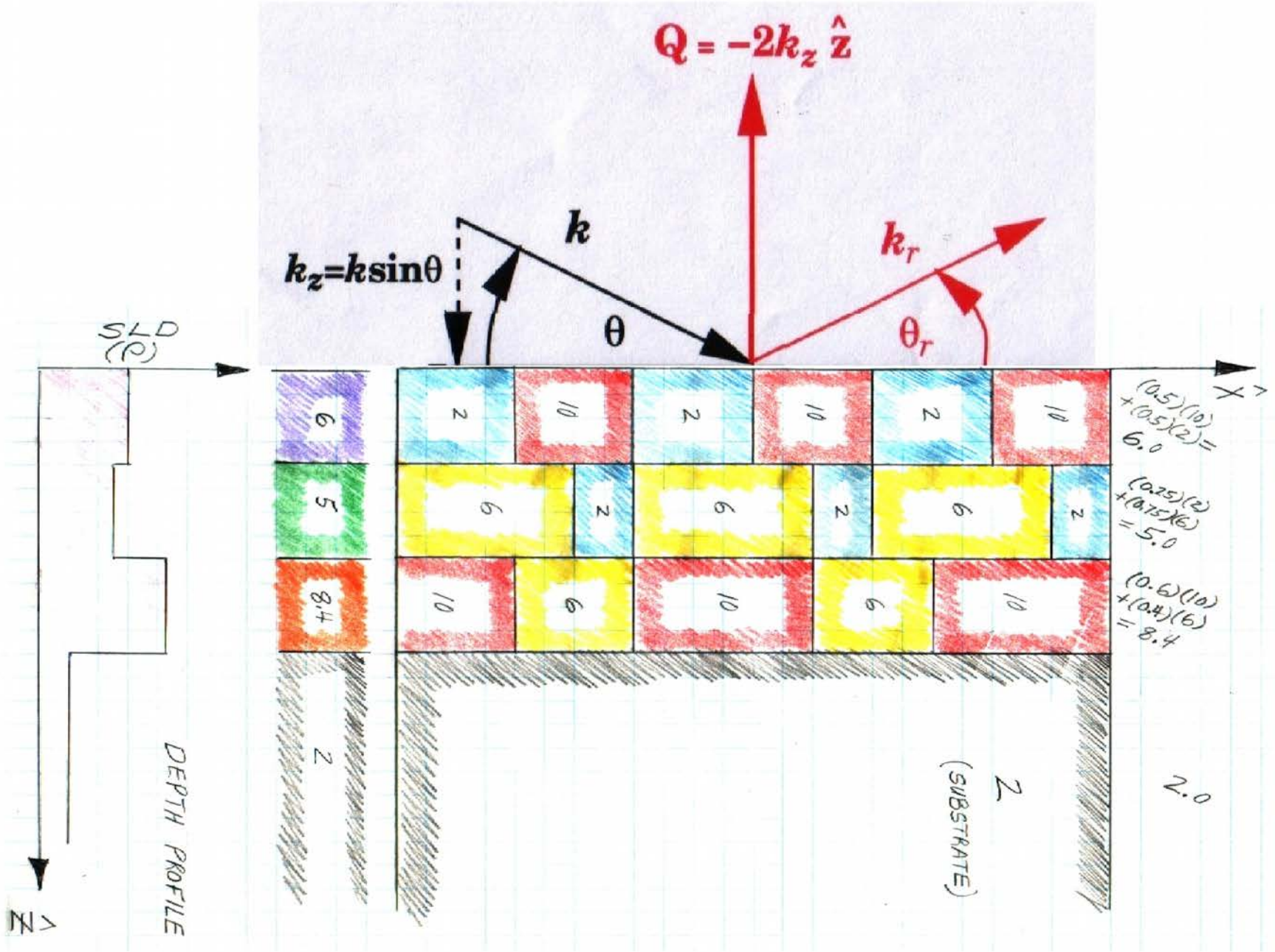

Averaging of the scattering length density (SLD) in the plane of a layer perpendicular to the wavevector transfer (Q) occurs for the specular reflection condition $\theta = \theta_r$.

What a neutron reflectometer (in the specular mode) probes

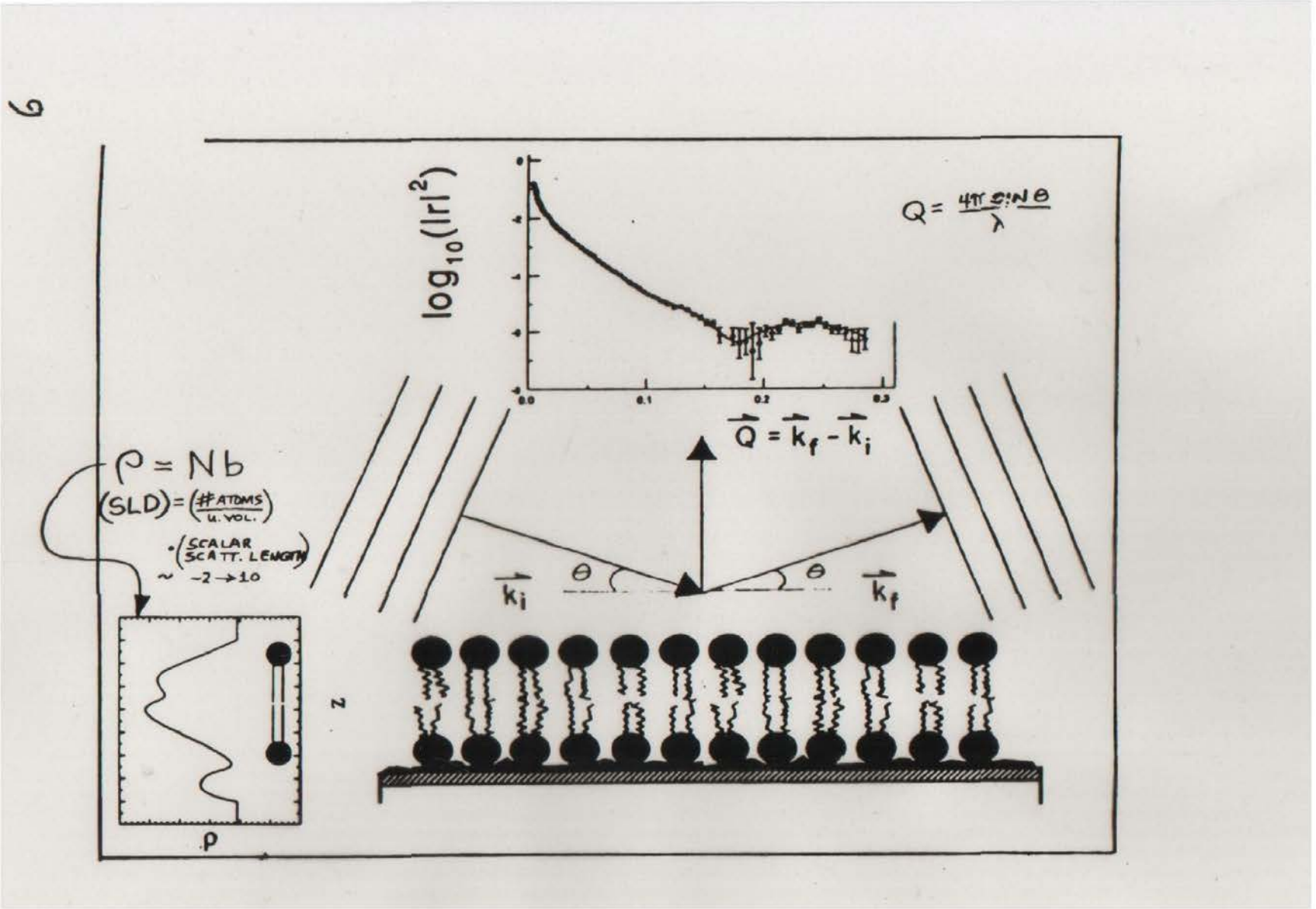

The specular reflection paradigm -- deducing the (in-plane average) scattering length density (SLD) depth profile along the surface normal from reflected intensity measured as a function of Q.

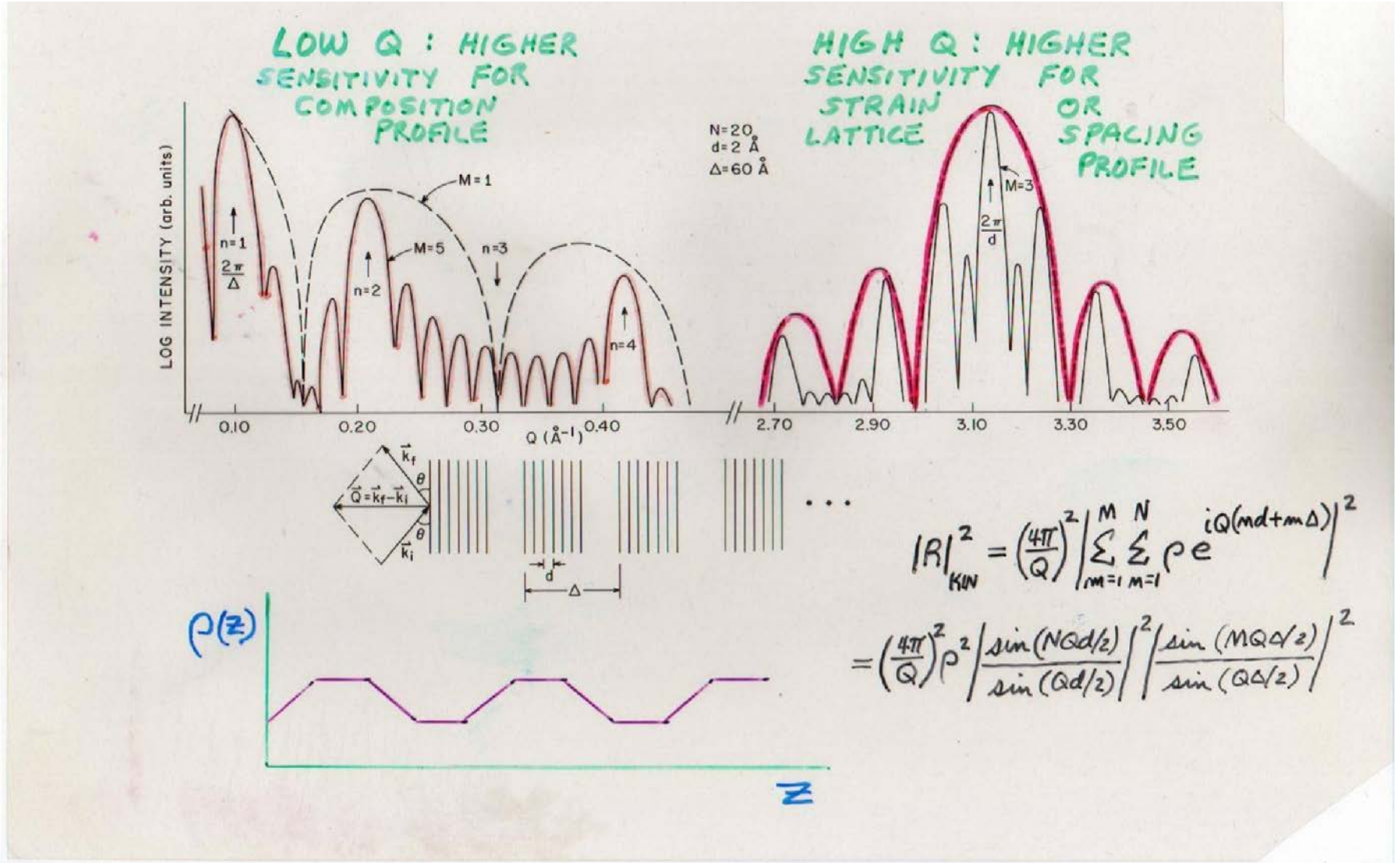

$$|R|^2_{KIN} = \left(\frac{4\pi}{Q}\right)^2 \left| \sum_{m=1}^{M} \sum_{n=1}^{N} \rho e^{iQ(nd+m\Delta)} \right|^2$$

$$= \left(\frac{4\pi}{Q}\right)^2 \rho^2 \left| \frac{\sin(NQd/2)}{\sin(Qd/2)} \right|^2 \left| \frac{\sin(MQ\Delta/2)}{\sin(Q\Delta/2)} \right|^2$$

Specular reflectivity measurements are conventionally taken to mean elastic diffraction over a region of sufficiently low values of Q that sensitivity to structure at inter-atomic length scales is insignificant. Continuing a specular scan to high enough Q eventually allows the interatomic structure of, say, a superlattice to be revealed.

IN THE CONTINUUM LIMIT

$$V(\vec{r}) = \frac{2\pi\hbar^2}{m} \sum_{j=1} N_j b_j = \frac{2\pi\hbar^2}{m} \rho$$

N_j: NUMBER OF ATOMS OF TYPE j PER UNIT VOLUME

b_j: COHERENT SCATTERING LENGTH OF ATOM j —

$$b = \underbrace{\mathrm{Re}\,b}_{\text{SCATTERING}} + i\,\underbrace{\mathrm{Im}\,b}_{\text{ABSORPTION}}$$

ρ: SCATTERING LENGTH DENSITY (SLD)

IN VACUUM

$$E_0 = \frac{\hbar^2 k_0^2}{2m} + 0$$

IN A MATERIAL MEDIUM

$$E = \frac{\hbar^2 k^2}{2m} + \frac{2\pi\hbar^2}{m}\rho$$

CONSERVATION OF ENERGY REQUIRES $E_0 = E$

SO THAT

$$k^2 = k_0^2 - 4\pi\rho$$

& THEREFORE

$$\boxed{[\nabla^2 + k^2]\Psi = 0}$$

CAN THEN DEFINE A REFRACTIVE INDEX $n \equiv \frac{k}{k_0}$

OR

$$\boxed{n^2 = 1 - \frac{4\pi\rho}{k_0^2}}$$

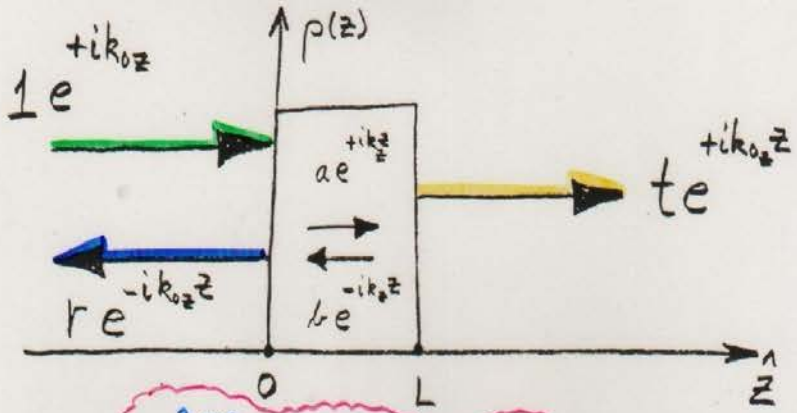

$$\frac{\partial^2 \psi(z)}{\partial z^2} + k_z^2 \psi(z) = 0$$

CONSERVATION OF MOMENTUM AND PARTICLE NUMBER REQUIRE THAT $\psi(z)$ AND $\frac{\partial \psi(z)}{\partial z}$ BE CONTINUOUS AT THE BOUNDARIES $z=0$ & $z=L$

$$\begin{pmatrix} t \\ it \end{pmatrix} e^{ik_{0z}L} = \begin{pmatrix} A & B \\ C & D \end{pmatrix} \begin{pmatrix} 1+r \\ i(1-r) \end{pmatrix}$$

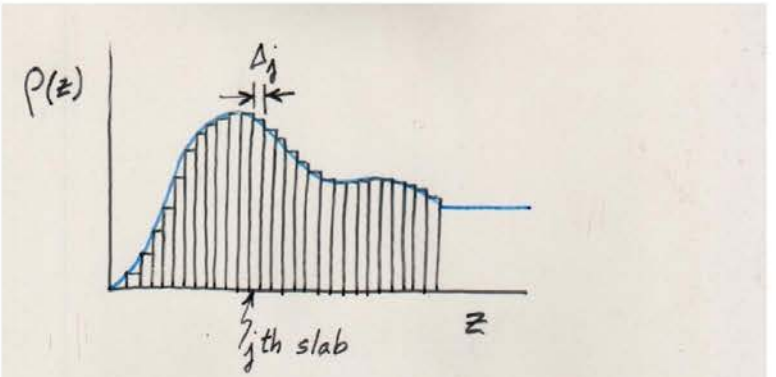

$$\begin{pmatrix} A & B \\ C & D \end{pmatrix} = \begin{pmatrix} a_N & b_N \\ c_N & d_N \end{pmatrix} \begin{pmatrix} a_{N-1} & b_{N-1} \\ c_{N-1} & d_{N-1} \end{pmatrix} \cdots \begin{pmatrix} a_2 & b_2 \\ c_2 & d_2 \end{pmatrix} \begin{pmatrix} a_1 & b_1 \\ c_1 & d_1 \end{pmatrix}$$

$$\begin{pmatrix} a_j & b_j \\ c_j & d_j \end{pmatrix} = \begin{pmatrix} \cos\delta_j & \frac{1}{m_{z_j}} \sin\delta_j \\ -m_{z_j} \sin\delta_j & \cos\delta_j \end{pmatrix}$$

$$\delta_j = k_{0z} m_{z_j} \Delta_j$$
$$= k_{z_j} \Delta_j$$

The elements A, B, C, and D of the so-called "transfer" matrix which relates the reflection, transmission, and incident wave amplitudes -- r, t, and 1, respectively -- contain all of the information about the SLD composition of the film. The transfer matrix can be constructed of a product of matrices, each of which corresponds to one successive "slice" of the film over which the SLD is taken to be a constant value. Thus, any arbitrary profile can be rendered -- and to whatever spatial resolution is needed by making the thicknesses of the slices small enough.

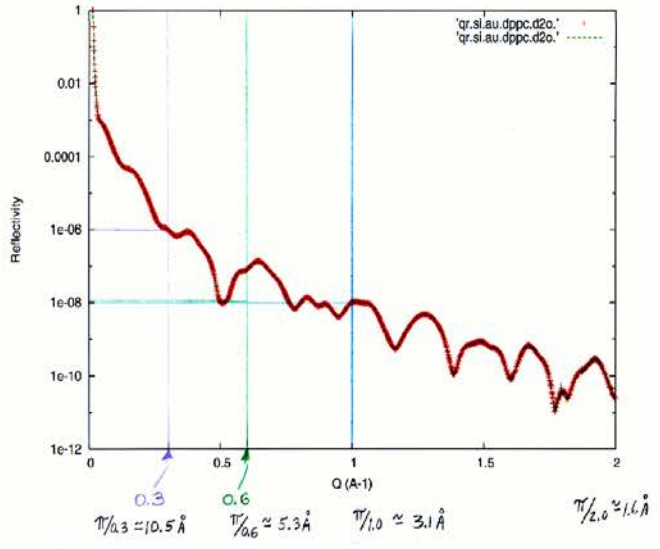

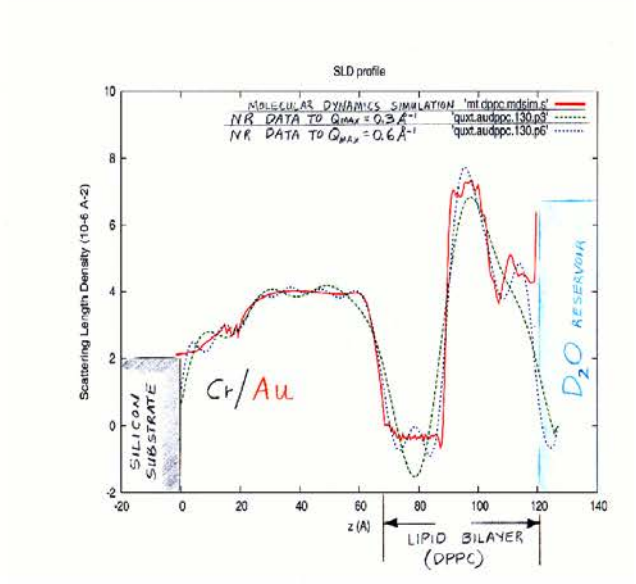

Illustration of the inverse relationship between the maximum value of Q up to which the reflectivity is measured and the spatial resolution in the corresponding SLD depth profile. Resolving smaller features in the profile in real space requires collecting reflectivity data up to larger values of Q in reciprocal space. The statistical accuracy in the measured reflectivity also affects the level of uncertainty in the associated SLD profile model to which the reflectivity data are fit.

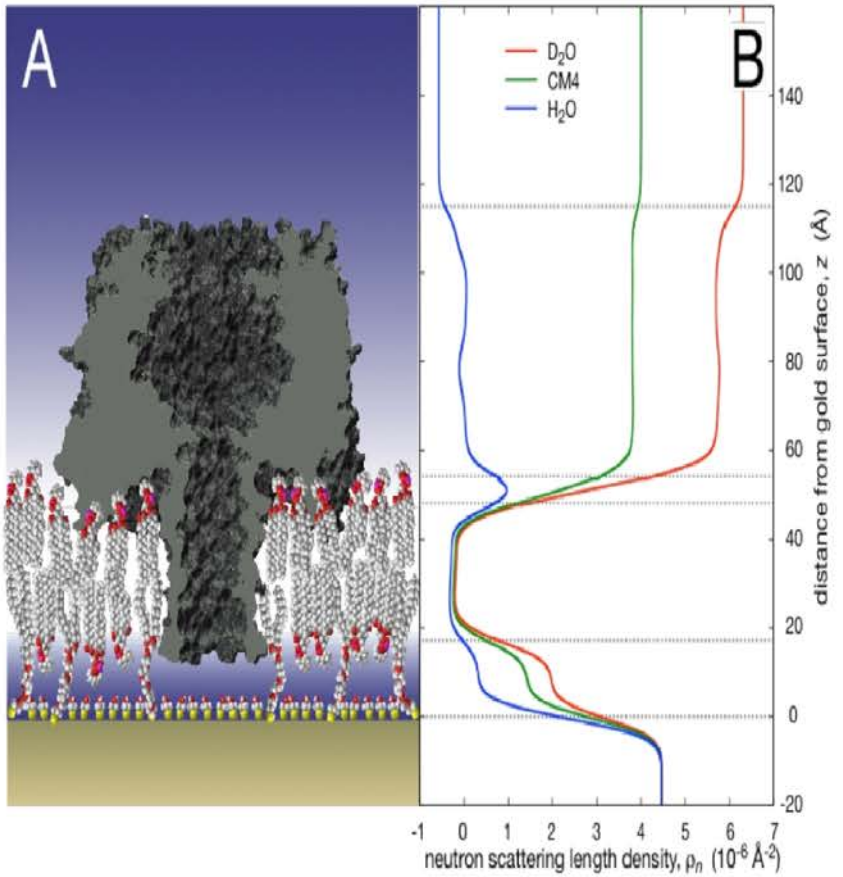

Molecular sketch of alpha-hemolysin channel in a tethered bilayer lipid membrane as deduced from NR measurements the (left) with corresponding scattering length density profile (right) [10].

[10] D.J. McGillivray, G. Valincius, F. Heinrich, J.W.F. Robertson, D.J. Vanderah, W. Febo-Ayala, et al., Structure of functional Staphylococcus aureus alpha-hemolysin channels in tethered bilayer lipid membranes, Biophys J. **96** (2009) 1547–1553.

Polarized Neutrons

<> a magnetic moment arises from the motion of electrical charges -- though neutral, a neutron is composed of charged quarks which give rise to a net magnetic dipole moment which is quantized with corresponding spin 1/2 -- a neutron is a Fermion

<> if it exists at all, any neutron electric dipole moment is of negligible magnitude for all practical purposes of concern to us here

<> a neutron can be represented by a spinor wave function having two components corresponding to two spin eigen-states (spin “+” or “up” and “-” or “down”)

<> for a nucleus with spin, the neutron-nucleus (i.e., the *nuclear*) interaction is spin-dependent

<> the *magnetic* interaction between the neutron magnetic moment and that of a *nuclear* magnetic moment is relatively weak (and nuclear magnetic moments are normally not ordered -- a notable exception occurring in a 3He gas cell used as a neutron polarizer)

<> the *magnetic* interaction between the neutron magnetic moment and that of an atomic magnetic moment, on the other hand, can be comparable to the nuclear interaction

(a good description of the phenomenon of a quantized spin one-half system is given in the quantum mechanics text by Merzbacher)

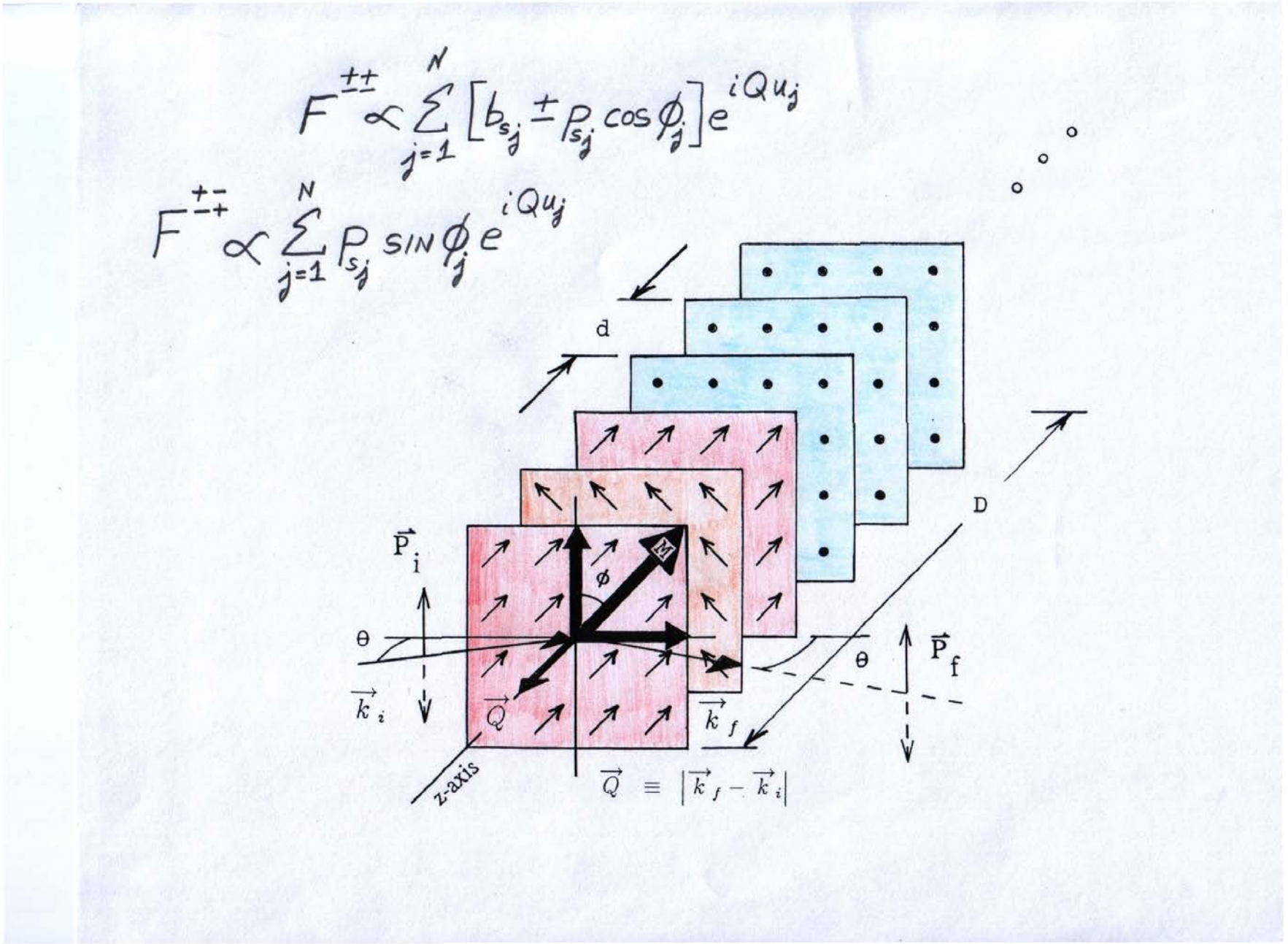

The above diagram illustrates a particularly useful configuration resulting in the ability to determine not only the magnitude of the net magnetization in each of the successive planes in a layered material, but also the direction of that magnetic moment.

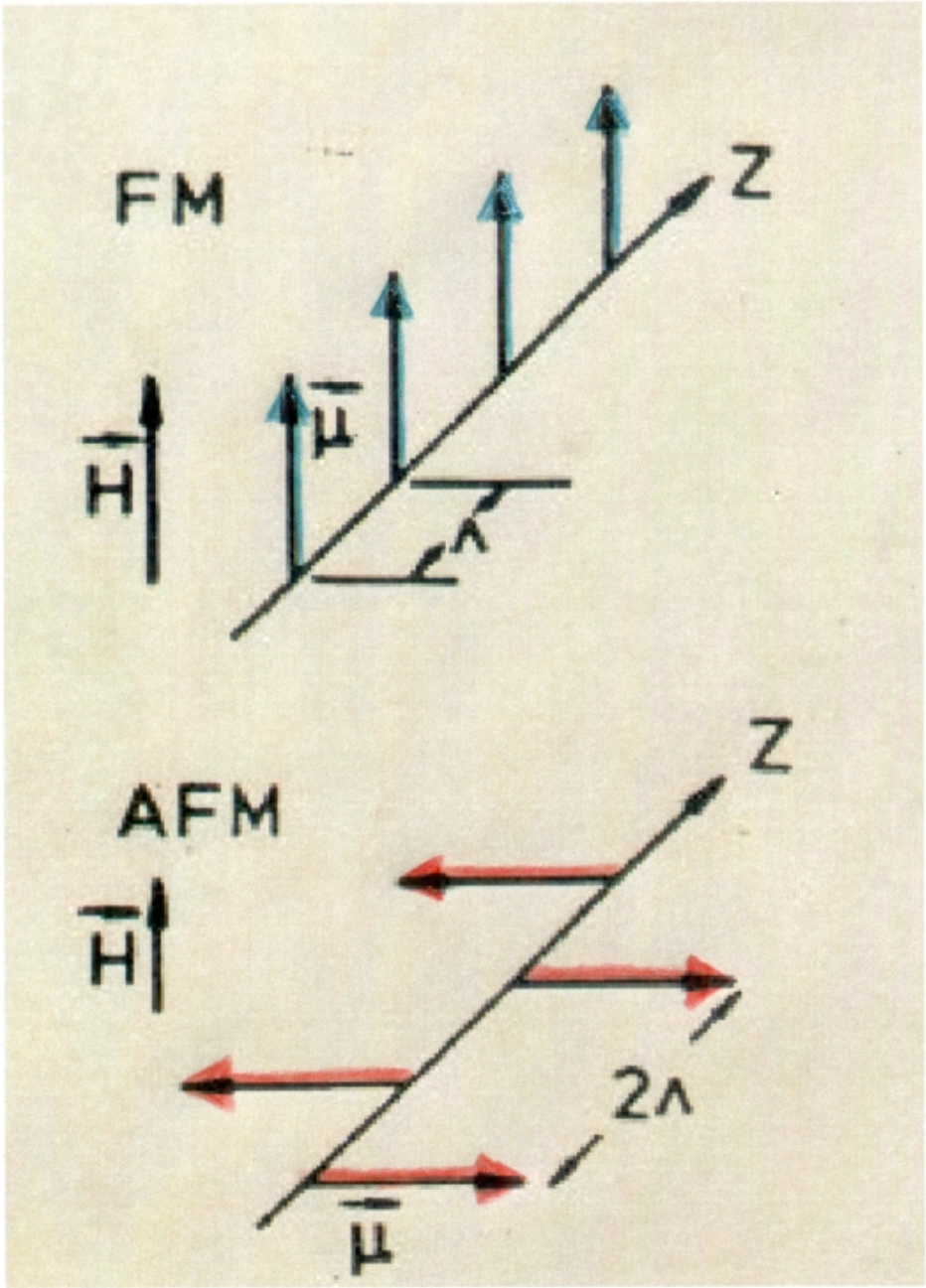

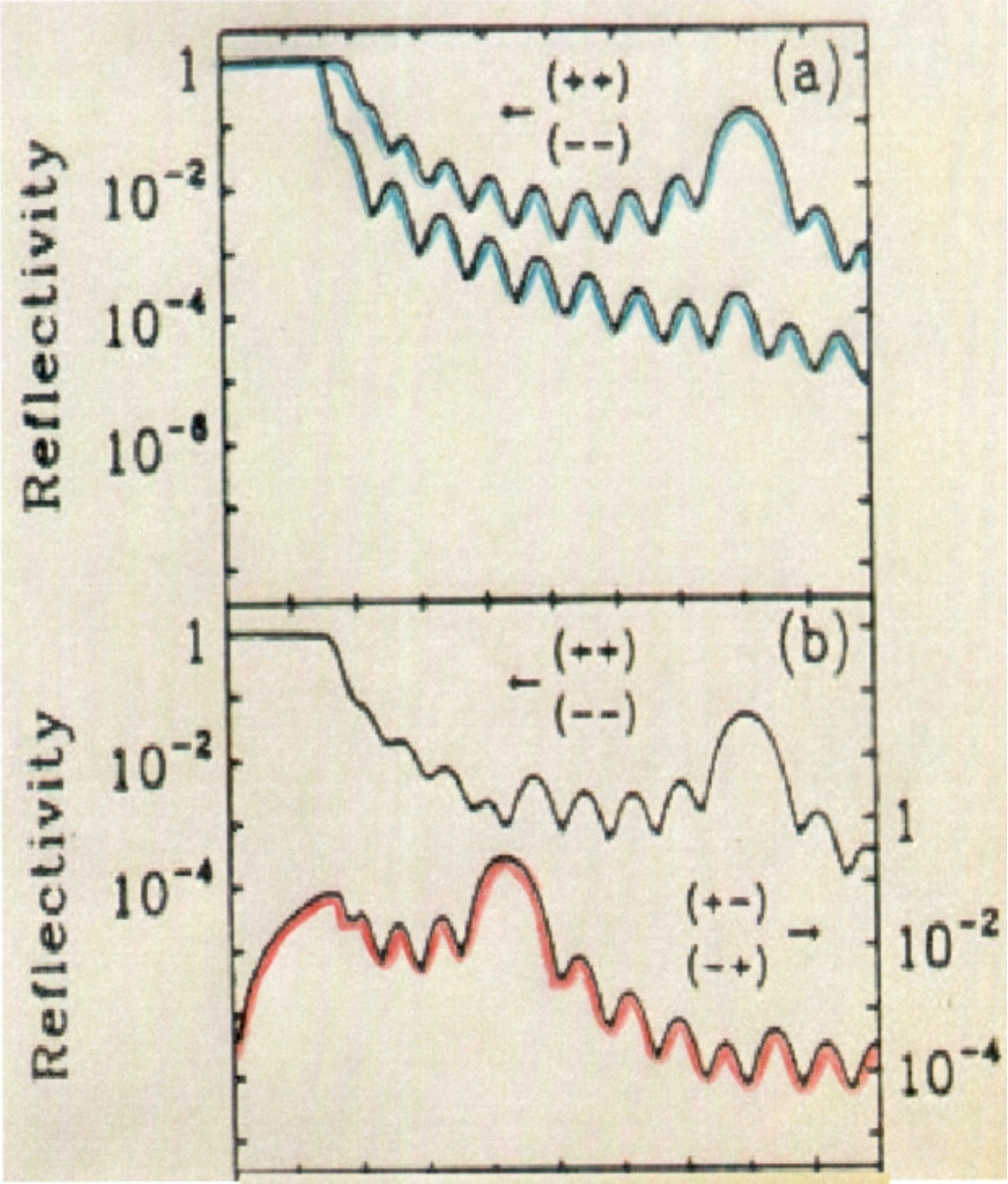

Two basic magnetic structures and their corresponding spin-dependent polarized neutron reflectivity curves (after Ankner, Schreyer, Majkrzak, and Zabel).

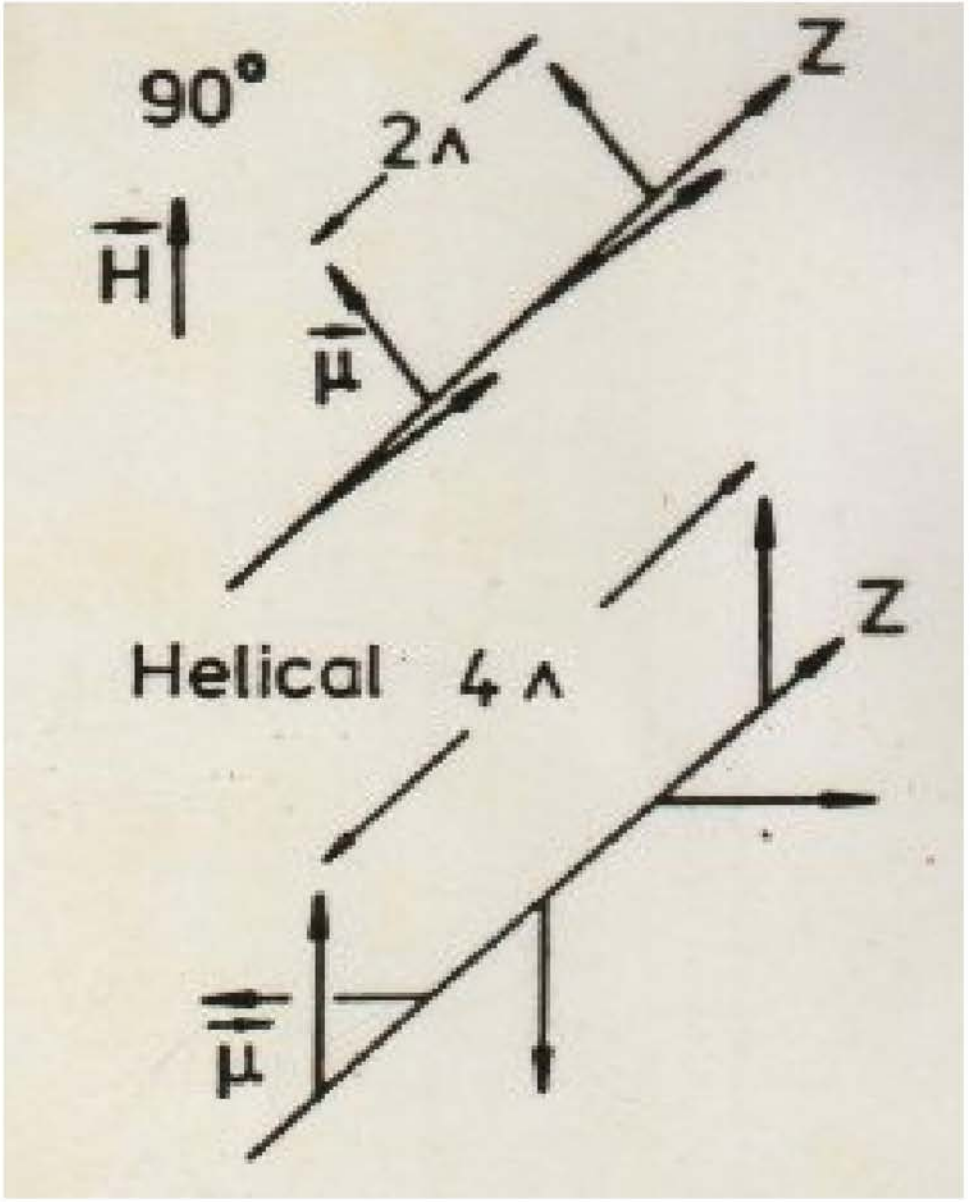

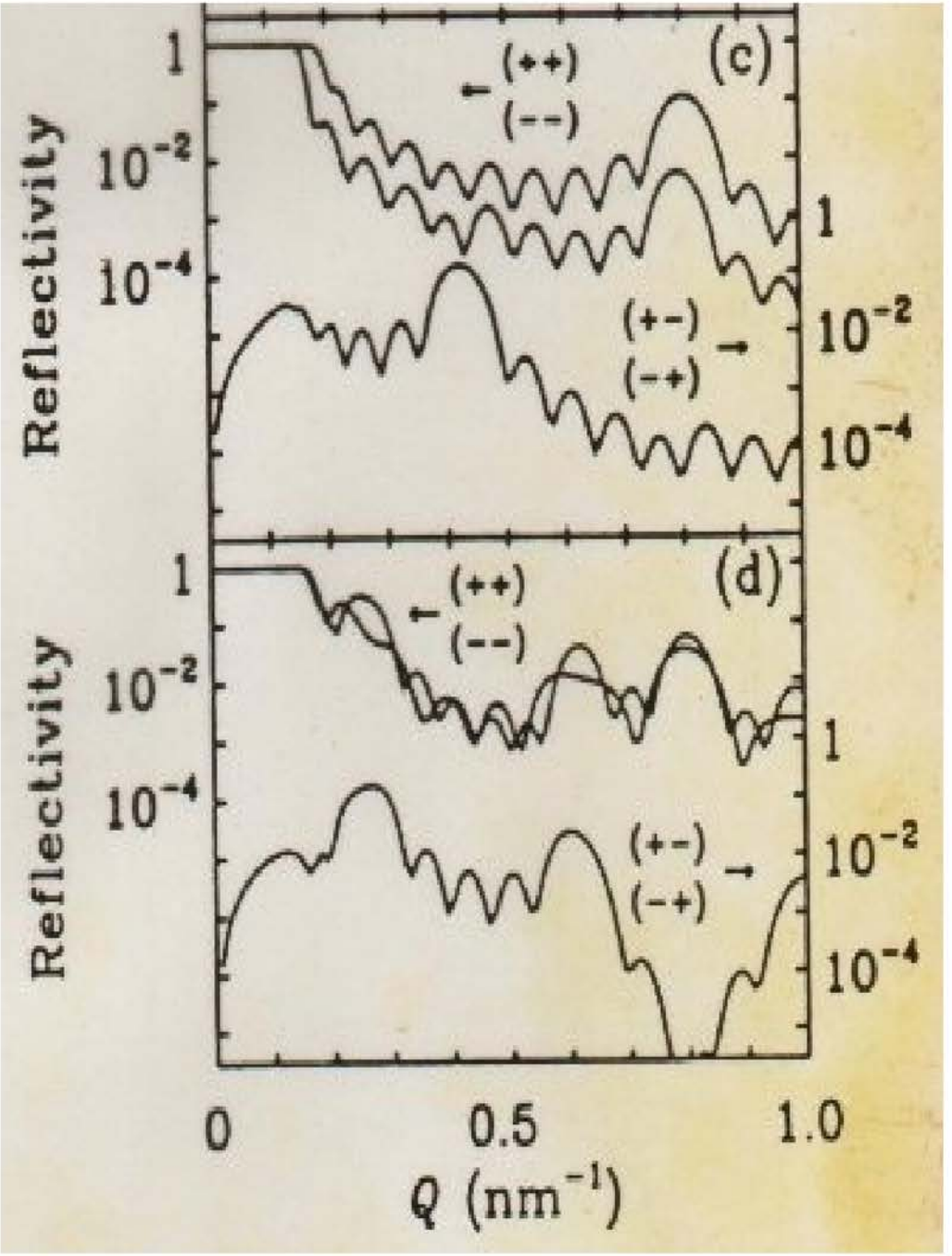

Two more magnetic structures and their corresponding spin-dependent polarized neutron reflectivity curves (after Ankner, Schreyer, Majkrzak, and Zabel).

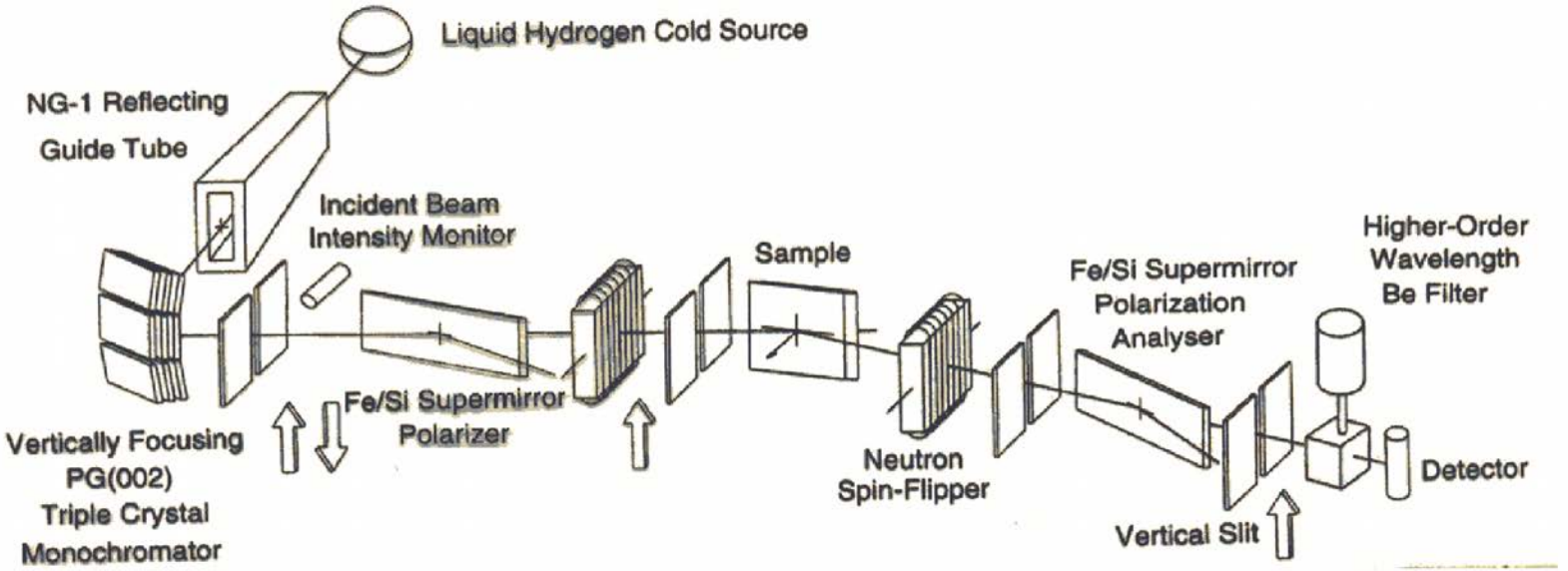
Liquid Hydrogen Cold Source
NG-1 Reflecting
Guide Tube
Incident Beam
Intensity Monitor
Sample
Higher-Order
Wavelength
Be Filter
Fe/Si Supermirror
Polarization
Analyser
Fe/Si Supermirror
Polarizer
Vertically Focusing
PG(002)
Triple Crystal
Monochromator
Neutron
Spin-Flipper
Detector
Vertical Slit

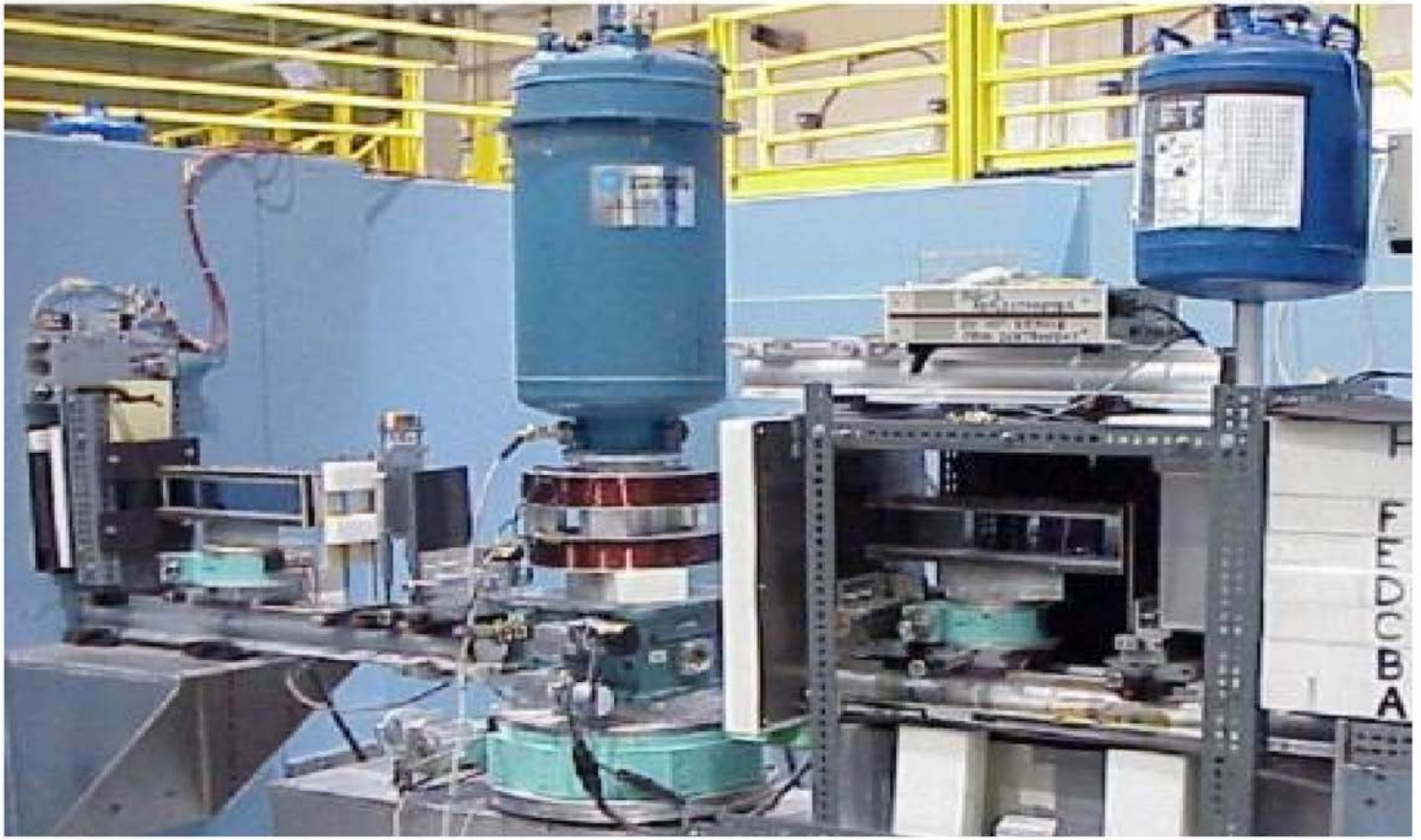

Scientific areas in which neutron reflectometry has been applied at the NCNR
(not necessarily a comprehensive account!)

<> Polymer Science

<> Magnetism

<> Biology

<> Electrochemistry and Photovoltaics

Magnetism


Alex Grutter
E130 x4198


Brian Kirby
E102 x8395


Eric Brok*
B110 x5180


Brian Maranville
E102 x6034


Kathryn Krycka
B107 x8685


Julie Borchers
E105 x6597


Dustin Gilbert
E130.1 x8369

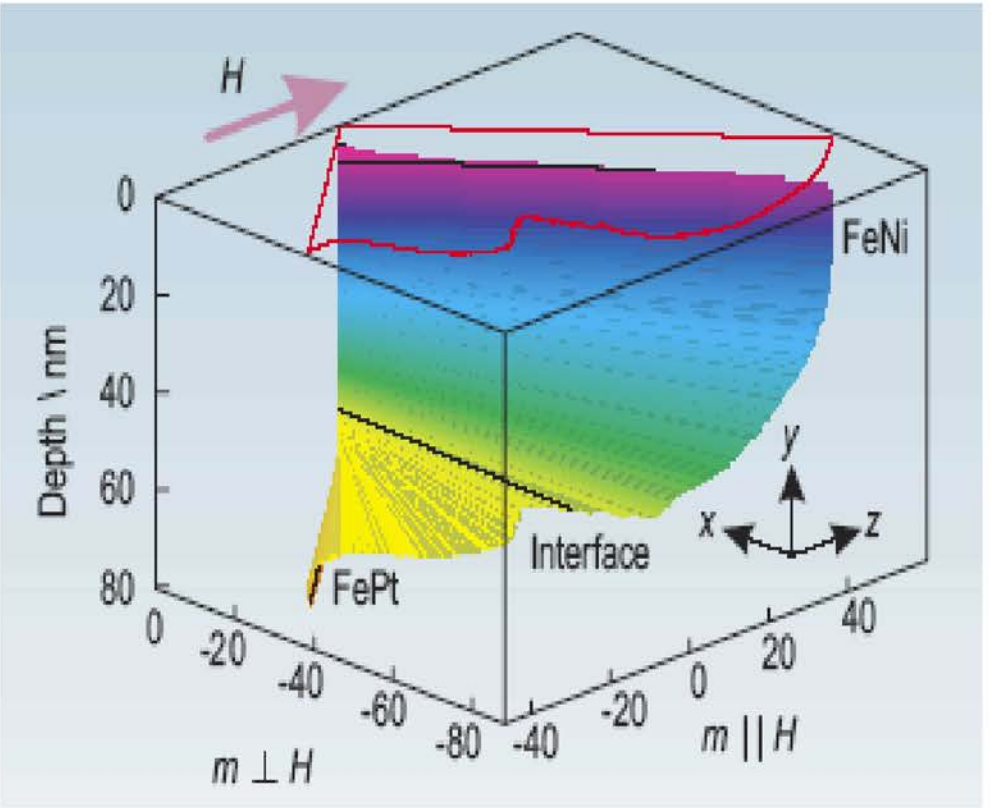

(after O'Donovan et al.)

New directions in science – synthetic superlattices

The same developments in physical vapor deposition methods were also being applied to the fabrication of composite layered systems (in some cases with atomic layer accuracy by molecular beam epitaxy) that do not occur in nature but which could be tailored to study fundamental physical phenomena in a controlled, systematic way.

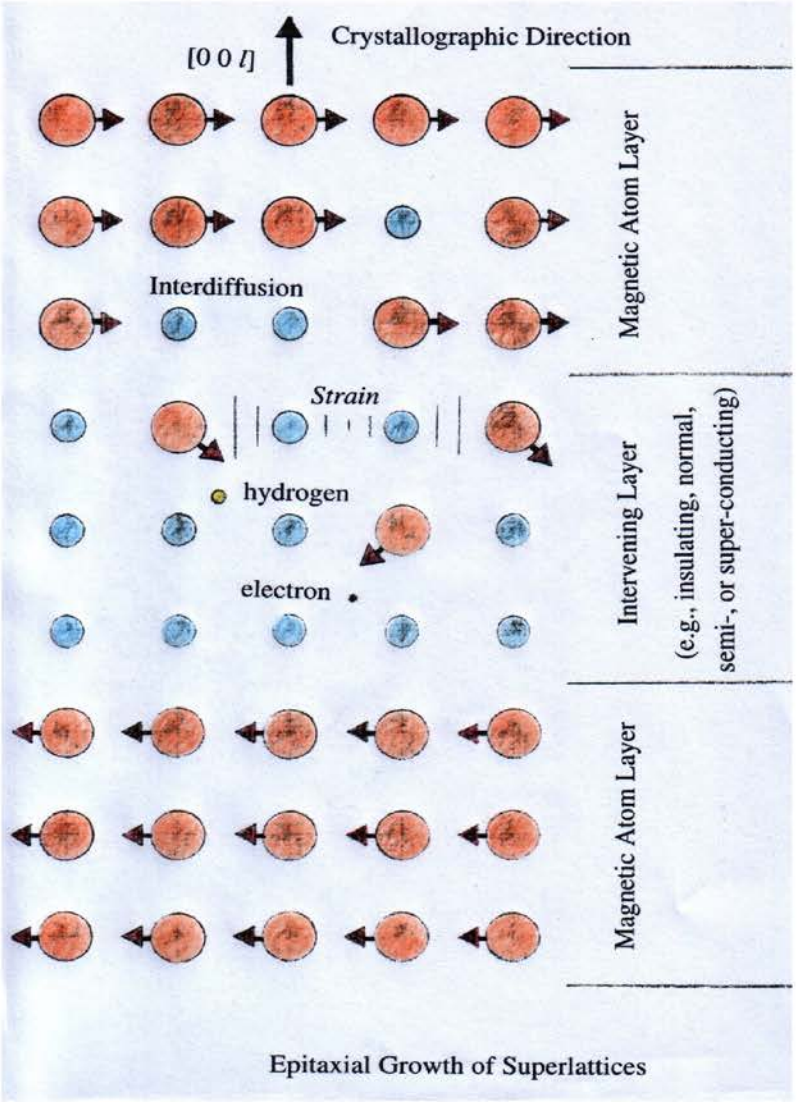

By means of molecular beam epitaxial growth in ultrahigh vacuum and other thin film deposition techniques, it is possible to construct synthetically layered systems tailored to study specific types of interactions of interest in hard condensed matter. For instance, how two separated regions made up of ferromagnetic atomic planes interact with one another across an intervening region of atomic planes of a material that is superconducting or semiconducting can be studied by analysis of the polarized neutron reflectivity -- as a function of temperature, applied magnetic field magnitude and direction, or other parameter such as the thickness of the intervening layer.

There exists a considerable body of work on systems prepared in this manner.

Magnetic structure of unit bilayer

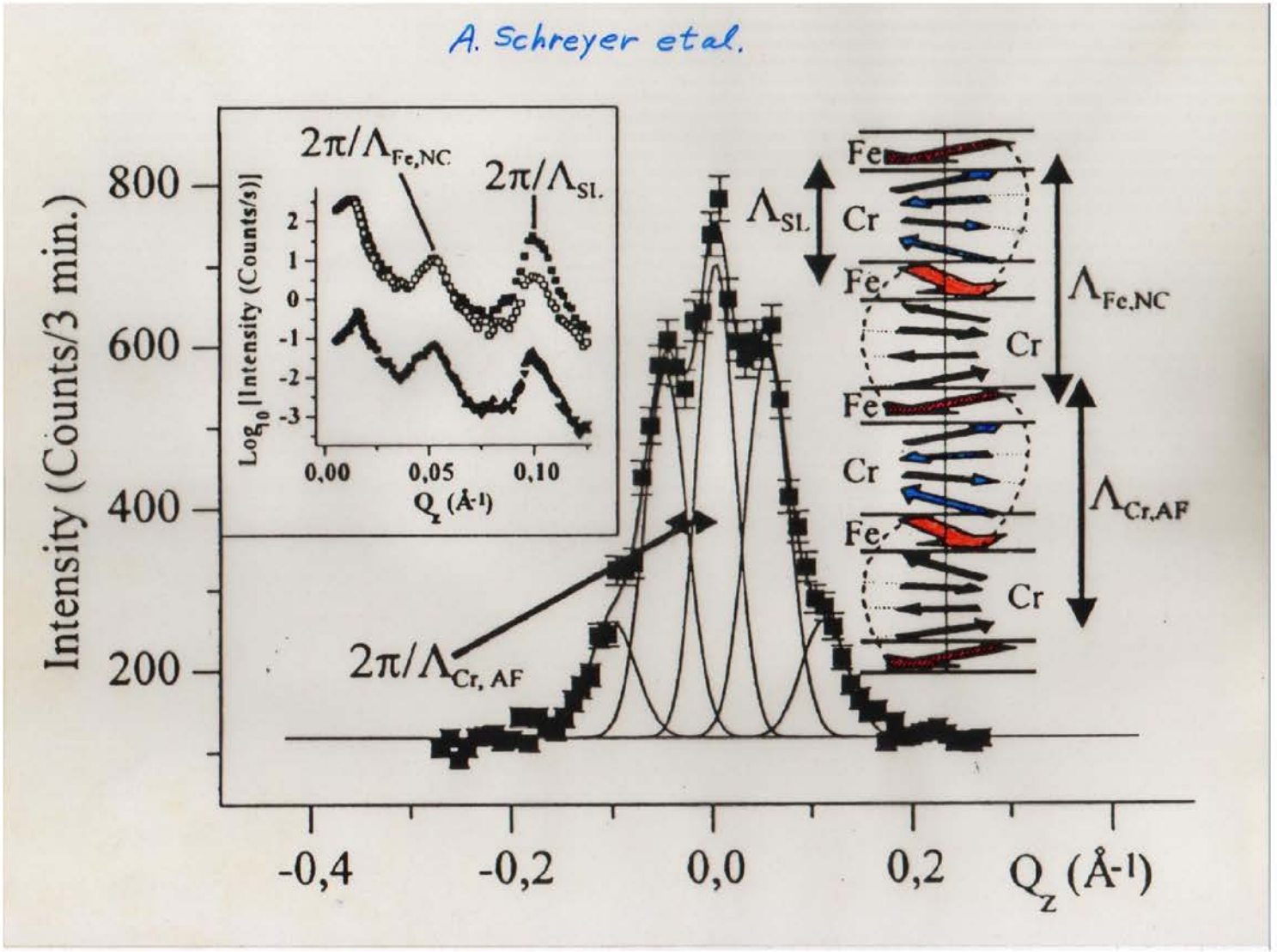

In this particular example, each ferromagnetic Fe layer consists of several atomic planes -- the relative orientations of these layers to one another within the overall layered system is deduced principally from the relatively low-Q polarized neutron reflectivity data (inset). The intricate modulated antiferromagnetic structure of the Cr atomic planes within the intervening layers is revealed primarily in the higher-Q polarized neutron diffraction pattern.

Magnetic multilayers -- interlayer correlation

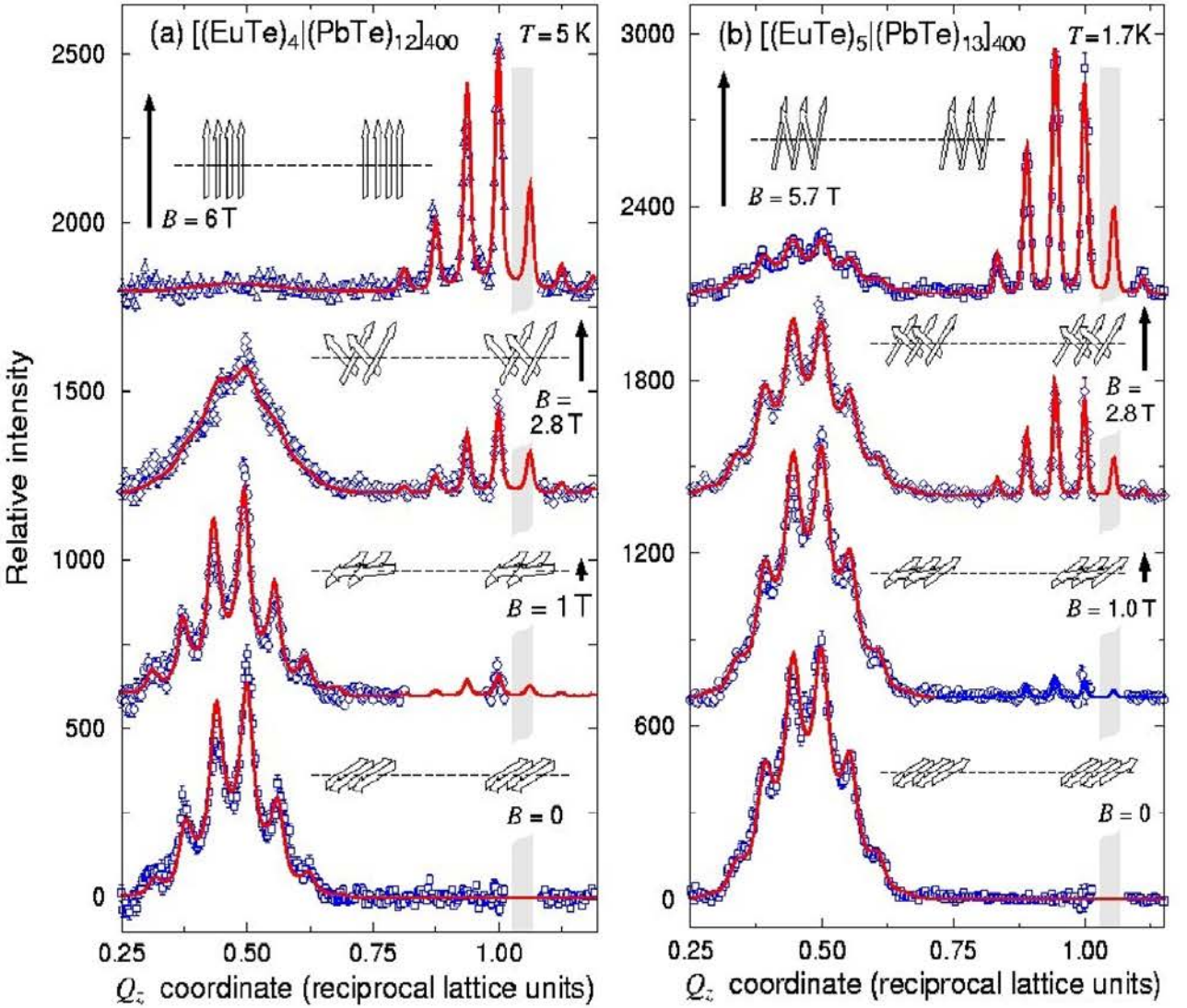

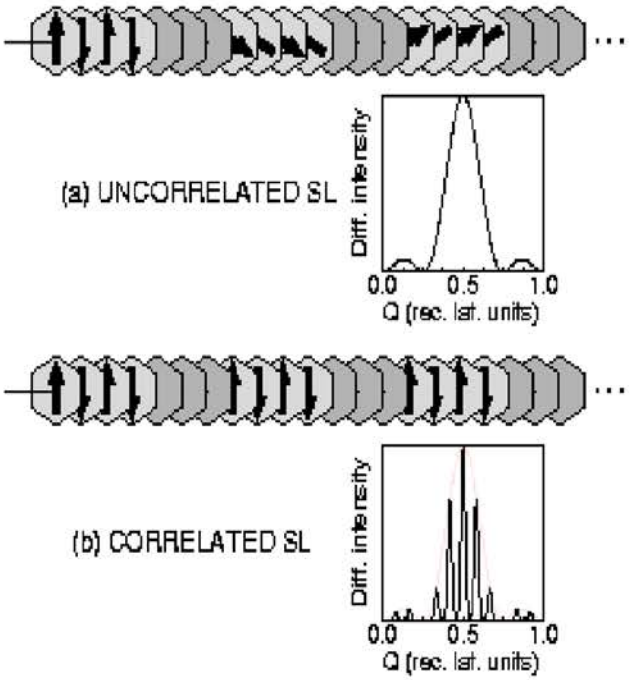

Remarkably detailed information about magnetic structure on an inter-atomic length scale can be obtained from polarized neutron reflection and diffraction studies. (Polarized neutron reflection data on magnetic semiconductor superlattices by Henryk Kepa et al..)

Observation of Antiparallel Magnetic Order in Weakly Coupled Co/Cu Multilayers

J. A. Borchers, J. A. Dura, J. Unguris, D. Tulchinsky, M. H. Kelley, and C. F. Majkrzak
National Institute of Standards and Technology, Gaithersburg, Maryland 20899

S. Y. Hsu, R. Loloee, W. P. Pratt, Jr., and J. Bass
Department of Physics and Astronomy, Michigan State University, East Lansing, Michigan 48824
(Received 16 December 1998)

Polarized neutron reflectivity and scanning electron microscopy with polarization analysis are combined to determine the magnetic structure of Co(6 nm)/Cu(6 nm) multilayers. These data resolve a controversy regarding the low-field state of giant-magnetoresistive (GMR) multilayers with weak coupling. As-prepared samples show a strong antiparallel correlation of in-plane ferromagnetic Co domains across the Cu. At the coercive field, the Co domains are uncorrelated. This irreversible transition explains the decrease in magnetoresistance from the as-prepared to the coercive state. For both states, the Co moments reside in domains with in-plane sizes of $\approx 0.5-1.5\ \mu$m. [S0031-9007(99)08797-9]

PACS numbers: 75.70.Cn, 61.12.Ha, 75.60.Ch, 75.70.Pa

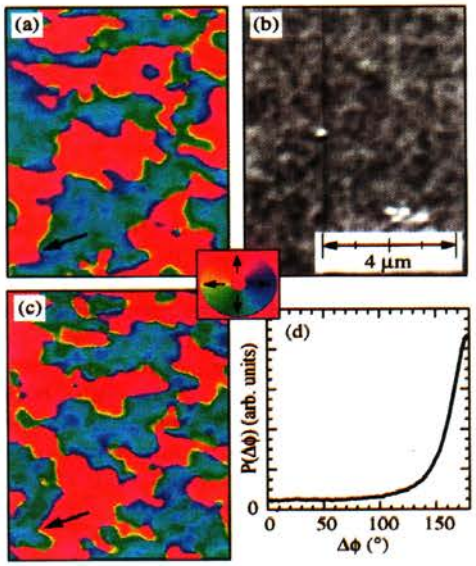

FIG. 3(color). SEMPA images of the topmost Co layer magnetization (a) and topography (b) and second Co layer magnetization (c) in the $[\text{Co}(6\text{ nm})|\text{Cu}(6\text{ nm})]_{20}$ sample. The magnetization direction is mapped into color as indicated by the color wheel in the center. A histogram of the difference in the magnetization direction between the two layers, $\Delta\phi$, is shown in (d).

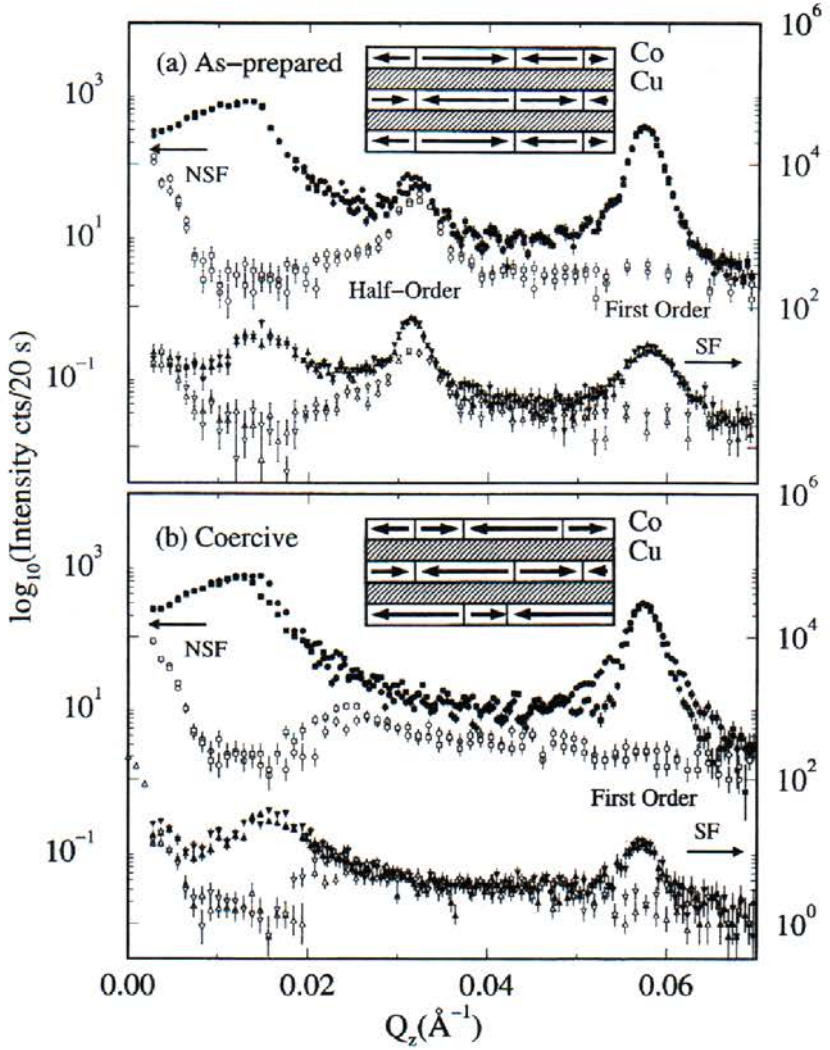

FIG. 2. Total PNR (shaded symbols) relative to the diffuse scattering (open symbols) as a function of $Q_z = 4\pi/\lambda \sin\theta$ for $[\text{Co}(6\text{ nm})|\text{Cu}(6\text{ nm})]_{20}$ in the (a) as-prepared and (b) coercive state at $H_C = 54$ Oe. The diffuse scattering was measured by offsetting the angle Ω by 0.2° and then scanning Q_z. The circles and squares correspond to $(--)$ and $(++)$ NSF data, respectively. The up and down triangles mark the $(+-)$ and $(-+)$ SF data. No corrections have been made for the polarization efficiencies or sample footprint. The insets show the idealized magnetic structures suggested by the scattering in each state.

Pinpointing Chiral Structures with Front/Back Polarized Neutron Reflectometry

K. V. O'Donovan, J. A. Borchers, and C. F. Majkrzak
NIST Center for Neutron Research
National Institute of Standards and Technology
Gaithersburg, MD 20899-8562

O. Hellwig, E. E. Fullerton
IBM Almaden Research Facility
San Jose, CA 95120-6001

We have developed a new method of using polarized neutron reflectometry (PNR) to extract the structure of buried magnetic spirals in magnetic films. This technique improves upon earlier methods by being particularly sensitive to the presence of magnetic twists vis-à-vis structures in which the magnetization direction does not vary appreciably. Tracking the formation and growth of twists may solve a number of puzzles that hamper the development of magnetic thin film devices.

In collaboration with IBM scientists, we have applied the technique to a thin-film exchange-spring magnet and confirmed that the results may violate the current theory regarding the behavior of such magnets. It has been predicted that exchange-spring magnets, comprised of soft and hard ferromagnets in close proximity, are a composite that has a strong moment and does not readily demagnetize [1]. Therefore, exchange-spring magnets should give industry the ability to make much smaller permanent magnets for use in the magnetic recording devices, and elsewhere. As a side effect, when a small external magnetic field is opposed to that of the magnet, the portion of the soft ferromagnet farthest from the hard ferromagnet may twist into alignment with the field. When the field is removed, the soft ferromagnet untwists. The film provided by IBM consists of the hard ferromagnet $Fe_{55}Pt_{45}$ topped by the soft ferromagnet $Ni_{80}Fe_{20}$ [2].

Figure 1 shows a simplified diagram of the behavior predicted by current theories [1]. A magnetic field of 0.890 T, provided by an electromagnet, is sufficient to align both the soft and the hard layers of our exchange-spring magnet, as shown on the left. When a modest reverse field (on the order of 0.025 T) is applied to the exchange spring magnet, only the top of the soft layer will realign with the magnetic field. The hard layer remains pinned in the original direction, and a continuous twist is induced in the soft layer, as the direction of magnetization changes smoothly between the reverse field direction to the aligning field direction.

Although there are many alternatives to PNR to measure the magnetization, typically they measure only the average orientation of the magnetic spins, and cannot readily distinguish a spiral from a structure in which all the spins are canted with respect to an external field. PNR can extract the depth-dependence of the magnetic and chemical structure. We have studied the sample over a wide range of external magnetic fields, and can track the development of the spiral with field [3].

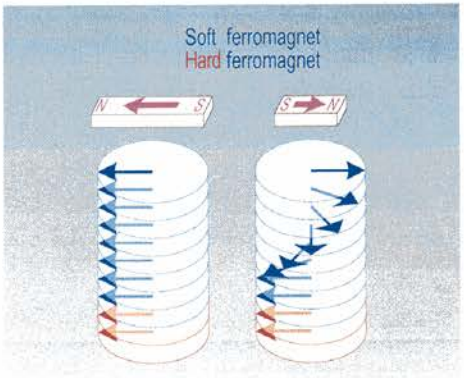

FIGURE 1. Model for field behavior of exchange-spring magnets. On the left the magnet has been aligned by a large external magnetic field. On the right a smaller field opposed to the first field causes a twist to form in the soft ferromagnet, while the hard ferromagnet remains aligned.

A PNR experiment begins with neutrons whose magnetic moments are aligned parallel (+) or opposite (−) to the external magnetic field. When the magnetization of the sample is perpendicular to this magnetic field, the neutron moment precesses as it interacts with the sample. When this happens the spin-flip (SF) reflectivities R^{+-} and R^{-+} are strong. If the magnetization of the sample is parallel to the external magnetic field, no precession occurs, but the non-spin-flip (NSF) reflectivities R^{++} and R^{--} will differ. The NSF reflectivities also provide information about the chemical structure of the film.

Our new modification of the PNR method greatly enhances the contrast between colinear and certain non-colinear magnetic structures [4]. We first measure the reflectivity with neutrons glancing off the front surface of the material, and then repeat with neutrons glancing off the back surface. The experiment is akin to holding the plane of the film up to a "magnetic mirror" to see whether the mirror image is the same as the original structure. In a colinear structure, all the spins are aligned along a common direction, and the mirror image is very much like the original structure.

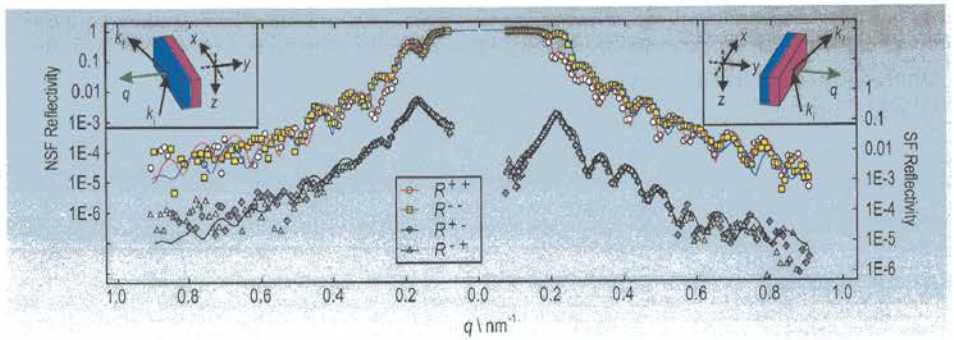

FIGURE 2. Reflectivity of a $Ni_{80}Fe_{20}|Fe_{55}Pt_{45}$ bilayer. The front reflectivity is plotted on the right while the back reflectivity is plotted on the left. The SF reflectivities R^{+-} and R^{-+} are plotted against the right ordinate axis. The NSF reflectivities R^{++} and R^{--} are plotted against the left ordinate axis.

But the mirror image of a magnetic twist to the right is a magnetic twist to the left. Therefore, if the front and back reflectivities are significantly different, we can deduce the presence of a spiral. Fitting the data confirms the spiral's existence.

Figure 2 shows data collected at 0.026 T after aligning in -0.89 T. Fits to the data are shown as solid lines. The data from the front reflectivity are shown on the right, and the data from the back reflectivity are shown on the left. The spin-flip (SF) reflectivities R^{+-} and R^{-+} are plotted against the right-hand axis, which have been shifted relative to the NSF reflectivities R^{++} and R^{--} plotted against the left axis. At $q = 0.2$ nm^{-1}, there is a splitting in the front NSF reflectivity that is much more pronounced than that of the back reflectivity at the same q. This is a hallmark of the spiral structure.

Figure 3 shows the magnetic structure that gives the excellent fit to the data plotted in Fig. 2. The location of the hard/soft interface is marked in Fig. 3. Surprisingly, we discover the spiral invades the hard ferromagnet even at extremely low fields. Current theory predicts that when this occurs, the soft ferromagnet will not be able to untwist fully. Yet, other magnetic studies show that our exchange-spring magnet does untwist when this field is removed. Thus, our PNR measurements have identified a shortcoming of current theory.

With this new technique, NIST is now able to better characterize the magnetic properties of thin films, which can improve the capability and reliability of industrial devices for magnetic recording and sensing.

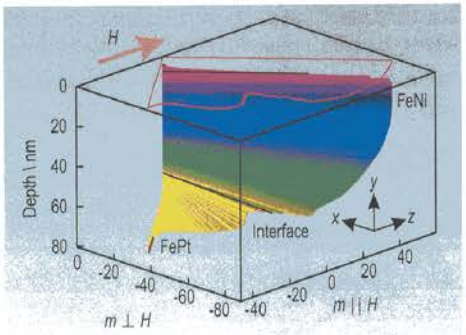

FIGURE 3. Fitted magnetization of the data presented in Fig. 2. The front of the sample is at a depth of 0 nm and the back is at a depth of 70 nm. The red curve is a projection of the magnetic structure into the plane of the front surface.

References

[1] E. F. Kneller and R. Hawig, IEEE Trans. Magn. **27**, 3588 (1991).
[2] O. Hellwig, J. B. Kortright, K. Takano, and E. E. Fullerton, Phys. Rev. **B62**, 11694 (2000).
[3] K. V. O'Donovan, *et al.*, in preparation.
[4] K. V. O'Donovan, *et al.*, submitted to Applied Physics A.

Exchange-spring magnets

Miniature sensors and devices (*e.g.*, magnetic recording) require small volume of high moment and anisotropy. Solution of Kneller and Hawig: produce a composite which combines small grains of both types of real ferromagnets.

Do they work "as advertised?"

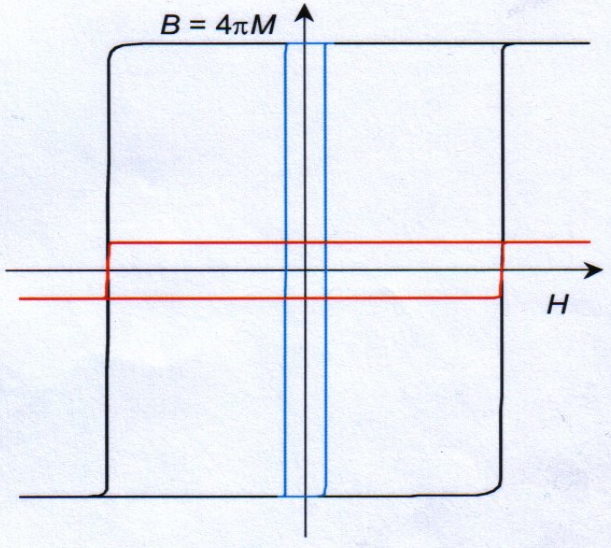

Ideal ferromagnet – large magnetization, large anisotropy

Typical soft ferromagnet – large magnetization, small anisotropy

Typical hard ferromagnet – small magnetization, large anisotropy

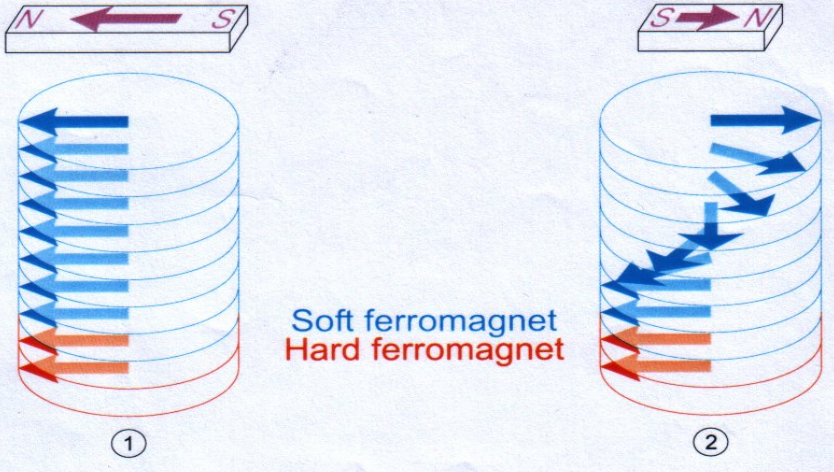

Front/Back Asymmetry of Magnetic Structures

Collinear structure:
front and back look the same

Noncollinear structure:
front and back look different

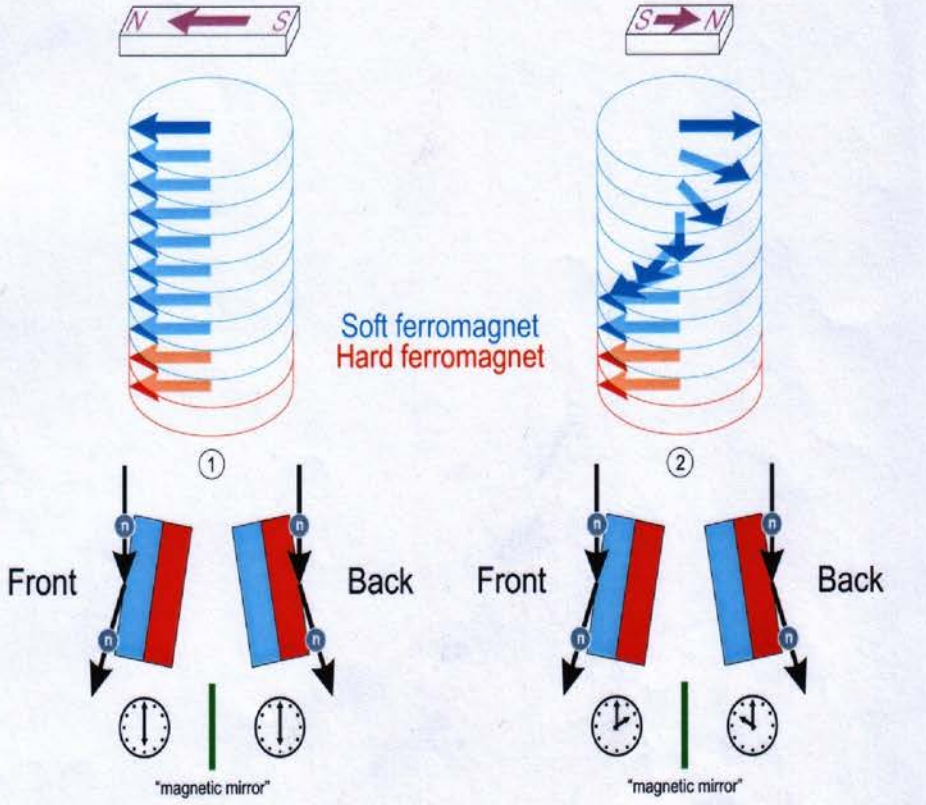

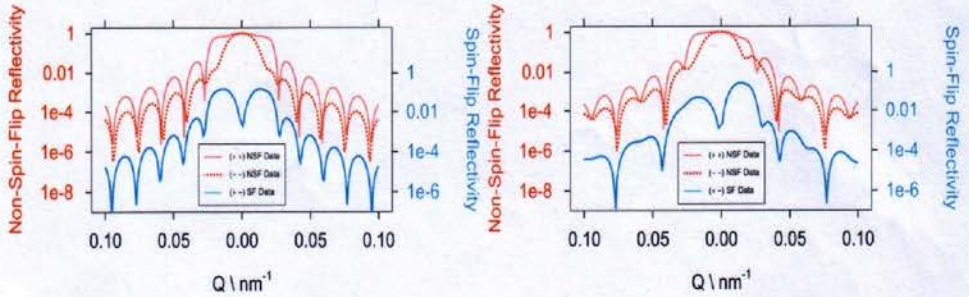

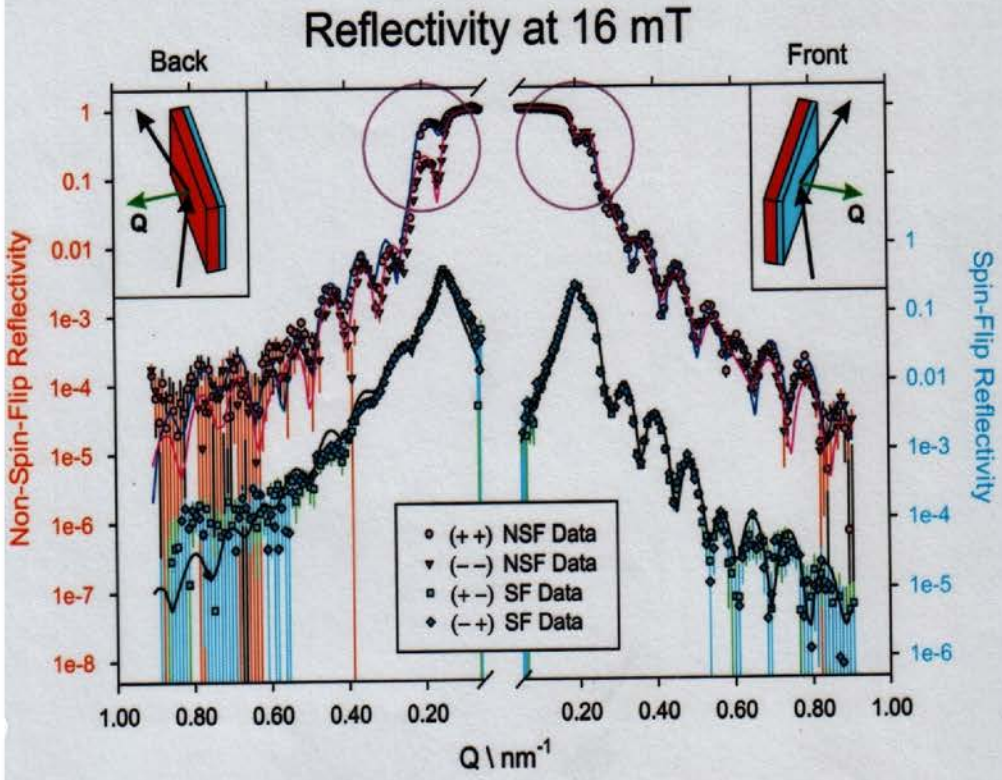

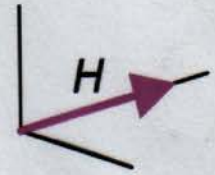

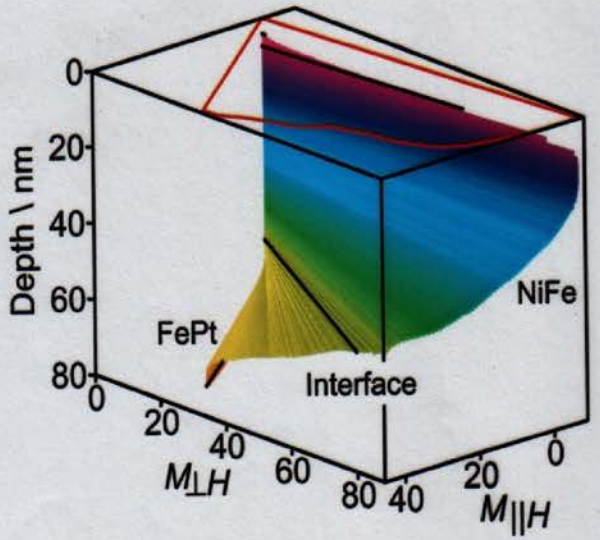

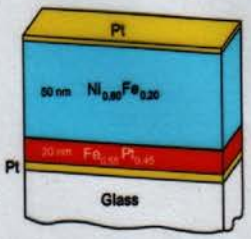

Deposited using magnetron sputtering
FePt codeposited from elemental targets
NiFe deposited from alloy target

Realization of ground-state artificial skyrmion lattices at room temperature

D. A. Gilbert,[1,2] B. B. Maranville,[2] A. L. Balk,[3,4] B. J. Kirby,[2] P. Fischer,[5,6]
D. T. Pierce,[3] J. Unguris,[3] J. A. Borchers,[2] and K. Liu[1]

Moore's Law has been the icon of the computer revolution for nearly 50 years, but recent challenges with heat management and miniaturization have signaled its impending end. Spintronics – data and logic technologies that use the electron spin, in addition to the electron charge – offer a new approach to ultra-low power information technologies that may reinvigorate Moore's Law. One promising spintronic technology is the magnetic skyrmion. Skyrmions are specialized configurations of magnetic moments into topologically-protected structures; a typical skyrmion structure, shown in Fig. 1, possesses a core and perimeter with opposite out-of-plane spin orientations, and a closed, continuous in-plane winding of magnetic moments between. These structures can be realized on the atomic scale, moved with very low electrical current densities, and are robust against moderate perturbations including stray fields and system defects. These make skyrmions very attractive for ultra-low power, high-density data storage and logic technologies. A key challenge to the development of skyrmion-based memory and logic devices is achieving skyrmion structures stable at ambient conditions (room temperature and no magnetic field).

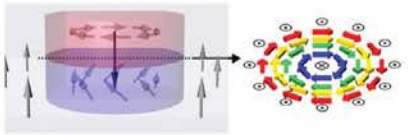

FIGURE 1: Diagram of an artificial skyrmion. Vortex dot is shown in red. The imprinted region (blue) that forms a skyrmion with the underlayer is shown in grey.

Recently, we have realized ground-state magnetic skyrmions stable at ambient conditions by nanopatterning [1]. Specifically, cobalt nanodots with diameters of 560 nm and heights of 30 nm are patterned. The magnetic 'vortex' configuration within these dots, shown in Fig. 1 (red), form a closed winding structure, with an out-of-plane core, which is stable over a wide range of temperatures. However, a vortex lacks an out-of-plane perimeter, distinguishing it from a skyrmion. By placing a vortex-state nanodot on top of a magnetic film, the loop structure and core can be imprinted into the film. Thus, by designing a film with an out-of-plane orientation, the imprinted structure at the interface has a closed loop structure with an out-of-plane core and perimeter, e.g. a skyrmion. To prove this claim and demonstrate its viability for application, three pieces of evidence must be shown: (1) the direction of circulation of the loop structure, called the circularity, must be controllable, (2) the orientation of the core, called the polarity, relative to the perimeter must be controllable, and (3) the loop structure must, in-fact, be imprinted into the film underlayer.

Samples were prepared by a three-step process. In step one, multilayer films of $[Co(0.5\ nm)/Pd(1\ nm)]_{10}$ were grown on naturally oxidized Si substrates; the multilayer structure gives the film a preferred out-of-plane orientation - called the perpendicular magnetic anisotropy (PMA). In the second step, hexagonal arrays of nano-holes with a diameter of 560 nm and center-to-center spacing of 1000 nm were patterned into a ≈ 400 nm thick polymer layer that was spin-coated onto the Co/Pd film. The holes are shaped like a circle, with one side made flat; the asymmetric structure has been previously used to realize circularity control. Next, the sample was irradiated by 1 keV Ar^+ plasma, which suppresses the PMA in the regions exposed by the holes, while the regions still protected by polymer retain their PMA. During the third step, 32 nm of Co was deposited into the holes and the polymer mask removed, realizing asymmetric Co dots grown over the irradiated regions. Once the sample was fabricated, the skyrmion state was configured by a designed field sequence. First, the Co/Pd underlayer was saturated in the positive out-of-plane direction using a large out-of-plane magnetic field. Then, the out-of-plane field was removed and a small in-plane magnetic field was applied to saturate the dots parallel to the flat edge. At this point a small out-of-plane magnetic field was applied anti-parallel to the underlayer. The in-plane magnetic field was removed, nucleating a vortex, with the core biased to be anti-parallel to the underlayer. Lastly, the out-of-plane magnetic field was removed, leaving the system at remanence (no magnetic field) in a vortex state dot, with a core anti-parallel to the underlayer, and the region under the dot having no PMA.

[1] University of California, Davis, CA 95616
[2] NIST Center for Neutron Research, National Institute of Standards and Technology, Gaithersburg, MD 20899
[3] Center for Nanoscale Science and Technology, National Institute of Standards and Technology, Gaithersburg, MD 20899
[4] University of Maryland, College Park, MD 20742
[5] Lawrence Berkeley National Laboratory, Berkeley, CA 94720
[6] University of California, Santa Cruz, CA 94056

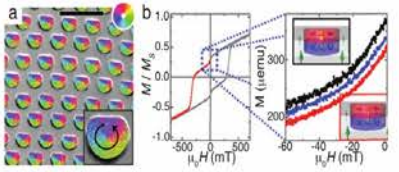

FIGURE 2: (a) SEMPA image of the asymmetric dot array. Color wheel indicates magnetization direction. (b) Remnant magnetization curve, with the core parallel, anti-parallel, and random relative to the underlayer, shown in black, red and blue, respectively (1 emu = 10^{-3} A m^2).

As stated above, circularity control was achieved by using the asymmetric dot structure. Applying an in-plane magnetic field parallel to the flat edge of the dot defines the nucleation site for the vortex and thus the circularity. Micrographs taken using scanning electron microscopy with polarization analysis (SEMPA) are shown in Fig. 2(a). The colors indicate the direction of the magnetization; the common color wheel for each of the dots indicates a common circularity of the magnetization. Other magnetic imaging technique and magnetometry measurements confirm the circularity control seen in SEMPA.

Recalling the magnetic field sequence to set the skyrmion state, polarity control is determined during the vortex nucleation by the small magnetic field applied anti-parallel to the underlayer. To demonstrate polarity control, the remanent magnetization was measured with the core parallel and anti-parallel to the underlayer. Specifically, the sample was prepared as discussed above, with the core anti-parallel to the underlayer and the out-of-plane magnetization measured as the magnetic field was decreased from remanence to negative saturation. In this case the magnetization of the core and perimeter are opposite, and thus subtract when measured together. Then, the sample was prepared again, but with the biasing field applied parallel to the underlayer. In contrast to the former case, the magnetization from the core and underlayer are expected to be parallel and add together. In a third measurement no biasing field was applied and the polarity was random. Indeed, as shown in Fig. 2(b), the skyrmion state, with the core and underlayer anti-parallel, has the smallest magnetization; the vortex state with the core and the underlayer oriented parallel has the largest magnetization; the random polarity falls in-between the parallel and anti-parallel configurations. This confirms the biasing field indeed defines the polarity.

Lastly, and arguably most crucially, the imprinting of the skyrmion was demonstrated using polarized neutron reflectometry (PNR), performed on the MAGIK reflectometer. PNR is a technique that uses scattering to extract depth-profiles from layered systems and possesses sensitivity to nuclear and magnetic features. The measured data are shown as dots in Fig. 3(a). A model was made to simulate the nominal structure and the reflectivity pattern calculated. By iteratively changing the model and comparing the calculated reflectivity to the data, the model converges on an accurate representation of the physical system. The

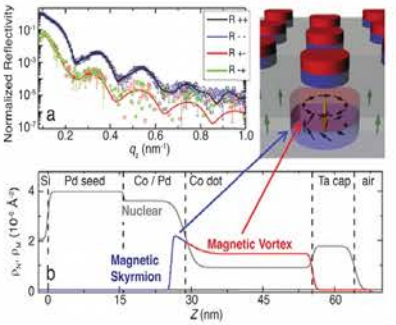

FIGURE 3: (a) Measured (dots) and simulated (lines) reflectometry, and (b) converged depth profile.

converged model is shown in Fig. 3(b), and the corresponding reflectometry is shown as the solid lines in Fig. 3(a), which agree well with the experimental data ($\chi^2 < 1.2$). The converged model correctly identifies the designed structure, giving confidence in its accuracy. More importantly, the model identifies the magnetization of the Co dot - as expected - but also shows that the magnetization extends ≈ 3 nm below the [Co/Pd]/Co-dot interface. This imprinted magnetic feature is the first direct evidence of the imprinted magnetic skyrmion. Further, the imprinted skyrmion is expected to be stable while the dots and underlayer are stable (ambient conditions up-to approximately 300 °C, and 300 mT). Theoretical modeling using NIST's object oriented micromagnetic framework (OOMMF) confirms that the imprinted structure extends 2 nm into the underlayer.

In summary, we have successfully achieved room temperature artificial skyrmion lattices in the ground state over extended areas, defining a platform for exploring skyrmion properties and behaviors as well as the use of skyrmion lattices in novel technological concepts. The system is constructed by fabricating circularity controlled Co nanodots on a selectively irradiated Co/Pd underlayer with PMA. Circularity control is imposed by the fabrication of asymmetric dots and confirmed by microscopy. Polarity control is realized by the application of a small out-of-plane magnetic field during the vortex nucleation, and demonstrated in the magnetization curves. The imprinted skyrmion lattice in the Co/Pd is directly confirmed by PNR, and is quantitatively consistent with micromagnetic simulations. These artificially constructed skyrmion lattices are stable over a wide range of magnetic fields and temperatures, including room temperature and zero magnetic field. These foundational results present a new path in skyrmion research on the meso-scale, at and above room temperature.

Reference

[1] D. A. Gilbert, B. B. Maranville, A. L. Balk, B. J. Kirby, P. Fischer, D. T. Pierce, J. Unguris, J. A. Borchers, K. Liu, Nature Communications **6**, 8462 (2015).

CONDENSED MATTER

Beyond the interface limit: structural and magnetic depth profiles of voltage-controlled magneto-ionic heterostructures

D. A. Gilbert,[1] A. J. Grutter,[1] E. Arenholz,[2] K. Liu,[3] B. J. Kirby,[1] J. A. Borchers,[1] and B. B. Maranville[1]

Oxidation is a common process that changes virtually every quality of a material, including optical, mechanical, electrical, thermal, and magnetic properties. For example, metals are typically shiny, ductile, conductive, and can be magnetic, while metal oxides can be matte or transparent, brittle, insulating, and are frequently non-magnetic. Controlling oxidation by electric fields offers an opportunity for manipulating the material properties with the flip of a switch. This is the premise behind both memristors, which use a voltage to control oxygen distributions and tune electrical conductivity, and magneto-ionic devices [1-5], which similarly use a voltage to tune magnetic properties. These technologies work by recognizing that metal oxides are ionic solids with oxygen atoms that have a net charge and thus are sensitive to electric fields. Applying a strong electric field can thus alter the oxygen ion distribution, changing the material properties. Recent investigations [1, 2] have demonstrated magneto-ionic control in ultra-thin Hall bar structures (thicknesses < 1 nm). In these studies, the films prefer to have the magnetization oriented out of the plane of the film; using an electric field to drive oxygen into the interface with a neighboring oxide material causes the magnetization to rotate into the plane of the film. Devices built on this control have been proposed for ultra-high density, low-power data storage technologies. However, for broader applications, ion-based control must be demonstrated in thicker films with bulk-like properties, and it is unclear how the magneto-ionic control mechanism works in this regime.

In this work, we demonstrated magneto-ionic effects in comparably thick (15 nm) cobalt films [5]. Using an applied voltage, oxygen was driven from a GdO_x/AlO_x film into the neighboring Co film, which then becomes non-ferromagnetic CoO_x. Magnetometry revealed that, while some of the magnetic properties are recovered, others are not. Using polarized neutron reflectometry (PNR), the depth-resolved oxygen distribution and magnetization were directly mapped, providing a physical picture to explain the observed behavior.

Thin-films with a structure Si/Pd(50 nm)/AlO_x(1000 nm)/GdO_x(2 nm)/Co(15 nm)/Pd(20 nm) were grown by sputtering and e-beam evaporation at the Center for Nanoscale Science and Technology. Electro-thermal (E+T) conditioning was performed by heating the sample to 230 °C and applying 40 V across the Pd layers for 15 min. The measured PNR reflection and

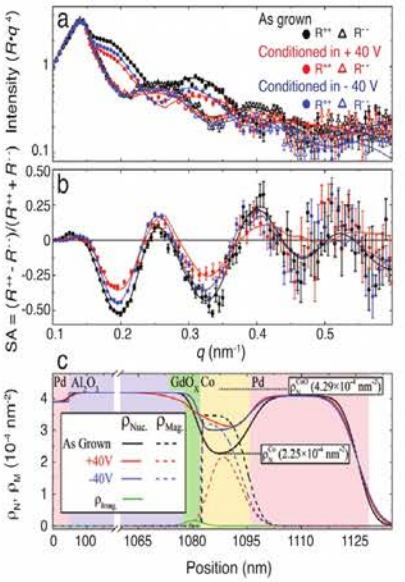

FIGURE 1: (a) Fitted PNR data scaled by q^4 and (b) spin asymmetry for the sample as-grown and after electro-thermal conditioning. (c) Depth-dependent real and imaginary nuclear SLD (ρ_N and ρ_{imag}), and magnetic SLD (ρ_M) extracted from the PNR. In (a) and (b) the experimental data are shown as symbols, and the lines are fits corresponding to the depth profile shown in (c).

spin-asymmetry (SA) for the as-grown sample, the sample after applying + 40 V (anode on the top surface), and sequential - 40 V are shown in Figs. 1(a) and (b), respectively. The SA, which is proportional to the product of the magnetization and nuclear scattering length density (SLD), is shown to decrease after the + 40 V treatment and partly recover after subsequently applying - 40 V. Using the Refl1d software package, models for the three treatments (as-grown, after + 40 V, and after sequential +/- 40 V) were fitted in parallel, Fig. 1(c). The fitted model for the as-grown sample closely matches the designed structure and the bulk nuclear SLD for these materials, lending confidence to its accuracy. After the initial + 40 V treatment the nuclear SLD increases in the Co layer, the GdO_x/Co interface becomes much broader, and the

[1] NIST Center for Neutron Research, National Institute of Standards and Technology, Gaithersburg, MD 20899
[2] Advanced Light Source, Lawrence Berkeley National Laboratory, Berkeley, CA 94720
[3] University of California, Davis, CA 95616

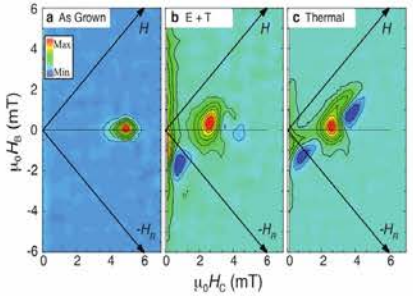

FIGURE 2: FORC distributions for the sample (a) as-grown, (b) after +/- 40 V conditioning, and (c) after thermal-only conditioning.

magnetic SLD decreases (38 %), most prominently at the interface (80 %). This is consistent with oxygen being moved by the electric field from the GdO_x layer into the Co layer, forming non-magnetic CoO_x. Subsequently applying - 40 V restored the sharp nuclear interface and most of the magnetism (92 %). However, oxygen migration was irreversible for thicknesses greater than 10 nm. Measurements performed using a thermal-only treatment showed a much smaller effect, demonstrating that the electric field moves oxygen into and out of the Co layer depending on its polarity.

Magnetic first order reversal curve (FORC) measurements of the as-grown sample, the +/- 40 V sample, and a thermally treated sample (230 °C for 30 minutes) are shown in Fig. 2. The FORC plots, in a general sense, are a map of all hysteretic events that exist within a system and provide detailed information regarding the magnetic reversal process. The FORC distribution for the as-grown sample shows only a single feature, indicating a single magnetic phase. By comparison the electro-thermal and thermal-only samples show two features, with a new feature located at $H_C = 0$ that specifically identifies reversible features. In general, reversible features indicate the absence of hysteresis and are often manifest when the magnetism is measured along a hard axis. We suggest that the new reversible phase is the result of a decoupling between grains within the Co film plane. Specifically, the film is comprised of many nano-scale magnetic grains, each with their own randomly oriented magnetocrystalline anisotropy. Typically, magnetic exchange coupling between neighboring grains can cause the film to behave as a single coherent structure. The small amount of residual oxygen may be interrupting the exchange interaction, allowing the magnetocrystalline anisotropy of each grain to dictate its orientation.

We suggest the reduced exchange interaction and irreversibility for thicknesses of > 10 nm is due to a screening effect of the electric field, as shown in Fig. 3. Specifically, the + 40 V electro-thermal treatment moved oxygen deep into the film, diffusing quickly at grain surfaces and more slowly in the bulk. During the - 40 V treatment the oxygen migrated quickly off of the grain surface,

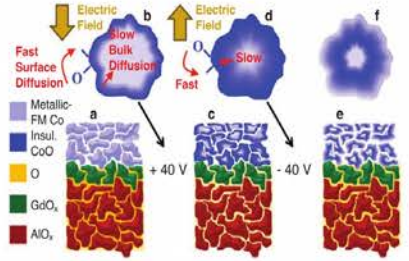

FIGURE 3: Cross-section view of (a) the as grown film, (b) a single grain during + 40 V treatment, (c) the film after + 40 V treatment, (d) a single grain during subsequent - 40 V treatment, and (e, f) cross section and grain after - 40 V treatment. Colors identify AlO_x (red), GdO_x (green), metallic FM Co (light blue), insulating non-FM CoO_x (blue), and interstitial oxygen (orange); large gold arrow indicates the electric field. Illustration (e) emphasizes fast surface migration, identified by the red arrows, and slow bulk diffusion, indicated by the grey arrows.

leaving a metallic Co shell. This shell screens the electric field via the Faraday effect, thus halting any further migration and trapping oxygen within each grain and deeper in the film. This mechanism suggests an unexplored role of the microstructure, and a potential limit to these technologies.

In summary, we have realized a thin film magneto-ionic device built on a thick (15 nm) Co film. Semi-reversible control of the magnetism resulting from oxygen migration was demonstrated and directly mapped using polarized neutron reflectometry. First order reversal curve measurements showed that the nominally similar sample possessed two phases, while the as-grown sample had only one. Based on a fundamental understanding of the nature of electric fields and oxygen migration, a physical picture was presented which supports the results. This work thus demonstrates that ionic devices with 'active' layers thicker than a few atom layers are still viable, thus opening new opportunities for future ion-based technologies.

References

[1] U. Bauer, L. Yao, A. J. Tan, P. Agrawal, S. Emori, H. L. Tuller, S. v. Dijken, G. S. D. Beach, Nature Mater. **14**, 174 (2015).

[2] C. Bi, Y. Liu, T. Newhouse-Illige, M. Xu, M. Rosales, J. W. Freeland, O. Mryasov, S. Zhang, S. G. E. t. Velthuis, W. G. Wang, Phys. Rev. Lett. **113**, 267202 (2014).

[3] D. A. Gilbert, J. Olamit, R. K. Dumas, B. J. Kirby, A. J. Grutter, B. B. Maranville, E. Arenholz, J. A. Borchers, K. Liu, Nature Commun. **7**, 11050 (2016).

[4] A. J. Grutter, D. A. Gilbert, U. S. Allan, E. Arenholz, B. B. Maranville, J. A. Borchers, Y. Suzuki, K. Liu, B. J. Kirby, Appl. Phys. Lett. **108**, 082405 (2016).

[5] D. A. Gilbert, A. J. Grutter, E. Arenholz, K. Liu, B. J. Kirby, J. A. Borchers, B. B. Maranville, Nature Commun. **7**, 12264 (2016).

CONDENSED MATTER

Mostly *Soft* Matter


David Worester*
E112 x5798


Daniel Scott
E116 x6128


David Hoogerheide*
E126 x8839


Ella Mihailescu*†
E130 x8327


Mathias Loesche*†
E104 x8128


Hirsh Nanda*
E103 x8367


Vitalii Silin*†
E105 x5234


Frank Heinrich*
E103 x4507


Joseph Curtis
E121 x3959


Sushil Satija
E104 x5250


Guangcui Yuan*
A120 x5098

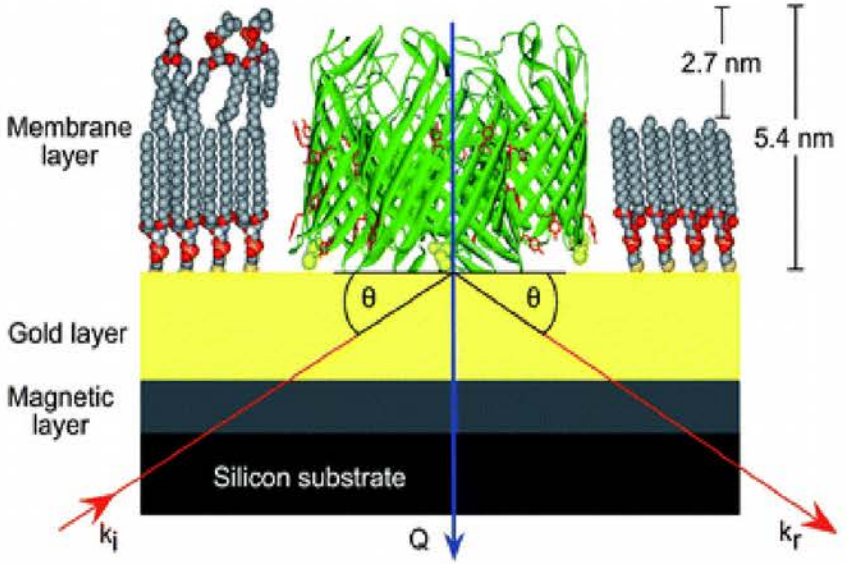

(after Holt et al.)


Susan Krueger
E121 x6734

Polymer Science

Early on, colleagues from various institutions, including Tom Russell, Frank Bates, Anne Mayes, Spiros Anastasiadis, Mark Foster, and at NIST, Sushil Satija, Alamgir Karim, Wen Li Wu, and others made pioneering studies of polymer thin film systems using neutron reflectometry as a probe. Greg Smith and Bill Hamilton were also involved in some of this research. Polymer science has continued to be a mainstay of NR activities at the NCNR with regular contributors such as Bulent Akgun.

Structure of symmetric polyolefin block copolymer thin films

Mark D. Foster,[a)] Mohan Sikka, Navjot Singh, and Frank S. Bates
Department of Chemical Engineering and Materials Science, University of Minnesota, Minneapolis, Minnesota 55455

Sushil K. Satija and Charles F. Majkrzak
National Institute of Standards and Technology, Reactor Radiation Division, Gaithersburg, Maryland 20899

(Received 5 February 1992; accepted 27 February 1992)

The microstructure of thin films of nearly symmetric poly(ethylene–propylene)–poly(ethylethylene) (PEP-PEE) diblock copolymers ($f = 0.55$, where f is the volume fraction of PEP) was characterized by neutron reflectometry (NR). A symmetric film structure in which the PEE block segregates preferentially to both interfaces is observed above and below the bulk order–disorder transition (ODT). Measurements at room temperature for several chain lengths, N, provide a real-space picture of the change in interdomain interfacial profiles associated with the crossover between the strong and weak segregation limits. The polymer/air and substrate/polymer interfaces are observed to induce an ordered microstructure even when the center of the film is disordered. The characteristic dimension of this near surface microstructure is larger than the corresponding bulk value for values of χN lying between those of the bulk Gaussian-to-stretched-coil and order–disorder transitions, where χ is the segment–segment interaction parameter. This behavior is attributed to the correlation of large amplitude composition fluctuations in the film with the interfaces. A mean-field behavior prevails for $\chi N < (\chi N)_{\mathrm{GST,bulk}}$, where some preferential segregation occurs at the interfaces, but the characteristic dimension once again matches that in the bulk.

Tom Russell, Frank Bates, and Mark Foster, CW from top left.

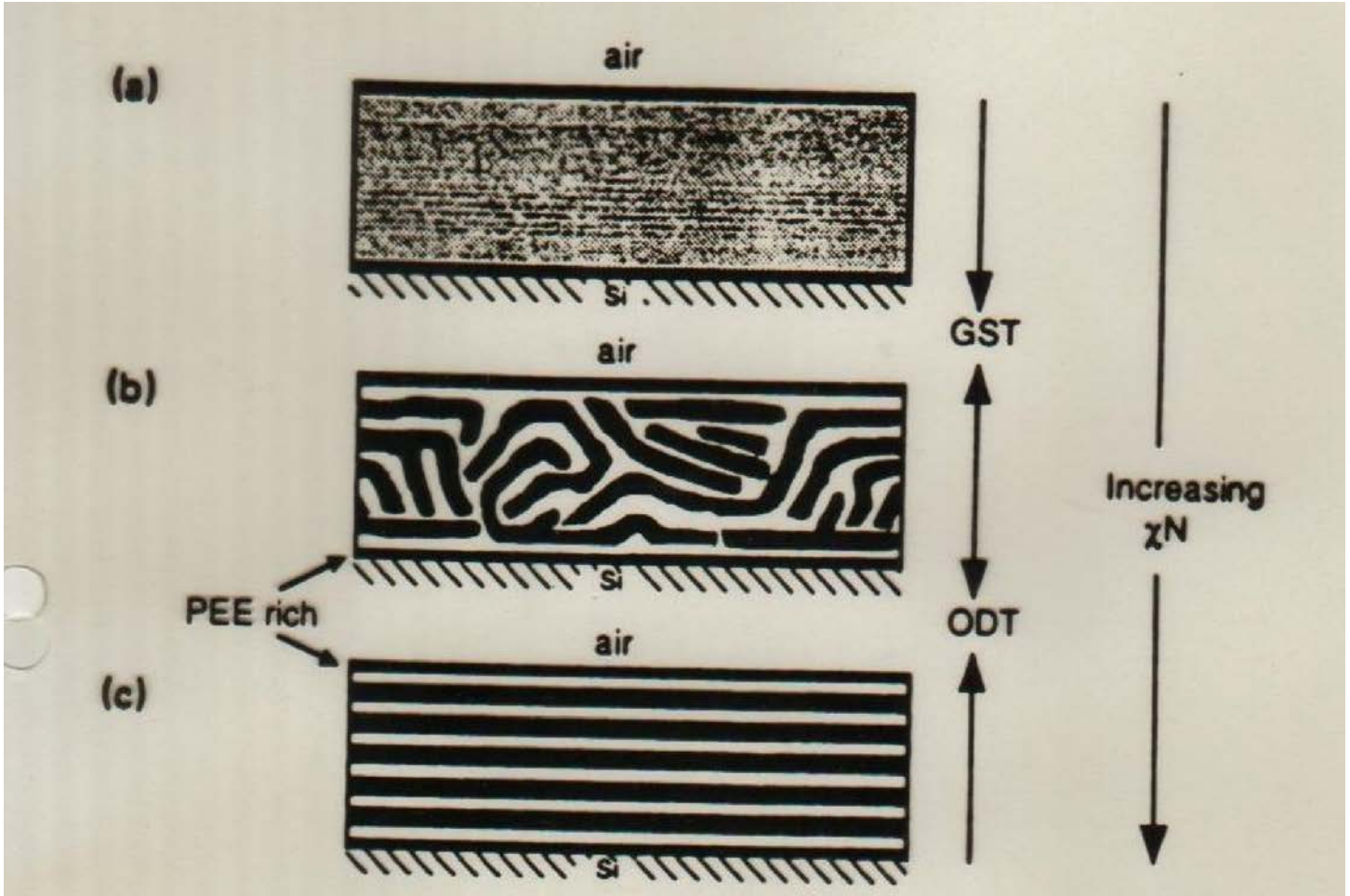

FIG. 5. Thin film morphologies for symmetric PEP–PEE diblock copolymers. (a) Interfacial segregation of PEE occurs for $\chi N < (\chi N)_{GST}$. The center of the film is spatially homogeneous. (b) For $(\chi N)_{GST} < (\chi N) < (\chi N)_{ODT}$ the film contains a microstructured morphology that is oriented at the film interfaces. The range of the orientational correlation increases with increasing (χN). (c) A lamellar microstructure that is highly oriented with the film interfaces exists when $(\chi N) > (\chi N)_{ODT}$.

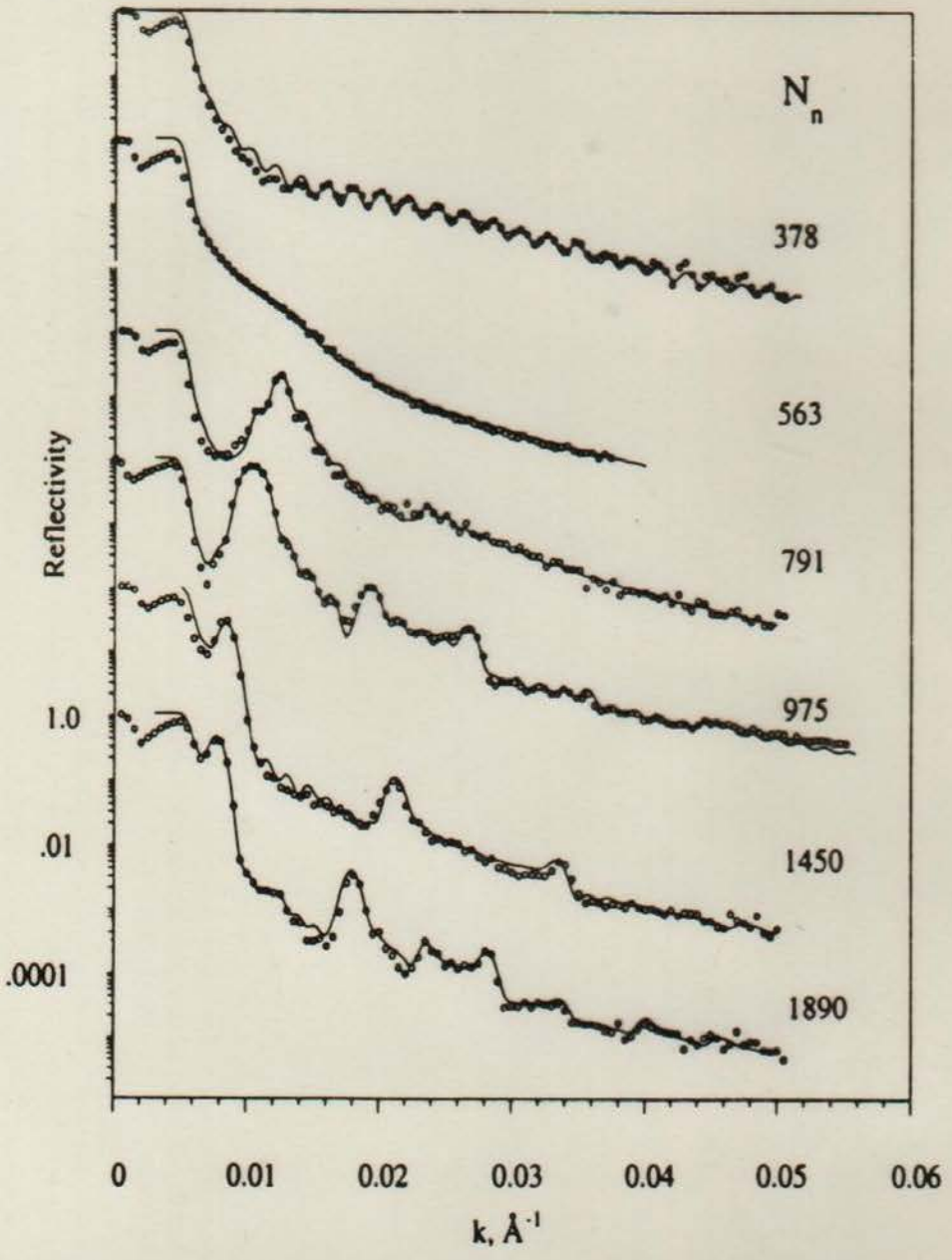

FIG. 8. Reflectivity data for six PEP–PEE chain lengths and the corresponding model curves used to infer concentration profiles illustrated in Fig. 9. The results for $N < 1890$ have been shifted vertically. Poor agreement between the model curves and data in the vicinity of the critical wave vector stems from an experimental artifact that also produces the apparent lack of total reflectivity for $k \lesssim k_c$ (Ref. 32).

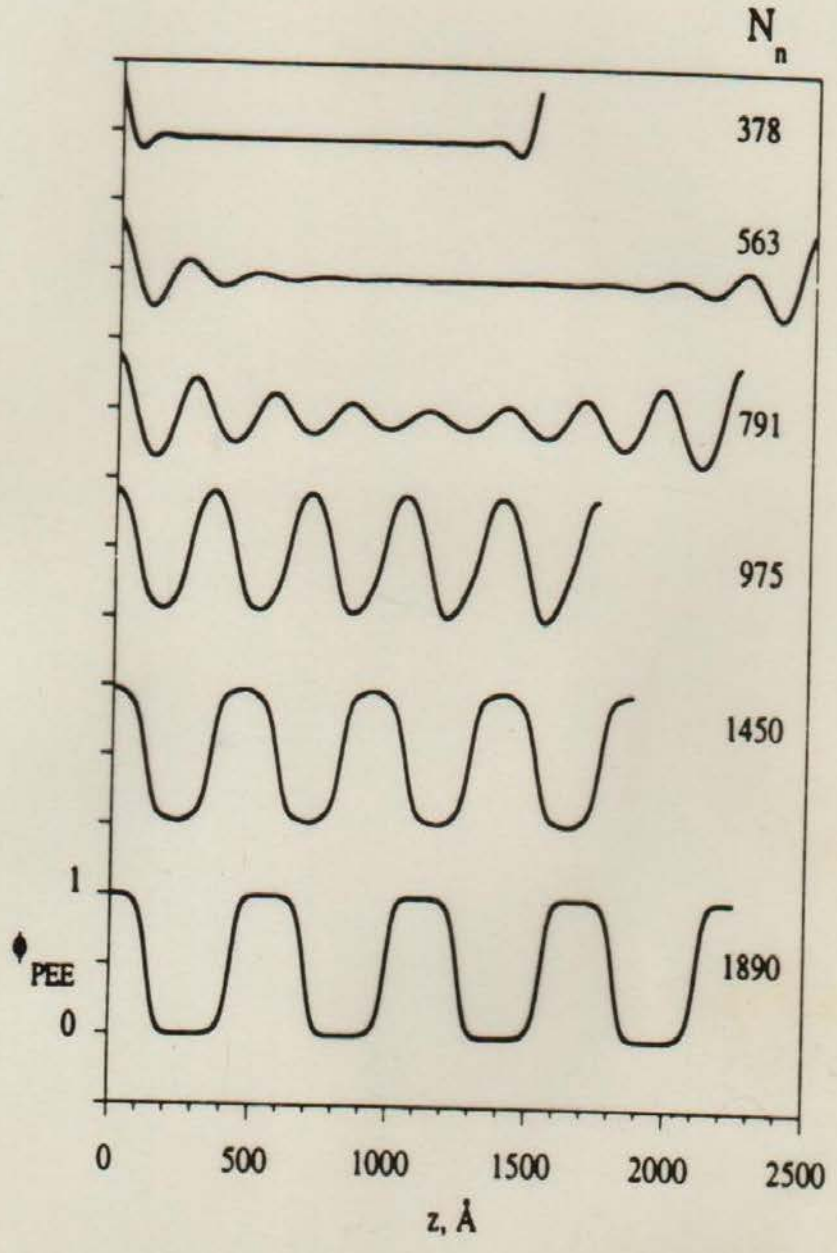

FIG. 9. Real space concentration profiles corresponding to the model curves shown in Fig. 8.

nSoft

Connecting polymer-solvent interactions to structural transformations during solvent vapor annealing of block polymer thin films

C. K. Shelton,[1] R. L. Jones,[2] J. A. Dura,[3] and T. H. Epps, III[1,4]

Solvent vapor annealing (SVA) is a powerful technique for directing nanostructure ordering, orientation, and morphology in block polymer (BP) thin films for applications in emerging nanotechnologies such as nanolithographic masks, nanoporous membranes, nanotemplating, and organic optoelectronics. Swelling BP thin films with solvent vapor plasticizes polymer chains and reduces polymer glass transition temperatures (T_gs), thereby increasing chain mobility and allowing nanostructures to reorganize into well-ordered morphologies. With judicious control over factors including the solvent vapor composition, solvent vapor partial pressure, and swelling/deswelling pathways to influence the thermodynamics and kinetics of the polymer-solvent interactions, one can access a myriad of potential nanostructure conformations not obtainable by traditional thermal annealing alone. Additionally, SVA is ideal for BP systems that are susceptible to thermal transitions and degradation or require infeasible thermal annealing time scales. Therefore, we recently employed a combination of *in situ* small-angle neutron scattering (SANS) and neutron reflectivity (NR) to elucidate the importance of polymer-solvent interactions on morphology development during SVA of BP thin films [1]. Our results allowed us to glean key insights into the mechanisms of SVA and develop a more predictive approach to target desired nanostructure self-assembly.

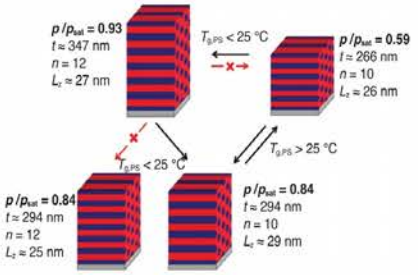

FIGURE 1: Schematic detailing the process by which SIS nanostructures restructured during SVA. SVA promoted layering of parallel PS cylinders by swelling the film to impart chain mobility *via* reduction of the T_g of the glassy PS domains below the annealing temperature (25 °C). To account for the film thickness (t) reduction during solvent removal from p/p_{sat} = 0.93 to p/p_{sat} = 0.84, n decreased, rather than L_z, to prevent unfavorable compression of the SIS polymer chains. However, commensurability conditions from mismatches in t and n and an increased polymer-polymer interaction parameter (χ_{PS-PI}) led to slightly stretched layers (L_z = 27 to L_z = 29). When there was not enough solvent in the film to lower the PS T_g below 25 °C ($p/p_{sat} \leq 0.59$), n could no longer adjust to account for thickness changes; instead, the average L_z decreased with the value of p/p_{sat} to account for the change in t.

Although the effects of SVA on BP self-assembly have been well researched, studies probing how solvent segregation into individual domains governs reorganization kinetics and thermodynamics have not been prevalent. Therefore, we used *in situ* neutron scattering to quantify the segregation of deuterated benzene (*d*-benzene) into the polystyrene (PS) and polyisoprene (PI) domains of PS-cylinder-forming poly(styrene-*b*-isoprene-*b*-styrene) (SIS) BP thin films as a function of atmospheric solvent concentration (solvent partial pressure divided by solvent vapor pressure [p/p_{sat}]) [1]. Neutron scattering with solvent deuteration provided enhanced polymer-solvent contrast, in comparison to traditional X-ray experiments. From our neutron scattering analysis, we elucidated the full mechanism that describes how the number of stacked domains (n) and the out-of-plane domain spacing (L_z) changed as a function of film thickness and p/p_{sat} (Figure 1). The key factor in this mechanism was the amount of solvent in the PS block, a commonly ignored parameter that caused a transition between a glassy PS state (kinetically trapped layers) and a non-glassy PS state (mobile layers); the PI domain is always non-glassy at room temperature. Primarily, we found that higher solvent concentrations in the PS domain lowered the T_g below room temperature, which increased the chain mobility and allowed the domains to rearrange and form the low energy domain spacing (modified slightly by commensurability). As the solvent concentration was decreased, T_g increased above room temperature, n was fixed, and L_z decreased as the film de-swelled. Interestingly, although the minority PS domain (cylinders) was the only glassy component at low solvent concentration, the non-glassy PI matrix was kinetically trapped as well and forced to conform to the same compressed L_z. This competition between polymer-solvent thermodynamics and kinetics resulted in an unexpected increase in L_z (27 nm to 29 nm) upon deswelling the film from a p/p_{sat} value of 0.93 to a p/p_{sat} value of 0.84, as there was sufficient *d*-benzene in the PS domain (51 % by mole and 40 % by mole, respectively) to lower the T_g of PS below 25 °C and impart chain mobility [2]. Therefore, the polymer chains were able to decrease n from 12 to 10 and maintain a favorable L_z at a reduced film thickness [3]. At the new n = 10, the layers were stretched slightly from 27 nm to 29 nm to achieve commensurability between the film thickness and L_z and to account for the slight increase in χ_{PS-PI} when the solvent concentration in the film was reduced.

[1] Department of Chemical and Biomolecular Engineering, University of Delaware, Newark, DE 19716
[2] Materials Science and Engineering Division, National Institute of Standards and Technology, Gaithersburg, MD 20899
[3] NIST Center for Neutron Research, National Institute of Standards and Technology, Gaithersburg, MD 20899
[4] Department of Materials Science and Engineering, University of Delaware, Newark, DE 19716

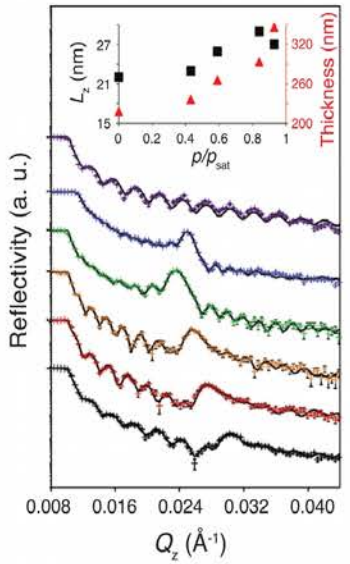

FIGURE 2: NR profiles (data point) and model fits (black lines) for *d*-benzene swollen SIS films at different p/p_{sat} in the order that they were run from top to bottom. Upon exposure to solvent vapor, the film increased in thickness (t) due to solvent swelling and developed repeating parallel cylinder layers as evidenced by the narrowing of Kiessig fringes and the formation of a Bragg peak, respectively. In general, L_z decreased with the value of p/p_{sat}. However, L_z increased slightly from p/p_{sat} = 0.93 to p/p_{sat} = 0.84. This effect was attributed to the reduction of n and subsequent incommensurability promoting slightly thicker layers. The inset plot shows how the film thickness and L_z change as a function of p/p_{sat}. The NR profiles have been vertically offset for clarity.

This unexpected transition from increasing to decreasing L_z during deswelling was determined from NR results obtained at the multi-angle grazing-incidence *k*-vector (MAGIK) reflectometer (Figure 2). The Bragg peak, which indicated the development of a periodic out-of-plane domain structure (parallel cylinders), shifted to a lower Q_z value going from the first (p/p_{sat} = 0.93) to second (p/p_{sat} = 0.84) solvent concentration and increased thereafter. This distinct shift signified an initial increase in L_z. Because the film thickness only decreased during deswelling, n had to decrease to maintain the low energy domain spacing. However L_z increased above this value to maintain commensurability with the film thickness, t. Following the initial increase in L_z the number of domains was fixed by the immobility of the PS domain, and L_z was forced to decrease with film thickness as solvent was removed.

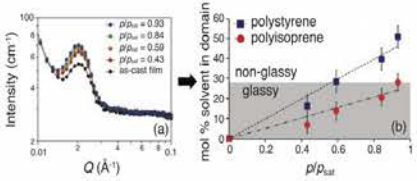

FIGURE 3: (a) SANS intensity profiles as a function of p/p_{sat}. (b) Solvent content in PS and PI domains calculated from broad peak model fits to SANS intensity profiles indicated that at a p/p_{sat} value of 0.59 the normalized *d*-benzene mol % in the PS domain (moles *d*-benzene in PS divided by moles *d*-benzene plus PS) was not high enough to reduce the T_g below 25 °C, which resulted in a glassy PS domain (gray shaded region) with limited mobility; the PI is always non-glassy at 25 °C.

To understand the cause of the structural transition, azimuthally averaged 1-D intensity profiles from *in situ* SANS, taken at the NGB 10 m SANS, (Figure 3a) were analyzed to quantify the solvent uptake in each domain as a function of p/p_{sat} (Figure 3b). Figure 3b revealed that at a p/p_{sat} value of 0.59, there was not a sufficient concentration of solvent to reduce the PS T_g below 25 °C (25-30) % by mole [2], and the PS domain transitioned to a glassy state. The p/p_{sat} value at which the glassy/non-glassy transition occurred matched with the p/p_{sat} value at which the restructuring mechanism, (measured with NR) changed, providing the final piece to the SVA mechanism.

In summary, we related measurable differences in L_z, n, and film thickness to in-plane and out-of-plane solvent profiles determined with SANS and NR, respectively. The ability to add polymer-solvent contrast (*via d*-benzene) allowed us to relate both polymer-polymer and polymer-solvent interactions to the reorganization of nanostructures during SVA. Thus, we determined how solvent preferentially diffuses into individual domains, tracked solvent diffusion and nanostructure reorganization as a function of p/p_{sat}, and monitored the kinetic trapping of nanostructure reorganization with solvent removal. Finally, we demonstrated that L_z can be controlled by manipulating the solvent content in the film and the swelling/drying pathway. These outcomes help define several of the underlying mechanisms that govern self-assembly in BP thin films subjected to SVA, such as the mobility required to restructure the domain lattice, the impact of surface and interfacial roughness on commensurability constraints, the trapping of solvent in the film as a function of polymer mobility, and the selectivity of polymer and solvent at the free and substrate surfaces, which can facilitate the prediction of ideal solvent annealing conditions depending on the objectives.

References

[1] C. K. Shelton, R. L. Jones, J. A. Dura, T. H. Epps, III, (2016) in review.
[2] J. E. Mark, Physical Properties of Polymers Handbook, (Springer Science & Business Media, LLC, New York, 2007) p. 191.
[3] M. Luo, J. E. Seppala, J. N. L. Albert, R. L. Lewis, N. Mahadevapuram, G. E. Stein, T. H. Epps, III, Macromolecules **46**, 1803 (2013).

SOFT MATTER

Biology

Biology is another significant area of science where neutron reflectometry and diffraction studies have been applied at the NCNR. Many people have been involved in this endeavor as well, both staff and external colleagues including Steve White, Doug Tobias, Mike Kent, Kent Blasie, Larry Kneller, Klaus Gawrisch, Ursula Perez-Salas, Duncan McGillivray, Jarek Majewski, Stephen Holt, Jeremy Lakey, and Anton Le Brun. Collaborations with Anne Plant, Curt Meuse, John Elliott and others in various divisions at NIST also proved very fruitful.

Part 3: Application of polarized neutrons and ferromagnetic reference layers to phase-sensitive neutron reflectometry studies of the structure of soft condensed matter systems

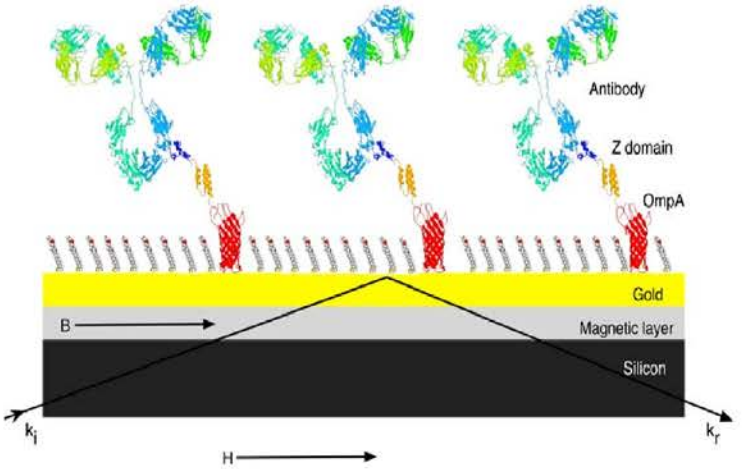

(Figure from the work of Anton Le Brun et al.)

Steve White, Ursula Perez-Salas, Mike Kent, and Kent Blasie, CW from top left.

Phase Sensitive Neutron Reflectometry on a Water-Cushioned Biomembrane-Mimic

Biomimetic membranes have been developed as models of living cell membranes, and this has applications in the quest for biocompatibility of inorganic materials in biologically active mediums, such as coatings for artificial organs. A membrane consists of a lipid bilayer (two lipid layers) where hydrophobic carbon chains form the inside of the membrane and their polar head groups the interface with the aqueous surrounding medium. A supported membrane-mimic consists of a lipid-like bilayer, typically attached to a single-crystal substrate, with access to water only at the top surface [1, 2]. Here we use neutron reflectometry to study a system in which water has access to both sides of a membrane-mimic attached to such a substrate, thus making the system a closer mimic to a real cell membrane.

The system devised by Liu *et al.* [3] consists of a water-swellable polyelectrolyte that electrostatically binds to the substrate and acts as a "cushion" for the membrane, not unlike the cytoskeletal support found in actual mammalian cell membranes. The lower half of the membrane-mimic is a terpolymer that attaches to the polyelectrolyte. A phospholipid layer forms on top of the terpolymer and the bilayer is finally chemically crosslinked for added stability. The system is shown schematically in Fig. 1.

Neutron reflectivity measurements were performed at the NG-1 vertical stage reflectometer to obtain the compositional profile at every step of the assembling process of the membrane-mimic which consisted of three stages: a) polyelectrolyte multilayer (PE), b) polyelectrolyte multilayer plus terpolymer (PE+TER), and c) polyelectrolyte multilayer plus terpolymer plus phospholipid layer (PE+TER+PC) [4]. The spatial resolution attained was approximately 10 Å, about half the thickness of a membrane bilayer, making it possible to distinguish the two layers of a membrane but not the structure of a single layer.

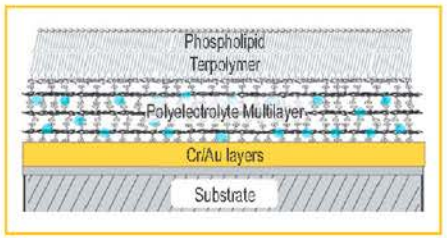

Fig. 1. Schematic diagram of a biomimetic membrane. The phospholipid layer at the top combines with the terpolymer layer to form a membrane-mimic that in turn resides on the water (blue dots) permeable "cushion" polyelectrolyte multilayer. The latter attaches electrostatically to the Au-capped substrate.

A unique compositional profile of the biomimetic film with no a priori knowledge of the sample's composition is obtained by measuring the reflectivity of equivalent samples made onto two substrates [5]. The substrates used were single crystal silicon (Si) and sapphire (Al_2O_3) coated with chromium (Cr) and then a gold (Au) layer to allow the polyelectrolytes to bind to a similar surface on both wafers.

Figure 2 shows the compositional profiles for the PE, PE+TER and PE+TER+PC assemblies in a D_2O atmosphere at 92 % relative humidity. The figure shows that the hydration of the PE layer is almost unaffected by the addition of the terpolymer and the phospholipid layer. Also, upon the addition of the phospholipid layer to the PE+TER assembly, the composite PE+TER+PC assembly shows an increase in thickness of approximately 30 Å, consistent with the formation of a single phospholipid layer at the surface. It is also clear that the addition of a phospholipid layer onto the terpolymer layer rearranges this region

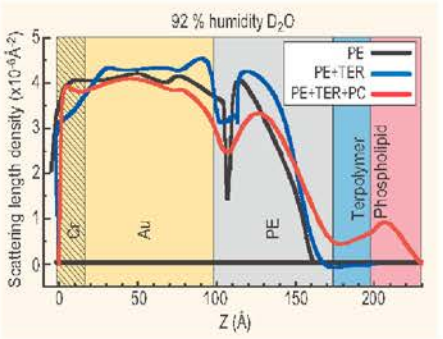

Fig. 2. Compositional profile of biomimetic membrane in a D_2O atmosphere at 92 % relative humidity at various stages of assembly on Au-capped substrate: only polyelectrolyte (PE), polyelectrolyte and terpolymer (PE+TER), polyelectrolyte, terpolymer and phospholipid (PE+TER+PC). The compositional profile is given by the scattering length density, SLD, profile when using neutrons.

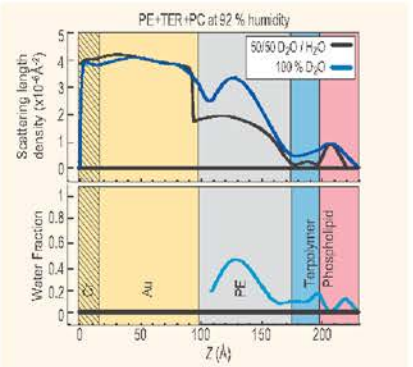

Fig. 3. Scattering length density profiles (top) and water fraction (bottom) for PE+TER+PC under indicated conditions.

significantly, since the terpolymer layer only becomes apparent after the phospholipid layer is added. It is possible to verify with an independent technique (contact angle) that the terpolymer was in fact deposited because it forms a hydrophobic outer layer. The outer surface becomes hydrophilic once the phospholipid layer is deposited onto the terpolymer layer.

Figure 3 (top) shows the profile for the PE+TER+PC assembly under 92 % relative humidity in 100 % D_2O and in 50/50 D_2O/H_2O. The overall thickness change due to the intake of water, in going from dry (not shown) to 92 % relative humidity, was found to be 20 Å. Figure 3 (bottom) shows the water fraction in the assembly under 92 % relative humidity. This is obtained by assuming that the distribution of each component in the layers is unaffected by having either D_2O or 50/50 D_2O/H_2O. From the figure it can be seen that the polyelectrolyte multilayer has a 40 % water uptake. This is a significant amount of water, which suggests that the polyelectrolyte multilayer can work as a "cushion" for membrane-mimetic systems. The terpolymer and the phospholipid layers contain an average of 10 % water, which is also significant, suggesting that these layers are not tightly packed.

The method of making equivalent samples on two substrates to obtain a unique compositional profile has a built-in congruency test, particularly useful in checking the reproducibility of the samples as well as the quality of the films. The test is to compare the calculated imaginary part of the complex reflectivity from the obtained profile with the corresponding data, as is shown in Fig. 4 for the PE+TER and PE+TER+PC assemblies. From Fig. 4 it is concluded that the PE+TER samples are homogenous and essentially identical while for the PE+TER+PC assembly, the

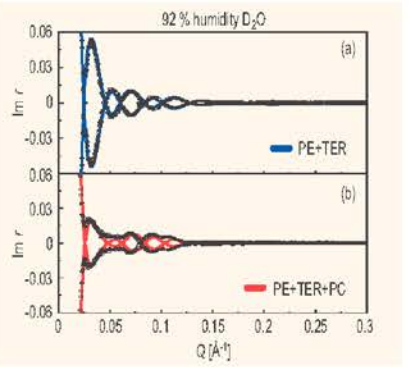

Fig. 4. Imaginary part of the complex reflectivity, Im $r(Q)$, data (symbols) and calculated curves (lines) obtained from the SLD profiles for the PE+TER and the PE+TER+PC assemblies shown in Fig. 2.

absence of true zeros, as indicated by the calculated curve, is suggestive of a small degree of sample inhomogeneity.

The system from Liu *et al.* has many characteristics desirable in a biomimetic membrane. It is a single membrane-mimic attached to a significantly hydrated soft "cushion" support that allows some membrane proteins to function. Thrombomodulin, a membrane protein relevant to blood-clotting, is being studied in this membrane-mimic environment to further develop biocompatible coatings for artificial organs [6].

References

[1] E. Sackmann, Science **271**, 43 (1996).

[2] A. L. Plant, Langmuir **15**, 5128 (1999).

[3] H. Liu, K. M. Faucher, X. L. Sun, J. Feng, T. L. Johnson, J. M. Orban, R. P. Apkarian, R. A. Dluhy, E. L. Chaikof, Langmuir **18**, 1332 (2002).

[4] U. A. Perez-Salas, K. M. Faucher, C. F. Majkrzak, N. F. Berk, S. Krueger, E. L. Chaikof, Langmuir **19**, 7688 (2003).

[5] C. F. Majkrzak, N. F. Berk, U. A. Perez-Salas Langmuir **19**, 1506 (2003).

[6] J. Feng, P. Y. Tseng, K. M. Faucher, J. M. Orban, X. L. Sun, E. L. Chaikof, Langmuir **18**, 9907 (2002).

U. A. Perez-Salas
NIST Center for Neutron Research
National Institute of Standards and Technology, Gaithersburg, MD 20899-8562

K. M. Faucher
Emory University School of Medicine, Atlanta, GA 30322

C. F. Majkrzak, N. F. Berk, S. Krueger
NIST Center for Neutron Research
National Institute of Standards and Technology
Gaithersburg, MD 20899-8562

E. L. Chaikof
Emory University School of Medicine
Atlanta, GA 30322

The next series of slides shows a NR study of the location of water within a particular biomimetic membrane of interest to a vascular surgeon (who is attempting to develop synthetic replacements for arteries and veins in medical applications). Such synthetic vessels must have bio-compatible coatings which won't foster an immune system response.

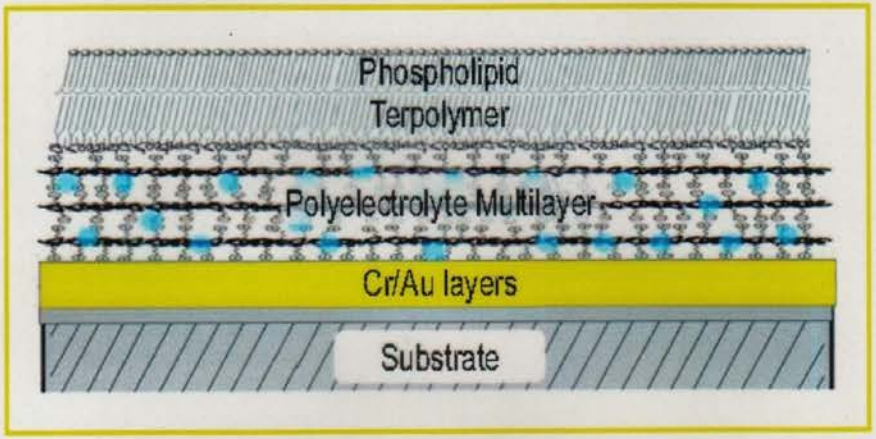

Fig. 1. Schematic diagram of a biomimetic membrane. The phospholipid layer at the top combines with the terpolymer layer to form a membrane-mimic that in turn resides on the water (blue dots) permeable "cushion" polyelectrolyte multilayer. The latter attaches electrostatically to the Au-capped substrate.

(Work of Ursula Perez-Salas, K. Faucher, E. Chaikof, et al.)

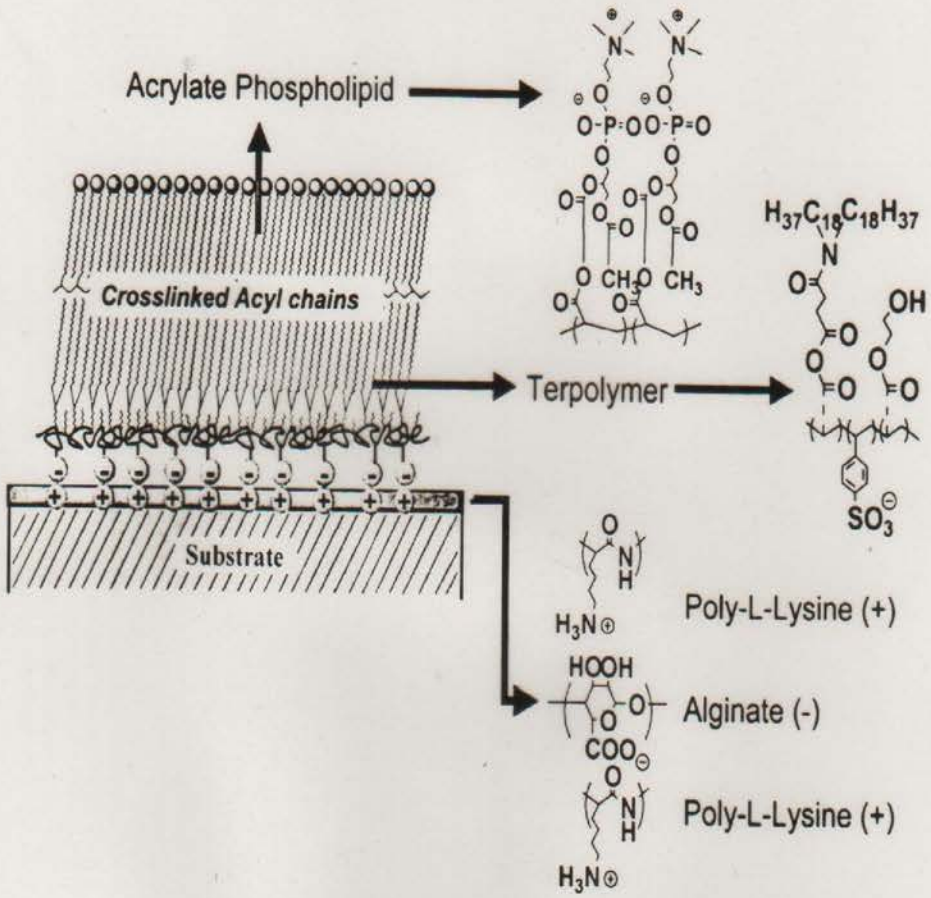

Figure 1:

1 Schematic representation the terpolymer (TER)-acrylate phospholipid (PC) membrane mimic supported on a polyelectrolyte multilayer(PE) "cushion". . . . . .

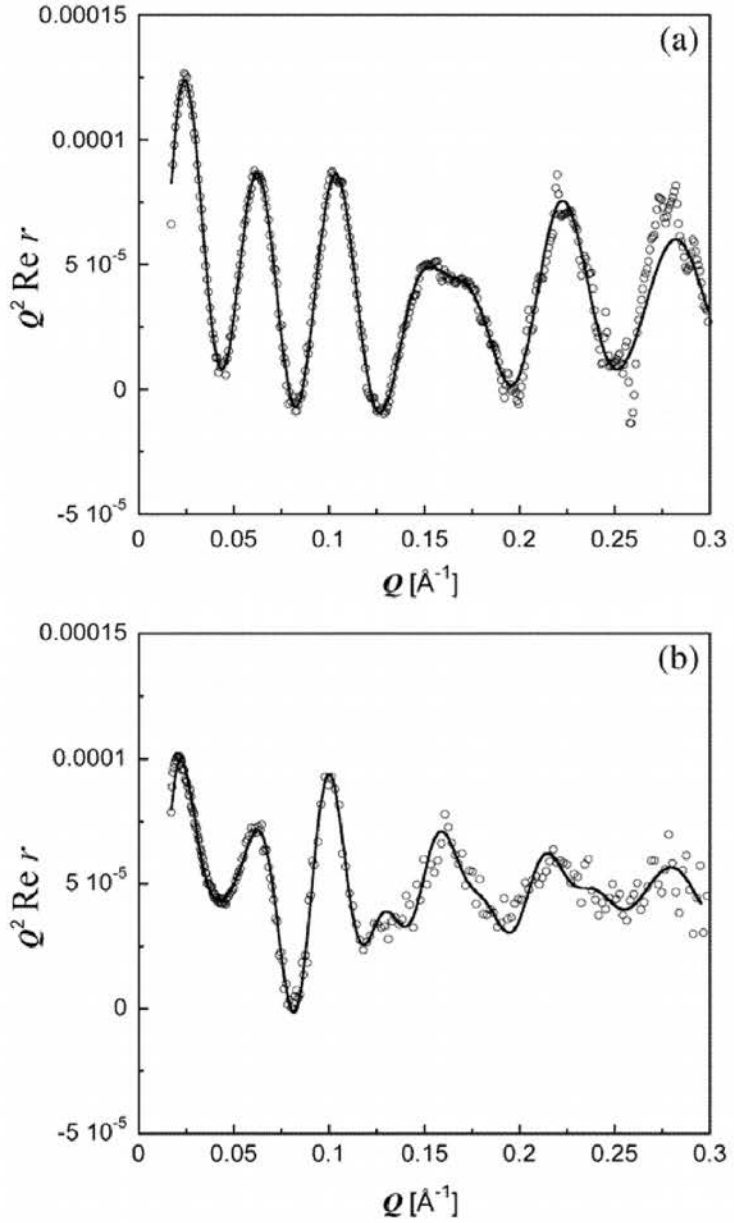

Typical real parts of reflection amplitudes obtained via phase-senistive neutron reflectometry methods for the biomimetic film structure presented in the previous slides.

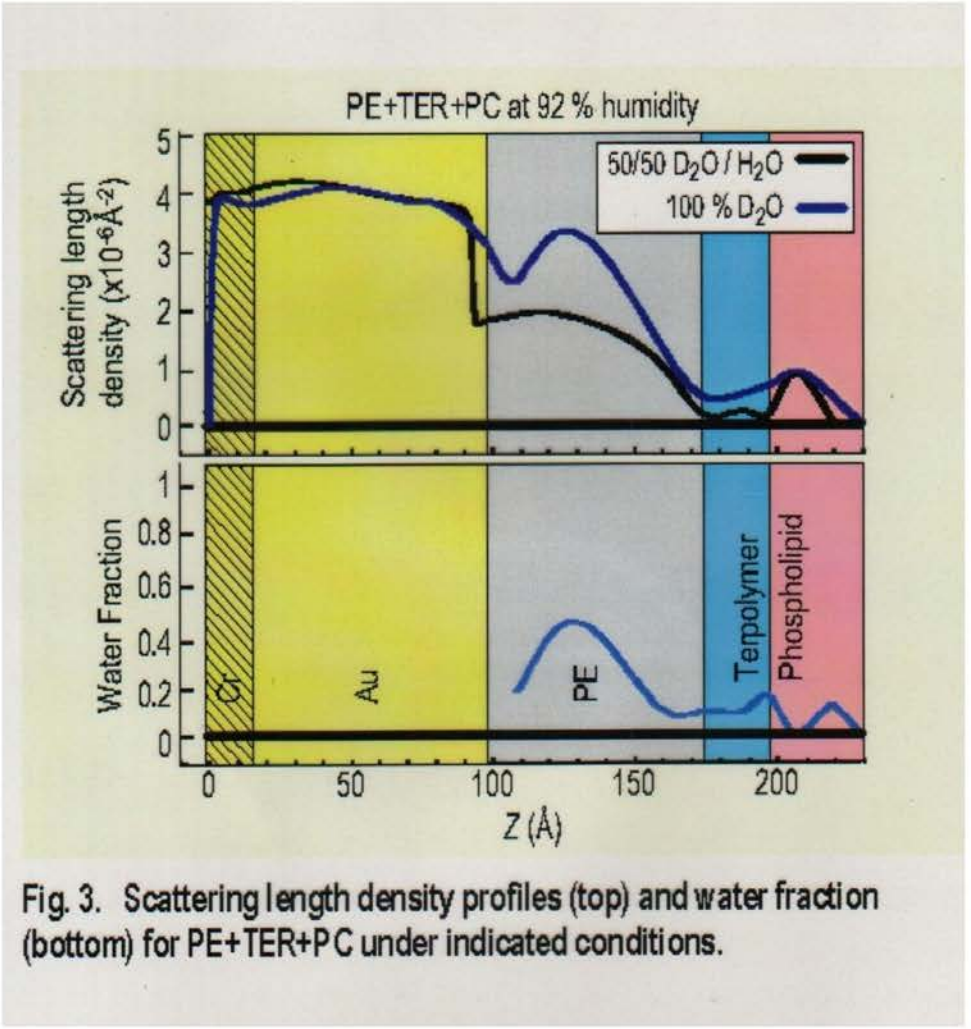

Fig. 3. Scattering length density profiles (top) and water fraction (bottom) for PE+TER+PC under indicated conditions.

After a number of different reflectivity measurements with various aqueous reservoir contrast values for H2O / D2O ratios, it was possible to deduce, from the analysis of that data, the water distribution across the thickness of the film structure. As shown in the figure above, the water is found to reside primarily within the poly-electrolyte layer.

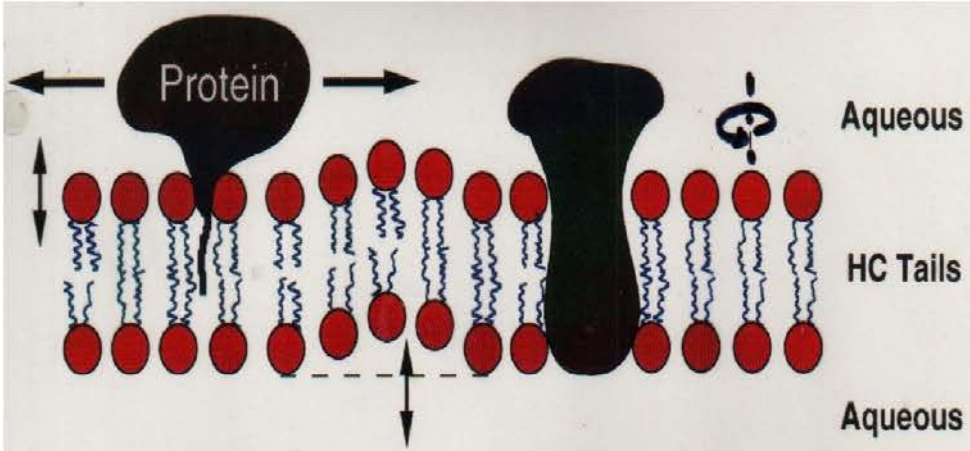

Supported Lipid Bilayers

A model system to mimic the structure and dynamics of cell membranes.

Proteins in Lipid Bilayers

- Difficult to characterize by traditional x-ray crystallography.
- Play a crucial role in cell function
  - regulate ion and nutrient transport
  - engage in binding, signalling and cell recognition
  - participate in cell fusion events.

Biosensors (Anne Plant & coworkers)

Melittin in Hybrid Bilayer Membranes

S. Krueger, A. Plant, et al., NIST (Langmuir)

- pore-forming toxin
- used as model membrane peptide
- active in HBMs

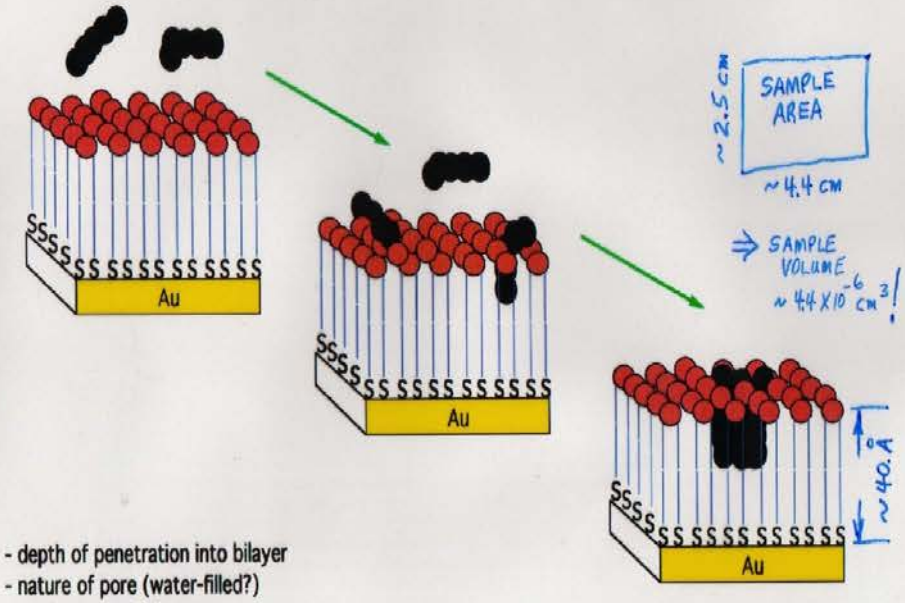

- depth of penetration into bilayer
- nature of pore (water-filled?)
- conformational changes
- random or ordered distribution?
- influence on surrounding lipids (location, conformation)

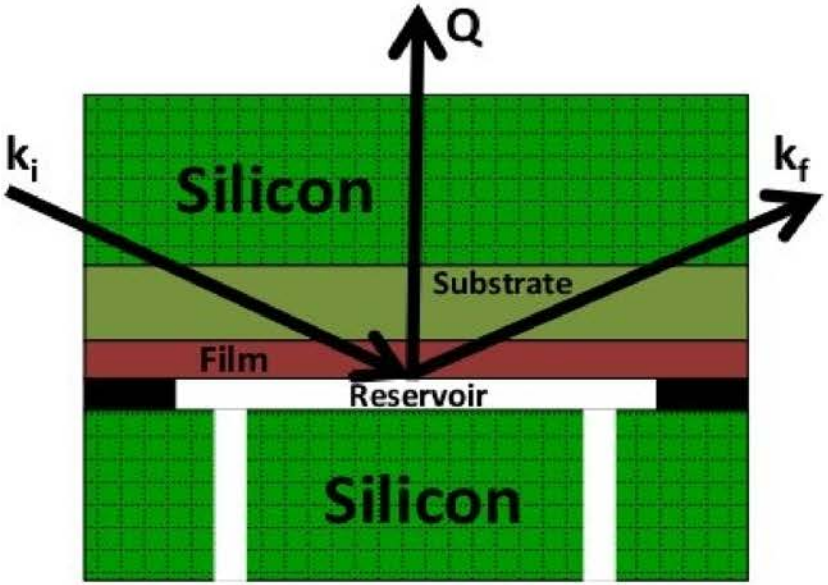

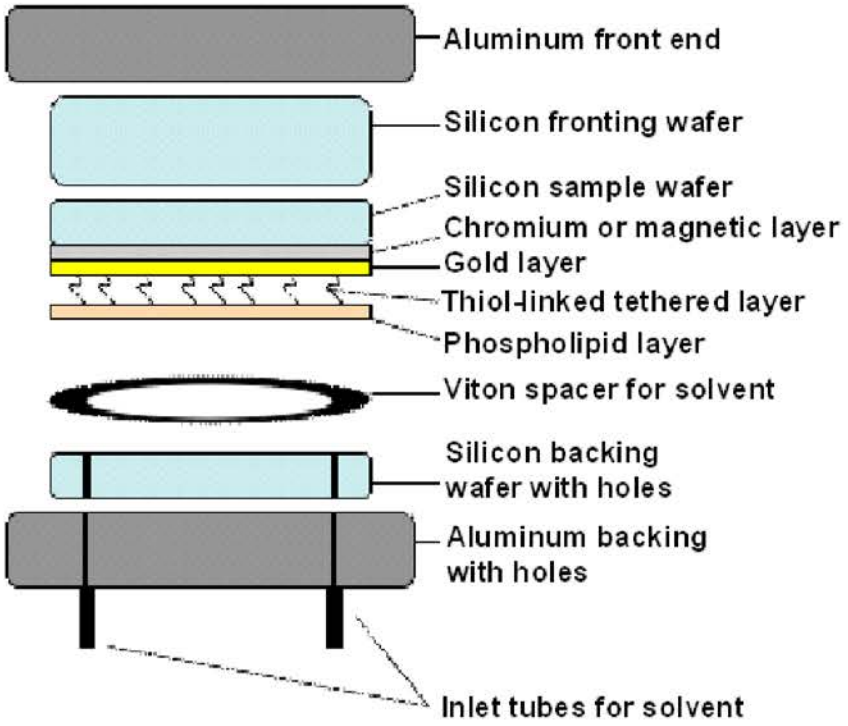

Proper design of a fluids cell is essential for optimizing the signal-to-noise ratio in neutron reflectivity measurements.

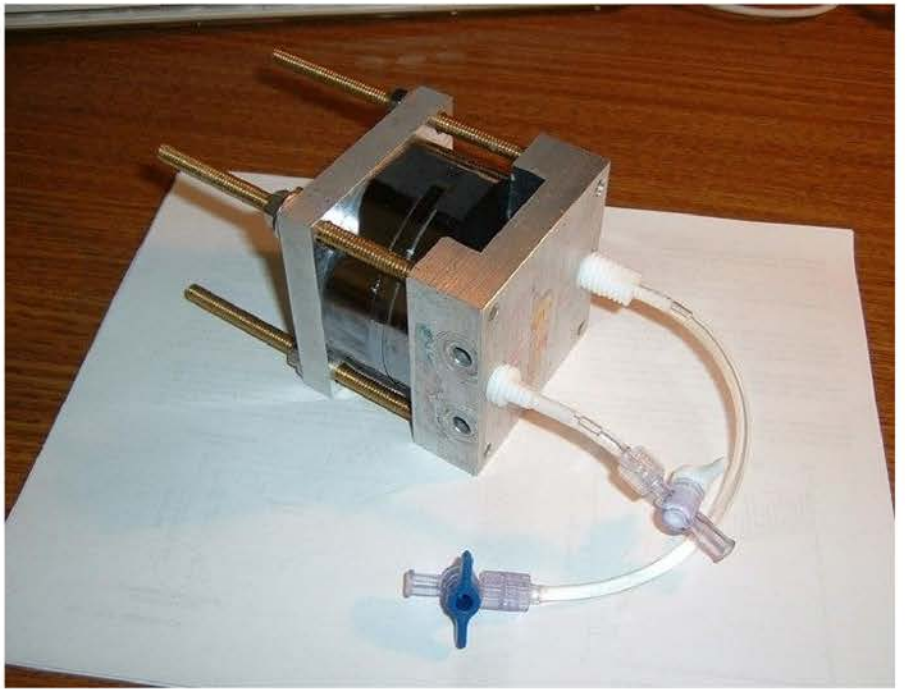

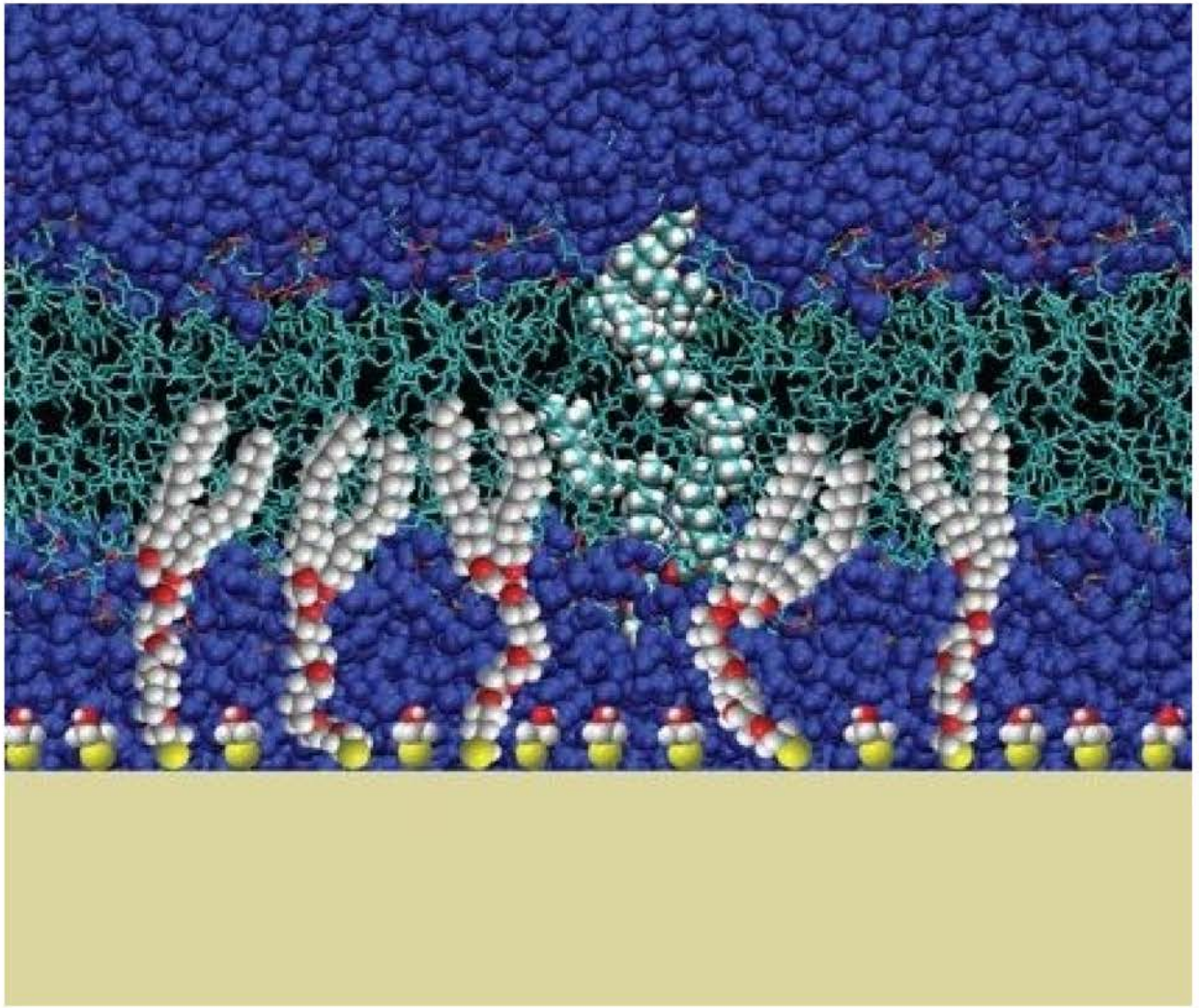

<> David Vanderah (NIST) biochemist extraordinaire – created tethered lipid bilayer membrane structures with almost perfect homogeneity and coverage over macroscopic surfaces.

<> Molecular dynamics simulations by experts such as Doug Tobias (UC Irvine) and Joseph Curtis (NCNR) can be essential in the analysis of corresponding neutron reflectivity measurements.

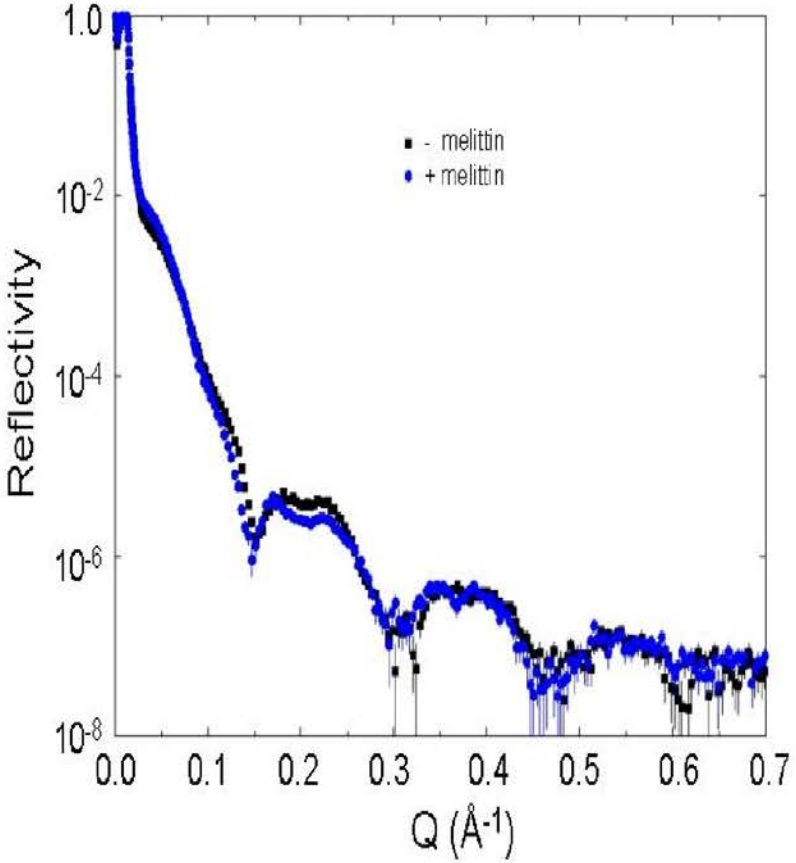

Specular neutron reflectivity data sets collected from a lipid bilayer membrane with and without exposure to melittin. Even on this log scale, significant differences are observable all across the reflectivity curves. Measurements of the reflectivity were obtained over nearly eight orders of magnitude and out to a Q of 0.72 inverse Angstroms -- which corresponds to a real space resolution of a fraction of a nano-meter in the SLD depth profile.

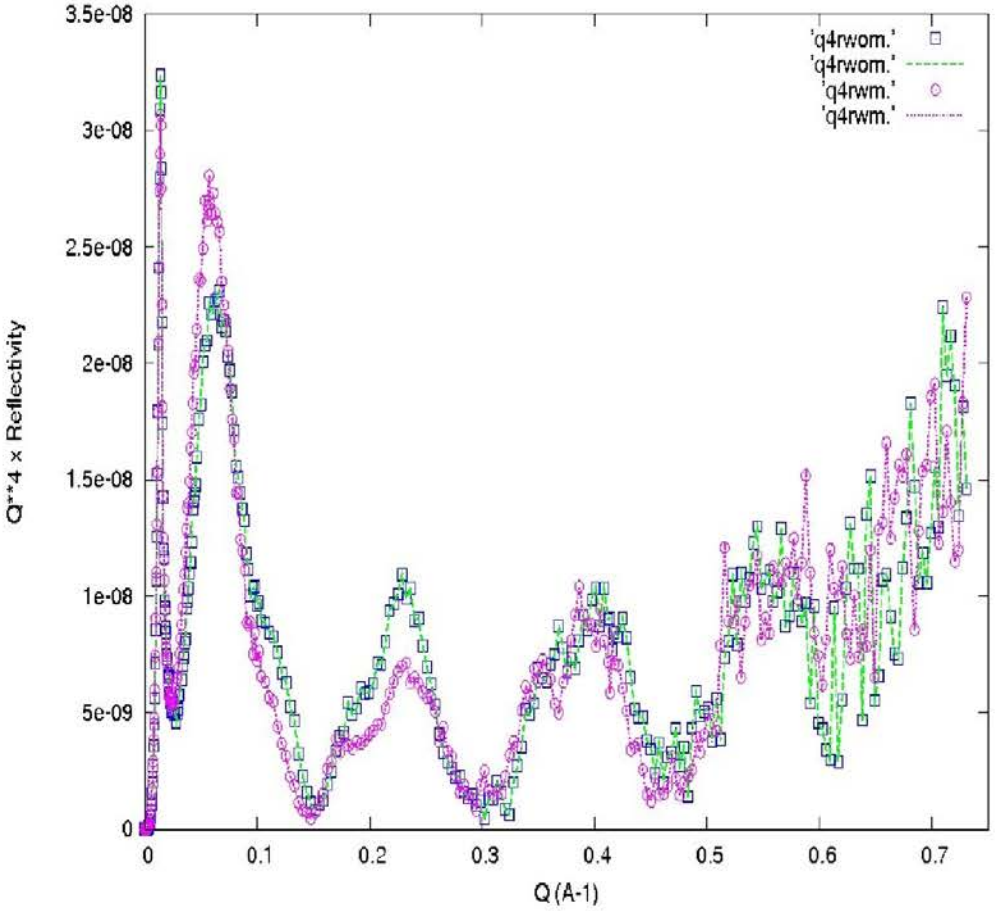

Multiplying the reflectitivities of the previous slide by Q^4 enhances the differences between the data obtained with and without melittin.

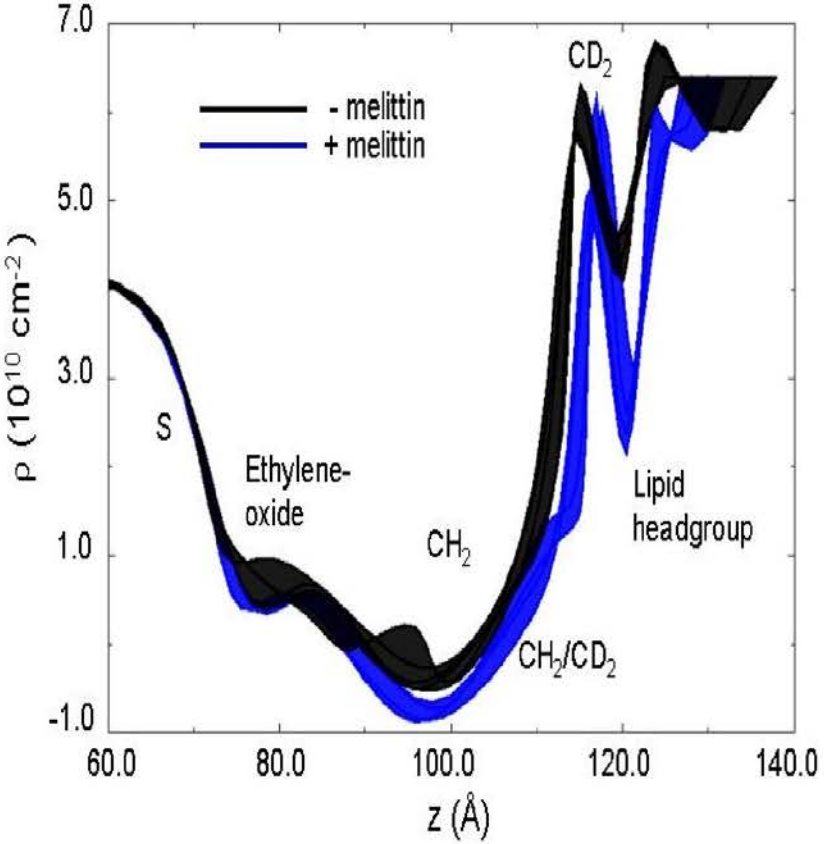

The scattering length density profiles obtained from fitting the reflectivity data -- the thickness of the plotted lines are a measure of the uncertainty in the SLD values. The data suggest that the melittin molecules perturb the outer leaflet of the bilayer membrane but do not penetrate significantly deeper.

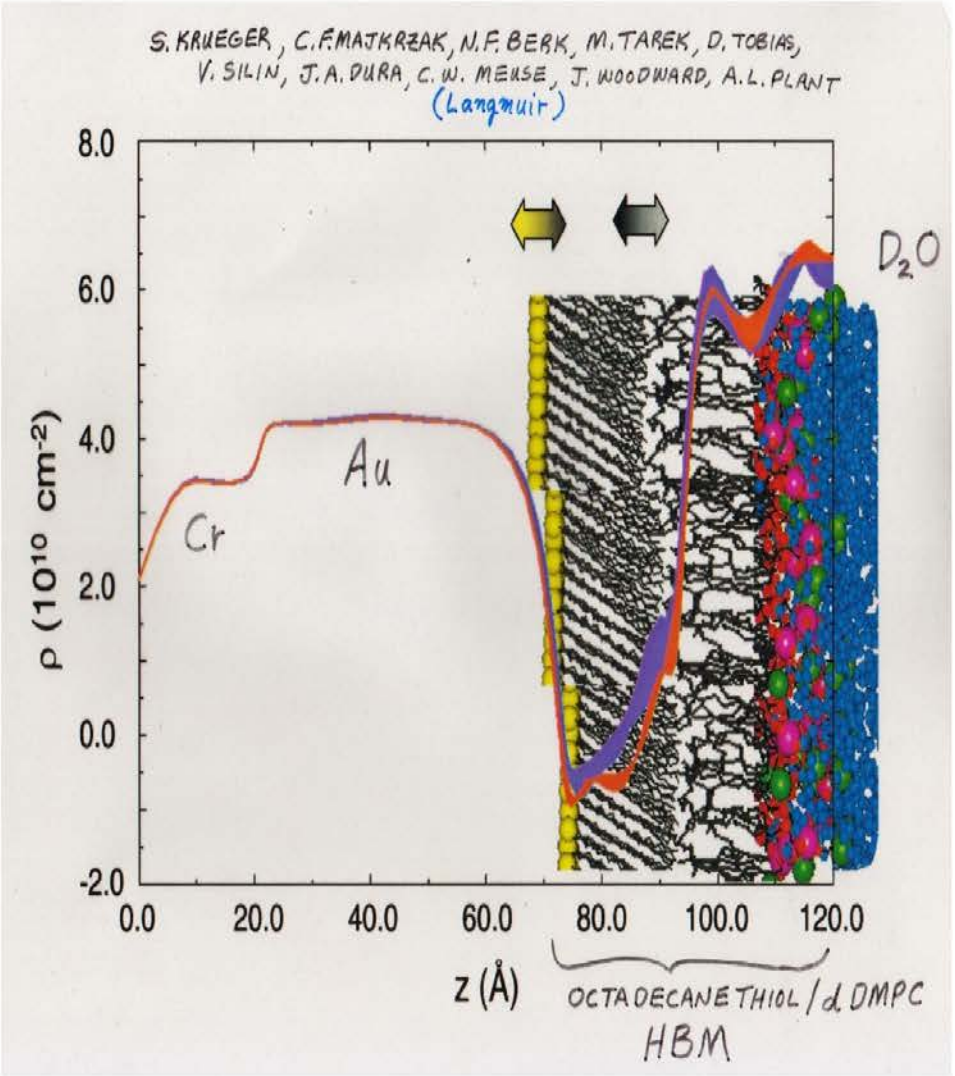

Comparison of the SLD profile for the lipid bilayer (without melittin) as obtained from the specular neutron reflectivity measurement with that predicted by a molecular dynamics simulation.

A sampling (on this and the next slide) of more recent specular NR studies of compositional depth pofiles of biological macro-molecules attached to or embedded in lipid bilayer membranes. These results are remarkable -- if not spectacular (at least in my opinion)!

Water-soluble membrane-associated proteins

>50% of biological NR beam time for biomedical applications using tBLMs

Active projects (last 2 cycles):

- Dengue
- Gaucher's disease
- GRASP
- HIV Gag & antibodies
- RSV & MLV
- Neurotransmitter
- OmpA/LA
- Parkinson's disease
- PTEN Tumor surpressor
- T-Cell receptor

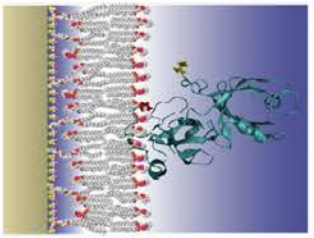

GRASP orientation at a tethered bilayer lipid membrane (tBLM) as determined by NR

Collaborative staff involvement:

- experimental planning
- substrate preparation
- tether synthesis
- neutron measurement
- data analysis

Bulent Akgun, Frank Heinrich, Mathias Lösche, Duncan McGillivray, Hirsh Nanda, David Vanderah

Typical reflectometry data for tBLM experiments

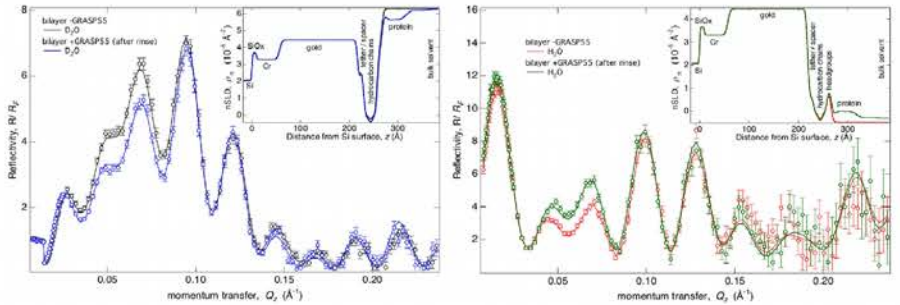

NR data measured on NG7, and best-fits for GRASP association with lipid membranes, project with A. Linstedt, University of Pittsburgh

Bulent Akgun, Frank Heinrich, Mathias Lösche, Duncan McGillivray, Hirsh Nanda

Example: Dengue Virus Envelope Protein

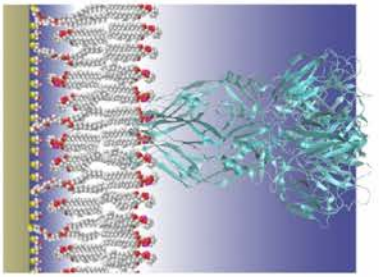

Visualization. Project with Mike Kent, Sandia National Labs.

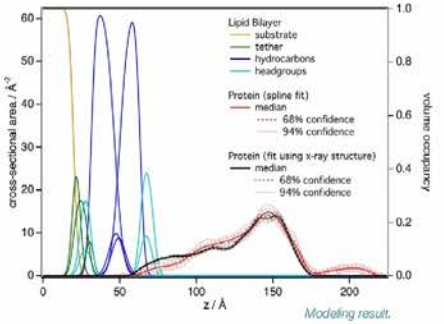

Modeling result.

- Monte-Carlo Markov Chain uncertainty analysis
- Composition-space modeling of the bilayer
- Free-form fitting of structurally unknown components of the architecture
- Usage of PDB structure files for position and orientation of rigid proteins

Bulent Akgun, Frank Heinrich, Paul Kienzle, Sushil Satija

www.ncnr.nist.gov/programs/reflect/

Combining NR with Molecular Simulations

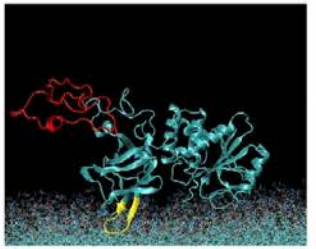

MD simulation snapshot of PTEN tumor suppressor association with a PS-containing lipid membrane

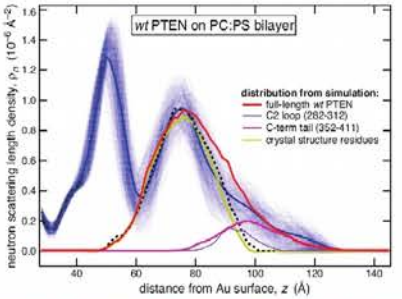

Comparison of MD and NR results, Shenoy, S. et al., J. Struct. Biol. 1–15 (2012).

Comparison of experimental data with results from:

- MD simulation
- Monte Carlo conformational search (SASSIE) results

Future Challenges:

- Ensemble averaging, integrating NR and simulation

Joseph Curtis, Mathias Lösche, Hirsh Nanda

An ion-channel-containing model membrane: structural determination by magnetic contrast neutron reflectometry†

Stephen A. Holt,*[a] Anton P. Le Brun,[b] Charles F. Majkrzak,[c] Duncan J. McGillivray,‡[c] Frank Heinrich,[cd] Mathias Lösche[cd] and Jeremy H. Lakey[b]

Received 15th December 2008, Accepted 17th March 2009
First published as an Advance Article on the web 20th May 2009
DOI: 10.1039/b822411k

To many biophysical characterisation techniques, biological membranes appear as two-dimensional structures with details of their third dimension hidden within a 5 nm profile. Probing this structure requires methods able to discriminate multiple layers a few Ångströms thick. Given sufficient resolution, neutron methods can provide the required discrimination between different biochemical components, especially when selective deuteration is employed. We have used state-of-the-art neutron reflection methods, with resolution enhancement *via* magnetic contrast variation to study an oriented model membrane system. The model is based on the *Escherichia coli* outer membrane protein OmpF fixed to a gold surface *via* an engineered cysteine residue. Below the gold is buried a magnetic metal layer which, in a magnetic field, displays different scattering strengths to spin-up and spin-down neutrons. This provides two independent datasets from a single biological sample. Simultaneous fitting of the two datasets significantly refines the resulting model. A β-mercaptoethanol (βME) passivating surface, applied to the gold to prevent protein denaturation, is resolved for the first time as an 8.2 ± 0.6 Å thick layer, demonstrating the improved resolution and confirming that this layer remains after OmpF assembly. The thiolipid monolayer (35.3 ± 0.5 Å), assembled around the OmpF is determined and finally a fluid DMPC layer is added (total lipid thickness 58.7 ± 0.9 Å). The dimensions of trimeric OmpF in isolation (53.6 ± 2.5 Å), after assembly of lipid monolayer (57.5 ± 0.9 Å) and lipid bilayer (58.7 ± 0.9 Å), are precisely determined and show little variation.

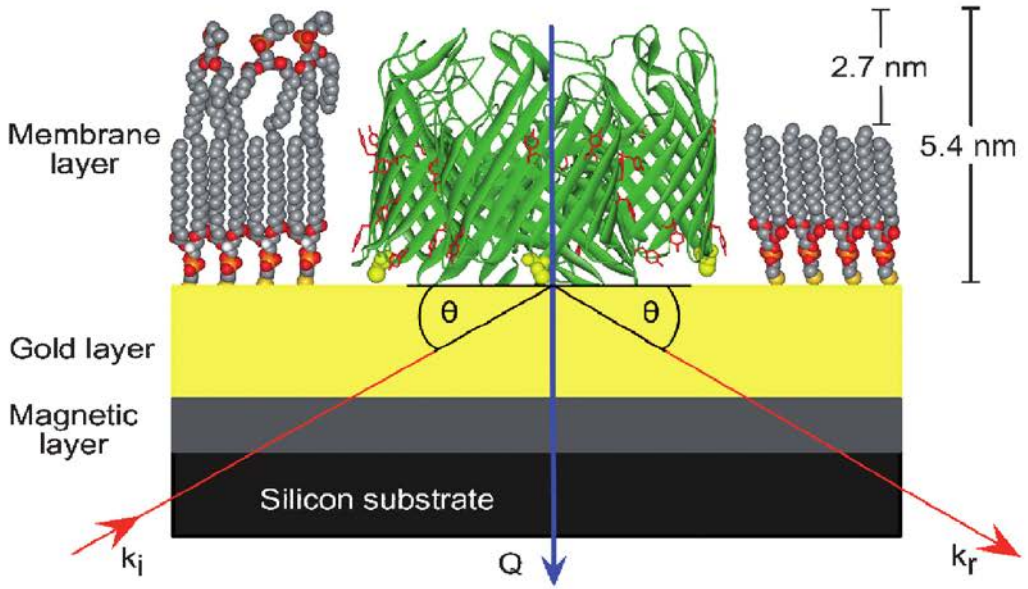

Fig. 1 Schematic of the sample configuration for the neutron reflection studies. The substrate was exposed to a 1% (v/v) βME in ethanol solution.[32] OmpF-E183C (300 μg ml^{-1} in buffer A) was incubated on the gold surface for at least 3 hours at room temperature. After incubation, the surface was washed, first with a 2% (w/v) SDS solution and then with distilled water, to remove any non-specifically bound protein. Thiolipid DPPTE (1,2-dipalmitoyl-*sn*-glyero-3-phosphothioethanol), (1.0 mg ml^{-1} in buffer A), was then deposited to infill around the OmpF trimers (right-hand side of figure). Finally DMPC (10 mg ml^{-1} in ethanol) was added to the assembled surface (left-hand side of figure) and incubated for 5 minutes. The DMPC solution was removed by washing the cell quickly with 50 ml of buffer B. The figure shows an OmpF trimer (PBD 2OMPF[34]) attached to the gold *via* cysteine residues surrounded by DPPTE (pdb file 870160.mol from Avanti Polar Lipids). DMPC molecules used to represent the upper layer are taken from a simulated DMPC bilayer structure.[61] The cysteine residues are yellow and space-filled, and a belt of tyrosine residues (wire frame, red) delineates the bilayer interface in the bacterial membrane region. The incident neutron beam (red arrow labelled k_i) was directed to reflect (k_r) from the back of the complex interfacial structure. The blue arrow labelled Q shows the scattering vector.

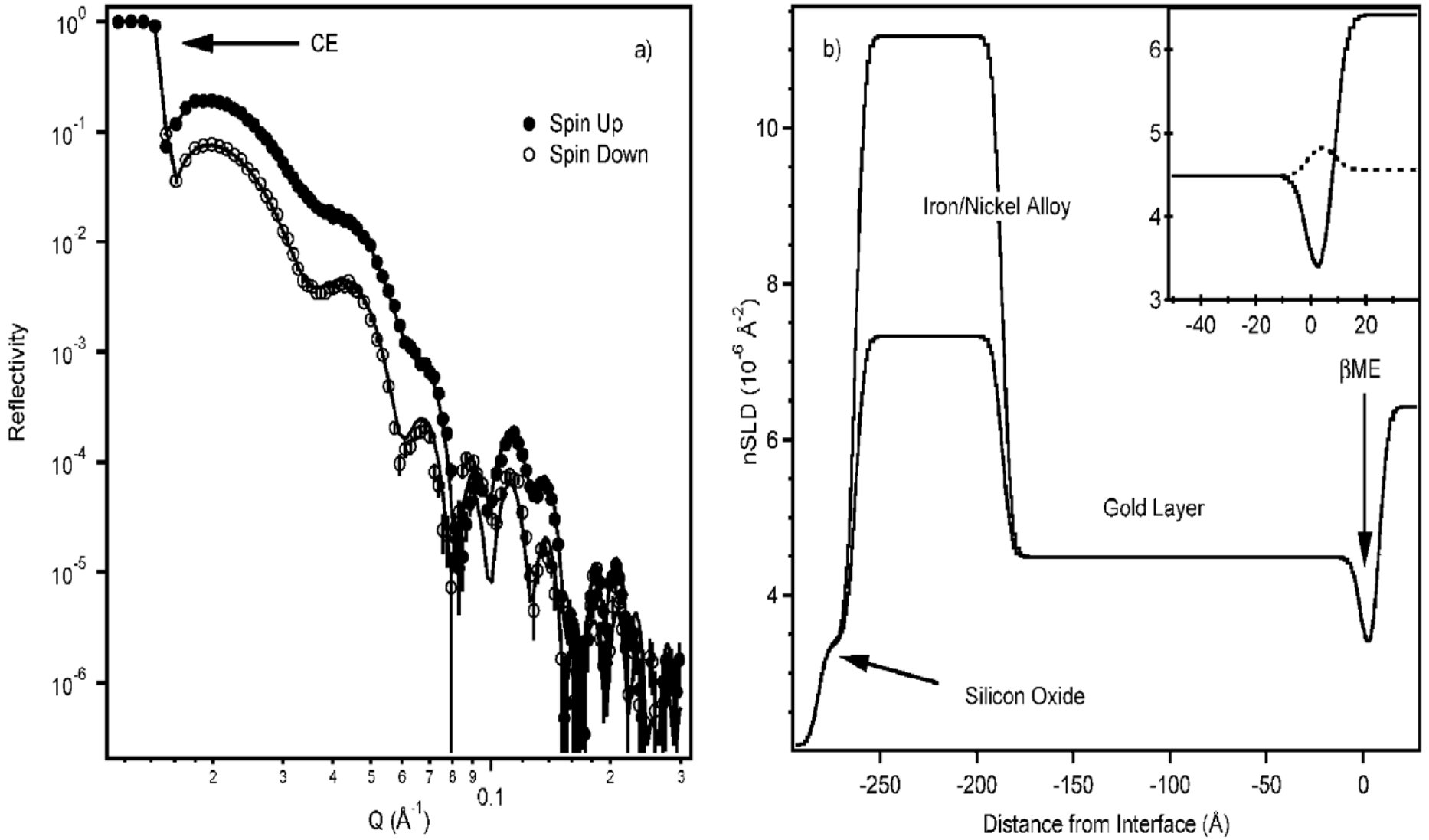

Fig. 2 a) Reflectivity data (symbols) and fit (lines) after βME adsorption onto the surface, D_2O buffer. Below the critical edge (CE) the neutrons are totally externally reflected and the reflectivity is unity. Q is the scattering vector defined in eqn (1). The separation in the data results from the different contrast of the magnetic layer to spin-up and spin-down neutrons. b) Real-space nSLD profile corresponding to the fit shown in a). The zero point has been set at the interface between the gold and the βME. The silicon substrate is on the left and D_2O buffer on the right. The twp different nSLD values for the magnetic layer are clearly seen. The hydrogenous βME layer is clearly evident between the gold and the buffer. The inset shows the βME region of the sample expanded with the dashed line the fit obtained with d-βME next to a gold-matched water buffer. Note: Data presented in Figs. 2 and 4 are all from successive depositions on the same substrate.

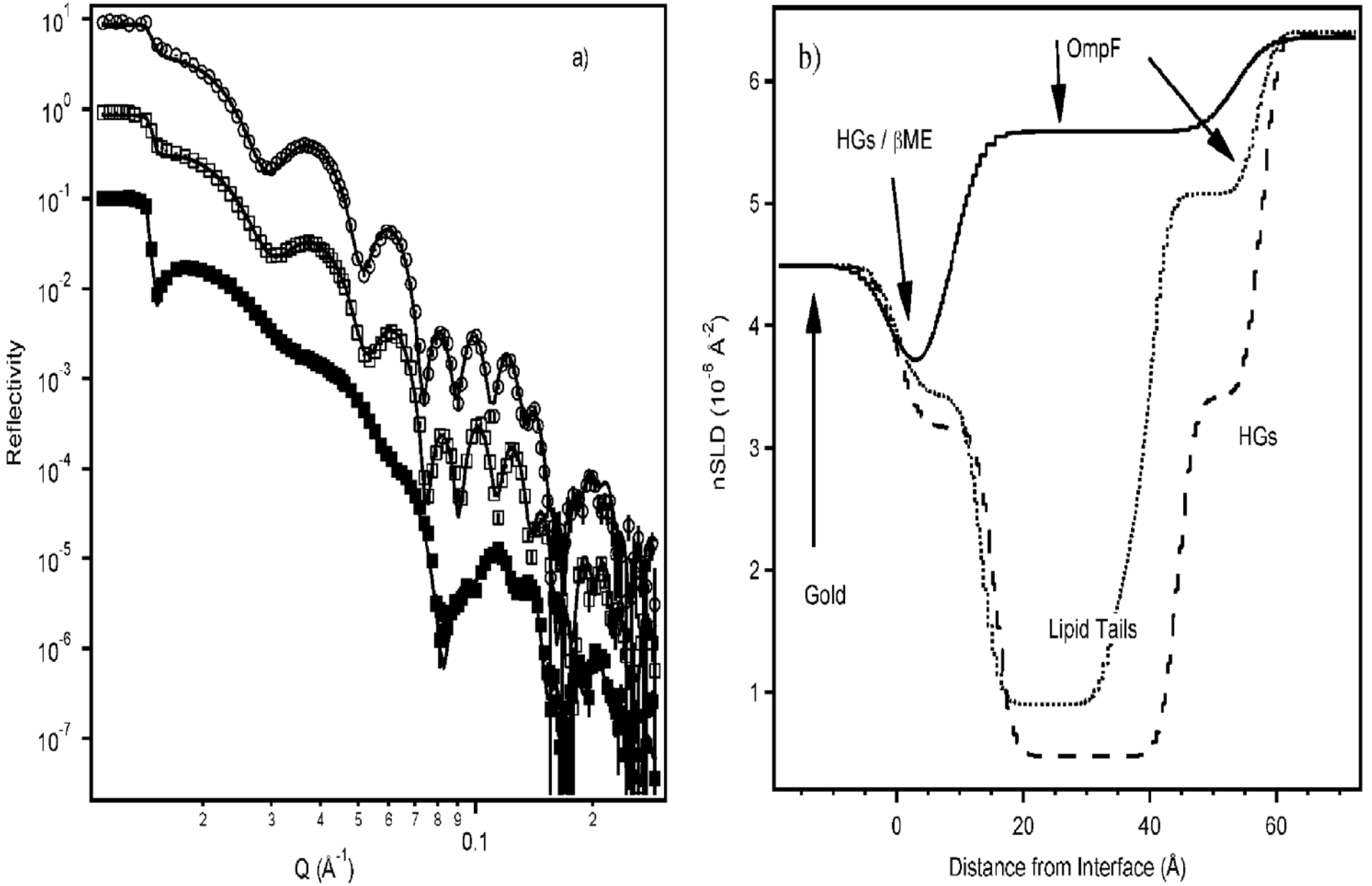

Fig. 4 a) Data, 'up polarisation' state (symbols) and fit (lines) after OmpF adsorption to a βME-passivated gold surface (■), subsequent DPPTE adsorption (□) and subsequent precipitation of DMPC (○). The OmpF and DMPC datasets have been offset for clarity. b) The real-space nSLD profiles corresponding to the fits of all polarisation data. Solid line – OmpF adsorption; dots – DPPTE adsorption; dashes – DMPC adsorption. The figure has been labelled to illustrate the main constituent of each region; HGs indicate regions of lipid headgroup.

Probing the Depths of Lipid Membranes with AND/R

M. Mihailescu
University of California at Irvine
Irvine, CA 92697 and
NIST Center for Neutron Research
National Institute of Standards and Technology
Gaithersburg, MD 20899

D. Worcester
University of Missouri
Columbia, MO 65211

Lipids are the major constituent of cellular membranes. Arranged as a two-molecule-thick bilayer with a thickness of about 50 Å, they insulate the inside of cells and cell organelles from the outside. Proteins embedded in this bilayer provide the only conduits between the two sides. Intriguingly, the structures of the embedded proteins are shaped by lipid-protein interactions. In order to understand and describe these interactions quantitatively, the structures of lipid bilayers of varying lipid compositions must be determined. Neutron diffraction is a powerful tool for this purpose, as we illustrate in this brief report. We show how high instrumental resolution combined with contrast variation by hydrogen-deuterium substitution can yield a wealth of information about the structure of lipid bilayers. As an illustrative example, we present results from bilayer membranes containing cholesterol obtained during the 2004 Summer School on Neutron Scattering held at the NCNR.

The neutron diffraction data are among the first obtained using the Advanced Neutron Diffractometer/Reflectometer (AND/R), which became operational at the NIST Center for Neutron Research (NCNR) in September 2003. The AND/R was designed and optimized to meet the criteria of high resolution and efficiency that the biophysical community has long needed for studies of membrane structure. It was constructed by the Cold Neutrons for Biology and Technology (CNBT) research partnership funded principally by a grant from the NIH National Center for Research Resources awarded to the University of California at Irvine, with the additional support of NCNR, UC Irvine, and the Univ. of Pennsylvania. A highly monochromatic beam ($\Delta\lambda/\lambda$ = 1 % at a neutron wavelength λ of 5 Å), a system of computer driven slits to control the beam collimation and reduce the background caused by spurious scattering, and easy access to either a pencil detector or a 2D position-sensitive detector, are only a few of the merits of the AND/R.

Due to their dual hydrophobic-hydrophilic character, cell membrane lipids organize spontaneously into bilayers, causing the hydrophobic alkyl chains to be hidden in the bilayer center and the polar 'headgroups' to be exposed to water. The deposition of lipids from an organic solution on a solid substrate (silicon, quartz, or glass) generally results in a stack of bilayers aligned parallel to the substrate surface (Fig. 1). The samples used in our study were formed from dimyristoylphosphatidylcholine (DMPC) lipids in mixture with 0.20 mole fraction of cholesterol. Cholesterol, an essential component of mammalian membranes, participates in many physiological processes and plays an important role in organizing other lipids and membrane proteins. There is increasing evidence that it can associate preferentially with saturated lipids to form ordered domains called "rafts". These are believed to play an important role in signaling across cell membranes [1].

The usefulness of neutron diffraction for studies of DMPC-cholesterol and other membranes arises because membrane lipids and the surrounding water are rich in hydrogen atoms that can be selectively replaced with deuterium without changing the structure of the membrane. Because deuterium nuclei coherently scatter neutrons much more strongly than protons, this selective deuteration allows the deuterated atoms to be readily identified, as described below.

The structural information sought in our experiments was the scattering profile of the DMPC-cholesterol bilayers. Such profiles show how the lipid mass (scattering length density) is distributed across the thickness of the membrane. Specular diffraction on oriented lipid multilayers, (i.e. diffraction where the beam incident and emergent angles relative to the sample surface are equal), produces a diffraction peak at Bragg angles θ given by $n\lambda = 2d\sin(\theta)$, where n is the (integer) order of diffraction, and d the spacing of the layers. $Q_z = 2\pi/d$ is the scattering wavevector (Fig. 1).

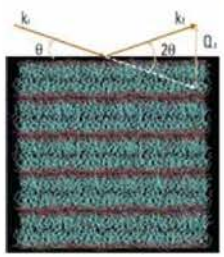

FIGURE 1:
A Molecular Dynamics simulation snapshot, performed for a stack of dioleoylphosphocholine bilayers at 66 % relative humidity, and T = 300 K. The incident (k_i) and emergent (k_f) neutron wave-vectors, and their resultant ($Q = Q_z$), are displayed, as in a specular set-up. Image courtesy of Francisco Castro-Román and Ryan Benz (University of California at Irvine).

In our experiments, the DMPC lipids were deuterium-labeled near the ends of the alkyl chains. A system of 4000 bilayers deposited on a thin glass slide was mounted vertically in the beam in a sealed sample chamber at room temperature and a controlled relative humidity of 66 %. Fig. 2 shows two sets of diffraction patterns collected in a specular set-up for two water-contrast conditions: 100 % H_2O and a mixture containing a 0.50 mole fraction of D_2O.

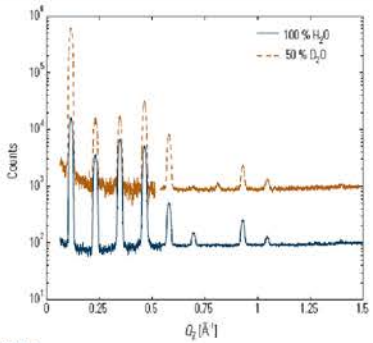

FIGURE 2:
The specular scattering intensities for oriented multilayers of DMPC + 0.20 mole fraction of cholesterol, measured at 66 % relative humidity and T = 22 °C, in two water contrast conditions. The data sets have been shifted vertically for better visibility.

The Fourier synthesis from all of the nine diffraction orders observed, in the first Born approximation [2], results in the density profile displayed in Fig. 3. The phase assignments for each diffraction order were determined from additional water contrast variation experiments [3]. A lipid bilayer is a thermally disordered system [4] (each atom will have a Gaussian distribution around its mean position in the bilayer). Nevertheless, a stack of bilayers has long-range order over experimentally accessible length scales, as is evident from the strong Bragg peaks in Fig. 2.

Previous work has shown that cholesterol increases the ordering of lipid alkyl chains within the bilayers of saturated lipids [2], but the mechanism of this ordering effect is still not very clear. The 9 orders of diffraction allow significant structural features of the bilayer to be resolved, such as the position and extension of the different submolecular groups (Fig. 3). At equilibrium, a few molecules of water are associated with the lipid polar headgroups. Therefore, replacing H_2O by D_2O in the vapor inside the sample chamber will alter the scattering-length density profile along the lipid axis (note the increase in the scattering length density close to the lipid headgroup, which peaks at position z = 27 Å, relative to the bilayer center). The bilayer thickness, as determined from the position of the diffraction maxima, is d = 54.1 Å, including the water associated with the lipid. The prominent feature appearing in the middle of the hydrocarbon region, located at 5.2 Å from the bilayer center, is due to the presence of the deuterium label near the end of the DMPC alkyl chains. Deuterium labeling at different positions along the lipids would allow determination of the positions of specifically-labeled atoms in the bilayer with a resolution of better than 1 Å.

Future experiments should reveal the exact position of cholesterol in the bilayer, the packing conformation of lipids in the presence of cholesterol, and ultimately the interplay between geometrical constraints and molecular interactions that drives the preferred association of cholesterol with certain lipids.

The Advanced Neutron Diffractometer/Reflectometer adds a powerful new instrument for structural investigations of materials at nanoscopic scales. The structural information obtained can be used in concert with molecular dynamics simulations to arrive at unprecedented dynamic structural models of lipid membranes.

We thank Prof. Stephen White for his valuable comments.

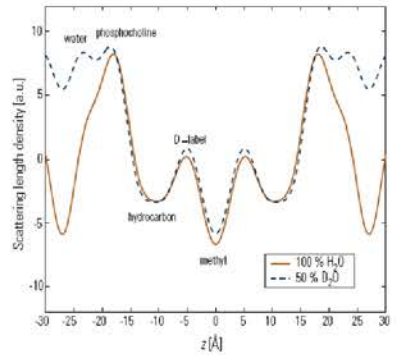

FIGURE 3:
Scattering-length-density profile for a bilayer of DMPC (deuterated near the end of the alkyl chains) in mixture with a 0.20 mole fraction of cholesterol, for two water contrast conditions: 100 % H_2O and a mixture containing 0.50 mole fraction of D_2O.

References:

[1] T. J. McIntosh, A. Vidal, S. A. Simon, Biophys. J. **85** (3), 1656, (2003).
[2] D. L. Worcester, and N. P. Franks, J. Mol. Biol., **100**, 359 (1976).
[3] D. Worcester *et al., in preparation.*
[4] S. H. White and M. C. Wiener In: *Permeability and Stability of Lipid Bilayers*, edited by E. A. Disalvo and S. A. Simon, Boca Raton: CRC Press, pp. 1-19 (1995).

Neutron reflectometry studies of membrane-bound tubulin reveal an amphipathic helical binding motif

D. P. Hoogerheide,[1] S. Yu. Noskov,[2] D. Jacobs,[3] L. Bergdoll,[4] V. Silin,[5] D. Worcester,[1] J. Abramson,[4,6] H. Nanda,[1,7] T. K. Rostovtseva,[3] and S. M. Bezrukov[3]

Bilayer lipid membranes (BLMs) form barriers that separate the interior from the exterior of the cell and divide the cell into specialized compartments called organelles. Proteins that are embedded into BLMs, known as membrane proteins, play diverse roles, including the transportation of various ions, metabolites, proteins, DNA, etc., across the BLMs, thus providing communication pathways between cells and between organelles inside cells. This function is so crucial for health and disease that while membrane proteins account for about 20 % of known proteins [1], they comprise 70 % of known drug targets [2]. In humans, mitochondria are the organelles responsible for energy conversion, with two main purposes: to store energy, and to produce heat that maintains body temperature. However, mitochondria themselves are also the sources of the reactive oxygen species that damage mitochondria, mitochondrial DNA, and other cellular components. Therefore, maintaining the appropriate conditions that provide sufficient energy for cellular functions and limit the production of chemically damaging reactive oxygen species is crucial for cell life and death. Recent evidence indicates that the regulation of this equilibrium is accomplished at least in part by a complex of the mitochondrial voltage-dependent anion channel (VDAC), a passive transport channel of the mitochondrial outer membrane (MOM), and dimeric tubulin [3], which is best known as a structural protein in microtubules. The association of tubulin with the MOM is particularly suggestive given the role of microtubule-targeting drugs (MTDs) in chemotherapy [4]. In this work we shed light on the role of dimeric tubulin in regulating mitochondrial bioenergetics by investigating the binding of tubulin to biomimetic mitochondrial membranes using a combination of neutron reflectometry (NR) and molecular dynamics (MD) simulations [5].

Tubulin is a heterodimer comprising α and β subunits, which have similar spatial arrangements but different amino acid sequences. In microtubules, the exposed end is always the β subunit; as a result, all MTDs bind to the β subunit [4]. Remarkably, in an *in vitro* system the rate of interaction between tubulin and a single VDAC channel was observed to depend strongly on the lipid composition of the BLM in which VDAC was embedded. In particular, the interaction rate increased by two orders of magnitude if a lamellar (i.e. preferring a flat membrane geometry) dioleoylphosphatidylcholine (DOPC) membrane was replaced with the non-lamellar (preferring a curved membrane geometry) dioleoylphosphatidylethanolamine (DOPE) [6], suggesting that tubulin is able to distinguish between these two lipid species. Furthermore, these results indicate that the first step of the VDAC-tubulin interaction involves tubulin binding to the lipid membrane surface.

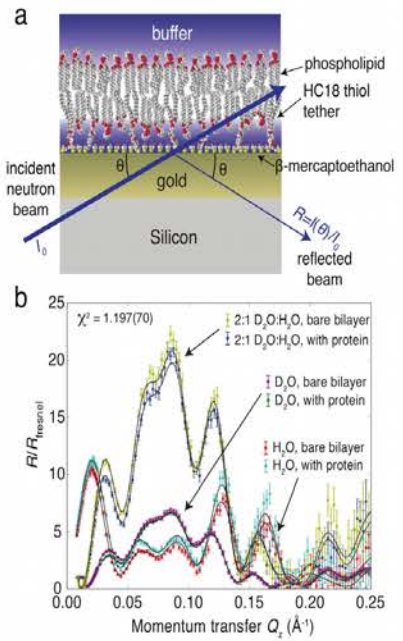

FIGURE 1: Neutron reflectometry (NR) experiment with a sparsely tethered lipid bilayer membrane (stBLM). (a) Schematic of the stBLM and scattering geometry. Sparse tethering is achieved by using β-mercaptoethanol as a spacer molecule. (b) NR data, showing the differences between the three deuteration levels of the buffer solutions. Data are normalized to the Fresnel reflectivity expected from a silicon/buffer interface. Solid lines show the fit to a theoretical model of the bilayer with bound tubulin.

[1] NIST Center for Neutron Research, National Institute of Standards and Technology, Gaithersburg, MD 20899
[2] University of Calgary, Calgary, AB, Canada, T2N 1N4
[3] Eunice Kennedy Shriver National Institute of Child Health and Human Development, National Institutes of Health, Bethesda, MD 20892
[4] University of California Los Angeles, Los Angeles, CA 90095
[5] University of Maryland, Rockville, MD 20850
[6] Institute for Stem Cell Biology and Regenerative Medicine, National Centre for Biological Sciences–Tata Institute of Fundamental Research, Bellary Road, Bangalore-560065, Karnataka, India
[7] Carnegie Mellon University, Pittsburgh, PA 15213

In this study, we determined the orientation of membrane-bound tubulin—and hence the face of the tubulin molecule that is in contact with the membrane surface—by NR on sparsely tethered BLMs (stBLMs). NR reports on the depth profile of the interfacial components, including the stBLM and any membrane-bound tubulin (Figure 1a). Thus, NR is well suited to determine the spatial extent of the protein in and away from the BLM and yields a potential family of binding surfaces to be investigated by computational methods and amino acid sequence analysis.

For these experiments, an stBLM was composed of a 1:1 molar ratio of DOPC:DOPE. This lipid composition closely mimics the mitochondrial outer membrane, in which the ratio of PC to PE headgroups is about 3:2. The stBLM was bathed in an aqueous 1 mol/L KCl solution buffered at pH 7.4 by 5 mM HEPES. The reflectivity of the stBLM was measured using 4.75 Å neutrons on the NCNR NG7 horizontal reflectometer. To provide contrast between the various components of the stBLM system, a sequence of reflectometry measurements was performed using buffers in 100 % D_2O, 100 % H_2O, and a 2:1 D_2O:H_2O mixture. This procedure was then repeated in the presence of 600 nM tubulin dimers (a physiologically relevant concentration).

The reflectivity data (Figure 1b) were then fit to an stBLM model (Figure 2a). Because it accounts for known molecular volumes, molecular connectivity, and stoichiometric constraints, the model is highly constrained. To determine the orientation of the tubulin dimer on the lipid substrate, the expected scattering profile was calculated for various Euler rotations of the known X-ray crystal structure of tubulin. Due to the elongated geometry of the tubulin dimer, the NR profile is very sensitive to the tilt angle β (Figure 2b), allowing a precise determination of this tilt angle, ≈ 60°, from the optimization of the experimental NR data to the stBLM/tubulin model.

To complement the NR results, molecular dynamics simulations were performed to confirm the orientation of α-tubulin on a DOPE membrane. A range of possible orientations were evaluated using a coarse-grained model of the protein; likely orientations were then optimized using atomistic simulations. The tilt angle of the tubulin on the membrane surface is consistent with that observed by NR, while the atomistic nature of the simulations allows us to identify the particular domain of the tubulin protein that is responsible for binding to the membrane surface. A comparison of the MD and NR results is shown in Figure 2b.

The binding sequence is shown in green in Figure 2b. Notably, it is on the α-tubulin subunit, rather than on the β-tubulin subunit which is conventionally targeted by chemotherapeutics. When associated with the membrane, this amino acid sequence likely adopts an α-helical structure which has opposing hydrophobic and hydrophilic faces, i.e. an amphipathic helix. Such helices are oriented at the interface between the polar lipid headgroups and the hydrophobic lipid tails. We have also shown [5] that the affinity of this helix to the mixed PC/PE membranes considered here depends strongly on the amount of PE lipid. This suggests that the lipid composition of the mitochondrial outer membrane could regulate tubulin binding, which in turn modulates VDAC permeability and consequently mitochondrial function. We hypothesize that this selectivity for the uncharged PE lipids may have developed to overcome electrostatic repulsion between the negatively charged components of the mitochondrial outer membrane and the tubulin molecule.

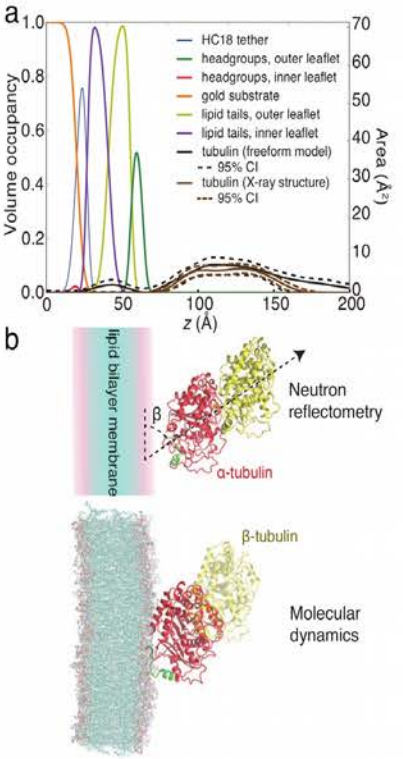

FIGURE 2: Results of modeling the tubulin-stBLM system. (a) Volume occupancy representation showing the position of various chemical species. (b) Visual representation of the structure of membrane-bound tubulin as determined by NR (top) and atomistic molecular dynamics simulations of the α-tubulin subunit (bottom). The Euler angle β is ≈ 60°. The α-tubulin subunit is shown in red; the β-tubulin subunit in yellow; and the binding site in green.

References

[1] M. S. Almen, K. J. Nordstrom, R. Fredriksson, and H. B. Schioth, BMC Biology **7**, 50 (2009).
[2] M. A. Yildirim, K.-I. Goh, M. E. Cusick, A.-L. Barabasi, and M. Vidal, Nat. Biotechnol. **25**, 1119 (2007).
[3] T. K. Rostovtseva, K. L. Sheldon, E. Hassanzadeh, C. Monge, V. Saks, S. M. Bezrukov, and D. L. Sackett, Proc. Natl. Acad. Sci. **105**, 18746 (2008).
[4] J. J. Field, A. B. Waight, and P. D. Senter, Proc. Natl. Acad. Sci. **111**, 13684 (2014).
[5] D. P. Hoogerheide, S. Y. Noskov, D. Jacobs, L. Bergdoll, V. Silin, D. Worcester, J. Abramson, H. Nanda, T. K. Rostovtseva, and S. M. Bezrukov, Nat. Struct. Mol. Biol., submitted (2016).
[6] T. K. Rostovtseva, P. A. Gurnev, M. Y. Chen, and S. M. Bezrukov, J. Biol. Chem. **287**, 29589 (2012).

How Do Lipid Membranes Accommodate Voltage-sensing Domains of Ion Channels?

M. Mihailescu[1], D. Krepkiy[2], J.A. Freites[1,4], E. Schow[4], D.L. Worcester [5,1,3], K. Gawrisch[6], D. Tobias[4], S.H. White[1] and K.J. Swartz[2]

Electrical signals in the nervous system propagate between neurons along axons via electric potentials that are generated by proteins that reside within the cell membranes. Known as voltage-gated ion channels, these proteins allow ions to pass through the cell membrane in a controlled manner. In the voltage-gated potassium, sodium, and calcium channels found in neurons and muscle cells, a special part of the protein, called the voltage-sensing domain (VSD), moves inside the membrane in response to changes in the membrane potential and drives the ion conduction pore open or closed (gating) [1] (Fig. 1). Until a few years ago, it was thought that VSDs were unique to voltage-gated ion channels. This view has changed radically with the discovery of new families of proteins that use VSD constructs for purposes other than ion channel gating [2]. There is tremendous interest in the structure and function of such proteins. Researchers want to elucidate the mechanism of ion gating in ion channels. Moreover, the portability of VSDs across the genomes of different organisms can provide important clues about evolutionary pathways.

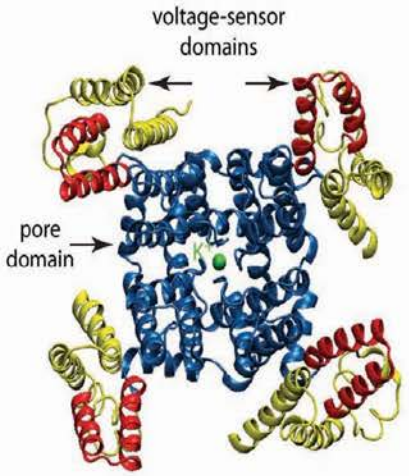

FIGURE 1: Top view (from above the surface of a lipid membrane) of a voltage-gated potassium channel.

Crystallographic studies using x-ray diffraction on voltage-gated potassium channels have revealed the atomic structure of the VSD in crystallized channels and identified regions that move in response to changes in the membrane electric field [3,4]. However, none of those studies were able to demonstrate the structure and conformation of the voltage-sensor domain in its native lipid environment. A picture of the topology of the VSD in a lipid membrane was needed in order to understand the role of the lipid in the protein stability and function, and ultimately, in the voltage-gating mechanism. We have developed an approach that employs neutron diffraction to obtain the image of functional voltage sensor domains in lipid membranes.

We focused our efforts on the voltage-sensing domain of KvAP, an archaebacterial channel from *Aeropyrum pernix* [5], because this domain can be robustly expressed, stably purified, and reconstituted into lipid membranes. The voltage-sensing domains were expressed in *E. coli*, purified, and transferred to lipid vesicles (reconstitution of the VSDs into proteoliposomes). Lipid multilayer samples were prepared by deposition of aqueous dispersions of proteoliposomes on cover glass slides. They were allowed to dry and rehydrated from water phase at 93 % relative humidity throughout the diffraction experiments. Samples containing a few thousands lipid bilayers with incorporated VSDs were measured and strong lamellar diffraction patterns were observed (Fig. 2) and used to generate one dimensional, absolute-scale, scattering-length density profiles normal to the plane of the lipid bilayer. We have determined the protein distribution using contrast variation between protonated and deuterated VSDs. The voltage-sensing domain of KvAP was uniformly deuterated to 74 % and multilayers were formed with either protonated or deuterated protein at the same protein:lipid ratio and lipid composition. Fourier transformation of the diffraction data to obtain scattering length density profiles and subtraction of the individual profiles for the labeled and unlabeled protein reveals the distribution of the protein across the bilayer (Fig. 3a; red).

[1]University of California, Irvine, Irvine, CA 92697
[2]National Institute of Neurological Disorders and Stroke, National Institutes of Health, Bethesda, MD 20892
[3]NIST Center for Neutron Research, National Institute of Standards and Technology, Gaithersburg, MD 20899
[4]University of California, Irvine, Irvine, CA 92697
[5]University of Missouri, Columbia MO 65211
[6]National Institute of Alcohol Abuse and Alcoholism, National Institutes of Health, Bethesda, MD 20892

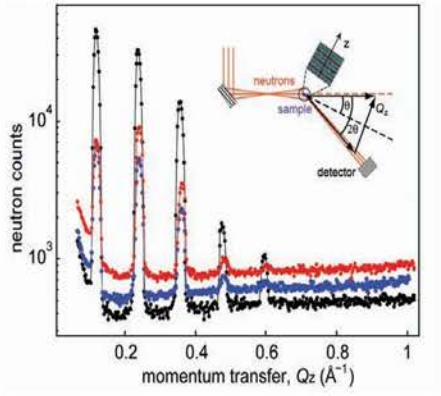

FIGURE 2: Neutron diffraction data collected at the AND/R (NCNR) for lipid multilayers samples with incorporated VSDs: Data displayed are for neat lipid (black), unlabeled VSD in lipid (blue) and deuterated VSD in lipid (red). The inset is a schematic illustration of the experimental setup.

The profile is presented with its uncertainty band derived from the standard deviation of the measured data. Maxima in the density distribution are observed in the headgroup region of the bilayer and minima in the inter-bilayer space. These findings firmly establish that voltage-sensing domains adopt a transmembrane topology, with the four helices oriented roughly normal to the membrane plane. Moreover, the protein distribution (Fig. 3a; red) exhibits extensive overlap with the water distribution (Fig. 3a; blue) within the confines of the lipid membrane, suggesting that the voltage-sensing domains are highly hydrated within the bilayer.

Because neutron diffraction reflects an average distribution of atoms, atomic details in the bilayer structure close to the VSD are not easily revealed in the experiment. To explore details in the protein, lipid and water distribution we employed molecular dynamics simulation for VSDs embedded in lipid bilayers. The simulation results (Fig. 3b) are in qualitative agreement with the experiment regarding the trans-membrane disposition of the four helical segments of the VSD and the overlap with the water distribution. Additionally, the simulations predict that about 4 % all water in the system is intimately associated with the VSDs, and that the lipid layers in contact with the protein are perturbed to a much greater extent than lipids several layers away from the protein (Fig. 3b).

Our results provide direct evidence that voltage sensors domain topology in a membrane environment and will be relevant for other important classes of membrane proteins. They show that the voltage-sensing domains of voltage-gated ion channels interact profoundly with the surrounding membrane and water, in a manner that facilitates their movement and function within the lipid membrane.

References

[1] K. J. Swartz, Nature **456**, 891 (2008).
[2] Murata Y. *et al.*, Nature **435**, 1239 (2005).
[3] Y. Jiang, *et al.*, Nature **423**, 33 (2003).
[4] S. B. Long, *et al.*, Nature **450**, 376 (2007).
[5] V. Ruta, *et al.*, Nature **422**, 180 (2003).

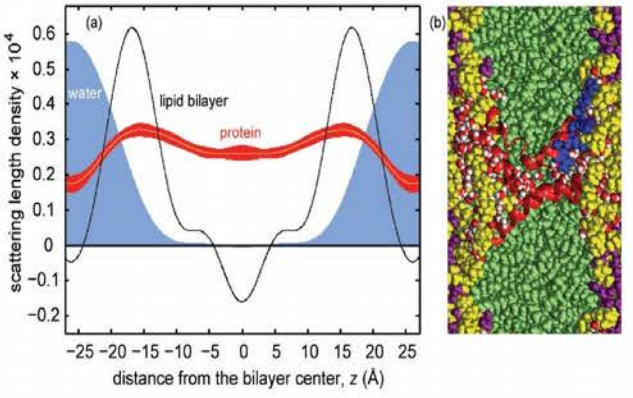

FIGURE 3: Distribution of the protein in lipid membranes: (a) Neutron diffraction results. Trans-bilayer distribution of the protein (red), water (blue) and lipid bilayer (black). (b) Molecular dynamics simulation results. Snapshot of the region in the vicinity of a voltage-sensing domains. Waters within 6 Å of protein are shown as red/white spheres while all other waters are colored purple. Phosphocholine headgroups are colored yellow and the acyl chains are colored light green.

Electrochemistry and Photovoltaics

Although the application of neutron reflectometry to research in this area has not yet become as extensive as in others, it continues to grow steadily. Early work was performed by Dave Wiesler on electrochemical reduction/oxidation reactions while Joe Dura, Steve DeCaluwe and company have focused more recently on fuel cell membranes. Michael Mackay and students from UD have recently investigated the morphology of organic photovoltaic devices at the NCNR, collaborating with staff Brian Kirby, Brian Maranville, and others.

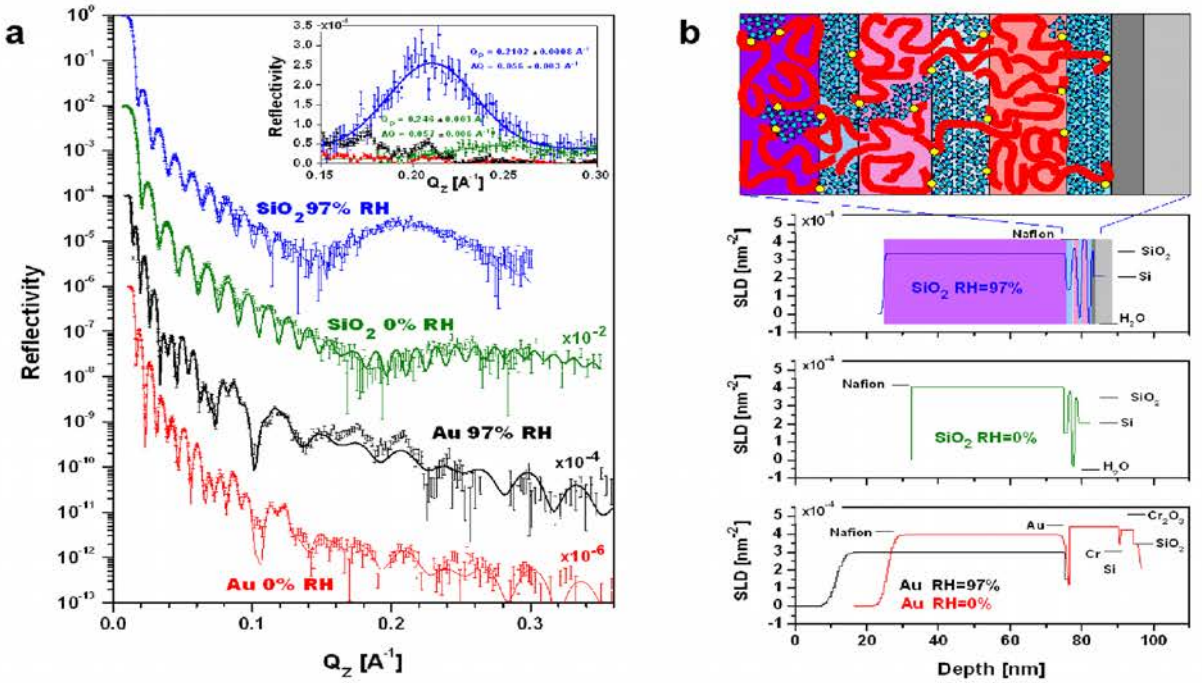


Joseph Dura
A126 x6251

Multilamellar Interface Structures in Nafion,
Joseph A. Dura, Vivek S. Murthi, Michael Hartman, Sushil K. Satija, Charles F. Majkrzak,
Macromolecules, **42** (13), pp 4769–4774 (2009) [DOI: 10.1021/ma802823j].

Nanoparticle distribution in polymer-based solar cells affects solar cell performance: A neutron reflectivity study

Jonathan Kiel[1], Brian Kirby[2], Charles Majkrzak[2],
Brian Maranville[2], Michael Mackay[3]

Thursday, August 20th, 2009

1) Michigan State University, Department of Chemical Engineering and Materials Science
2) National Institute of Standards and Technology, Center for Neutron Research
3) University of Delaware, Materials Science and Engineering

UNIVERSITY OF DELAWARE MICHIGAN STATE UNIVERSITY NIST Center for Neutron Research

Components of organic solar cells

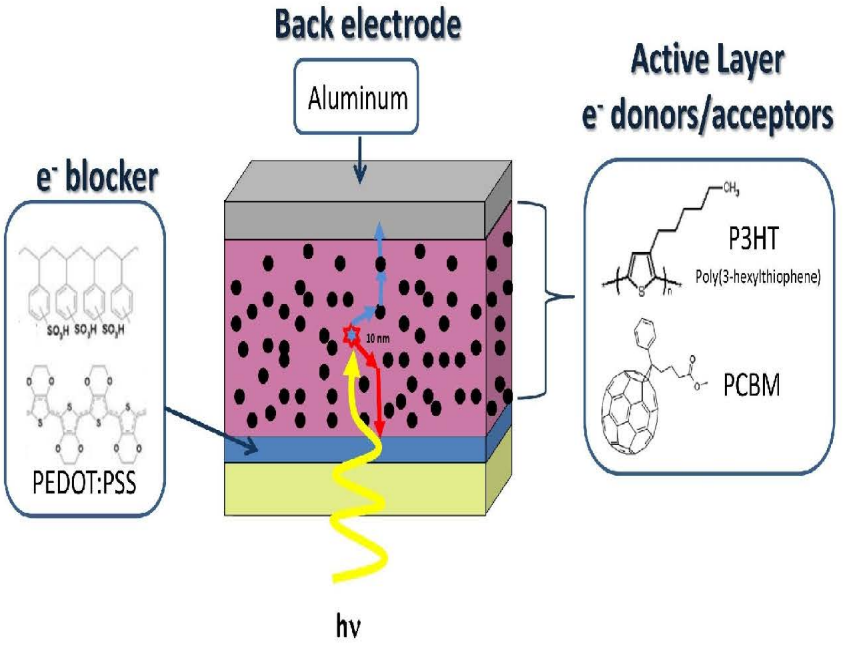

- Exciton diffusion length ~10 nm
- PCBM:P3HT morphology very important

What is the morphology of the active layer

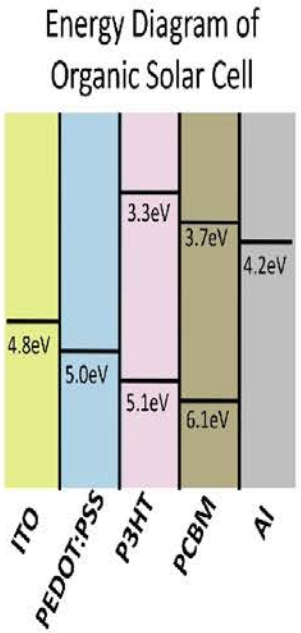

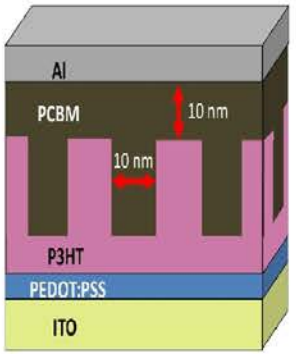

Idealized morphology

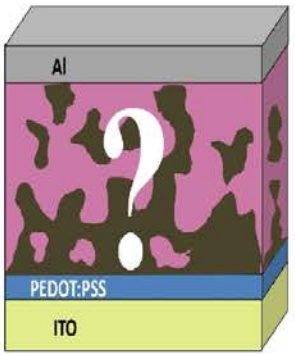

Actual morphology

K. M. Coakley, M. D. McGehee, *Chemical Materials*, **2004**

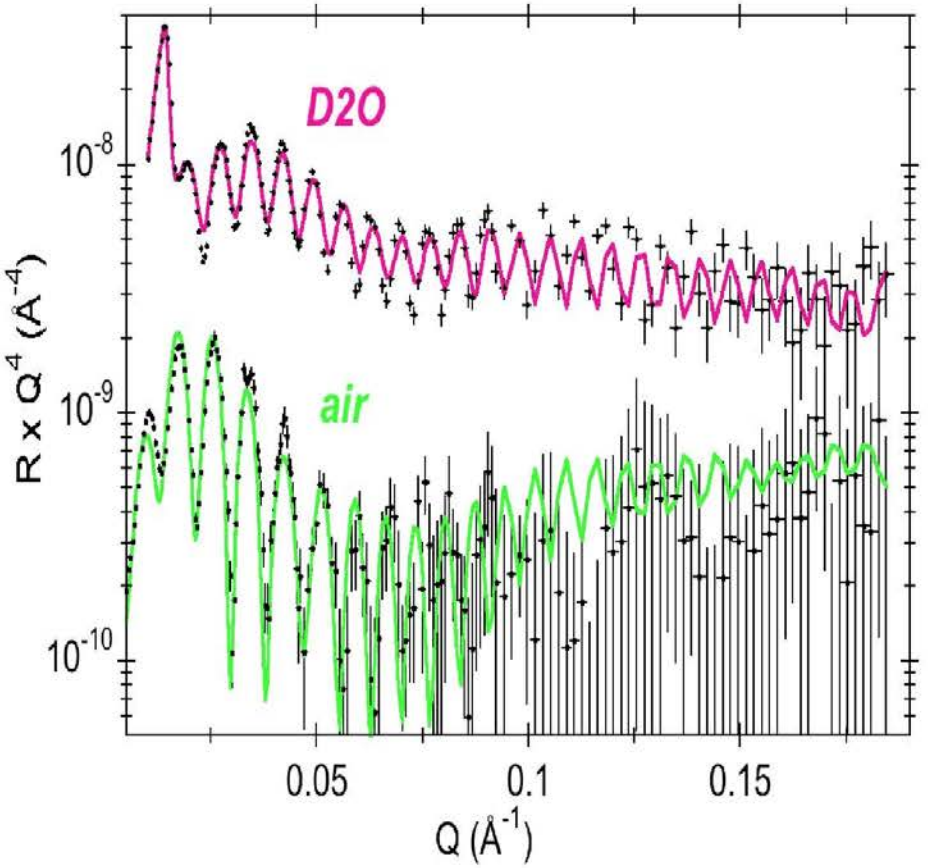

Reflectivity data collected from the same film system with two different backing media -- air and deuterated water. Once again, the reason for collecting such composite system (reference plus unkown part) reflectivity data is to be able to retrieve the phase information.

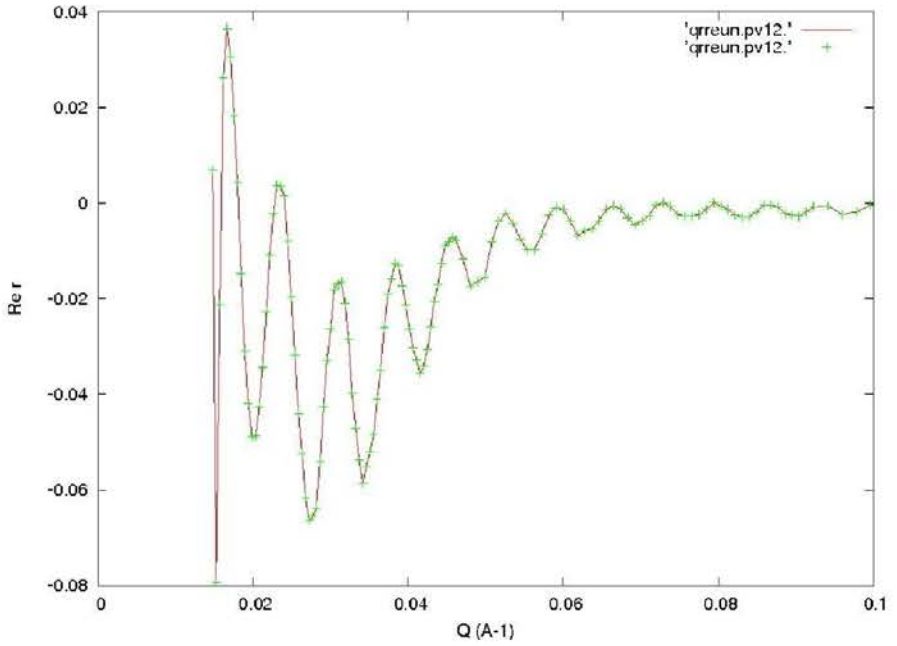

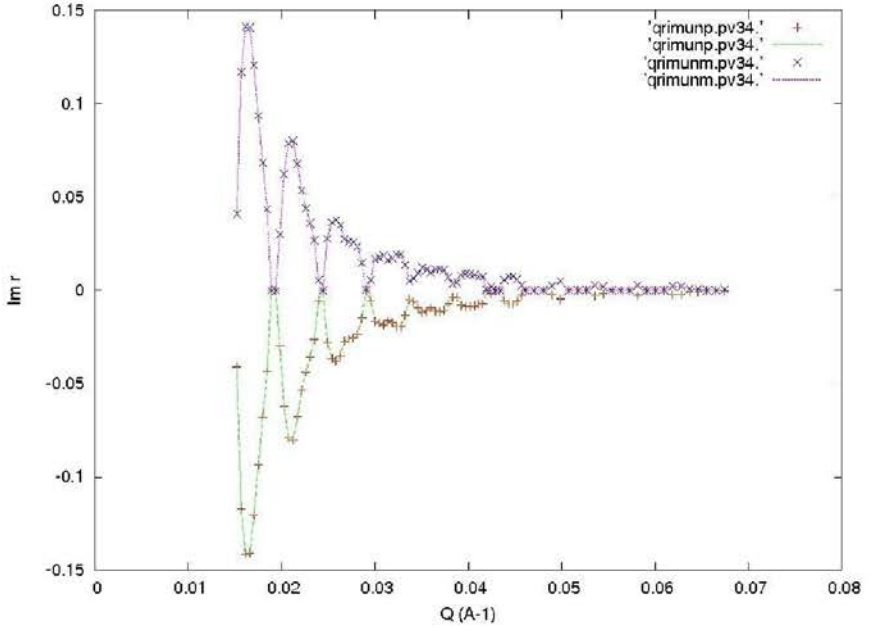

Real and imaginary parts of the reflection amplitude associated with the film structure alone -- as obtained from analysis of the composite system reflectivity data sets shown in the previous slide.

PCBM Volume % Comparison

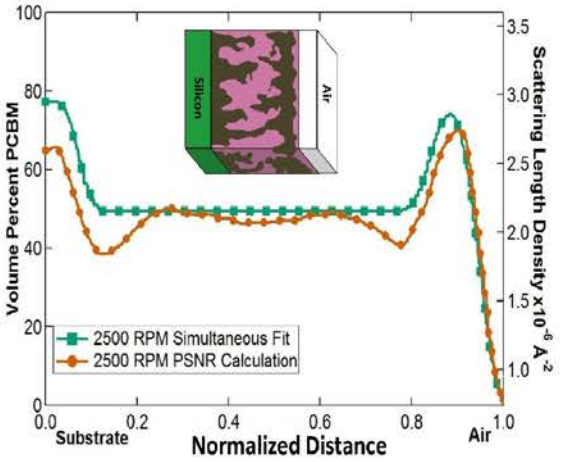

$$\text{Vol\% PCBM} = \frac{SLD_{measured} - SLD_{P3HT}}{SLD_{PCBM} - SLD_{P3HT}}$$

- Simultaneous fitting and PSNR calculations show great agreement
- High PCBM concentration at substrate
- High PCBM concentration near air interface

Development of scattering theory for analysis of neutron reflectivity measurements

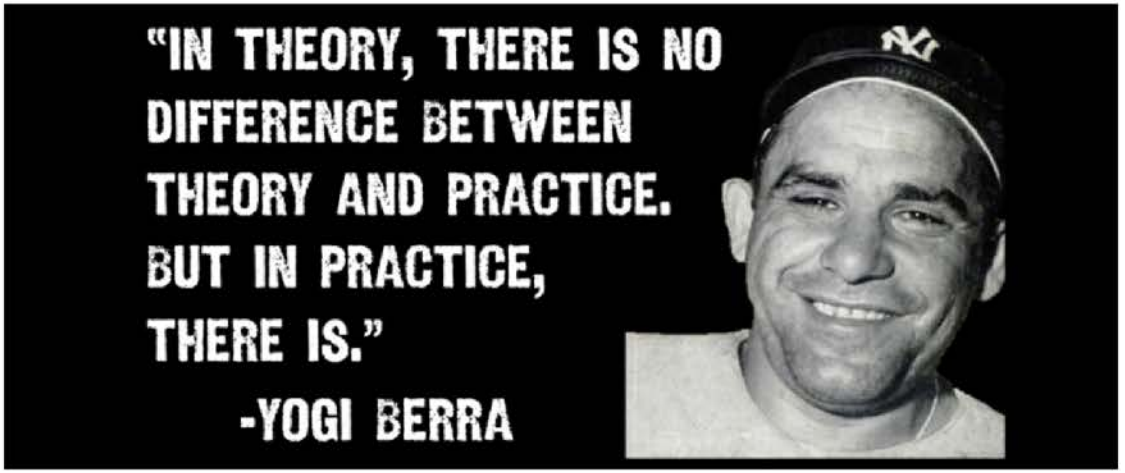

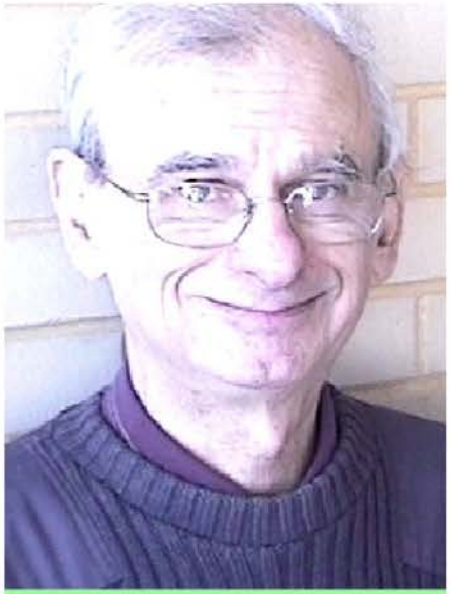
Norman Berk*

Fortunately, the NCNR has a resident theoretical physicist who is a very well-respected expert in neutron scattering – and who has been "instrumental" in helping formulate our methodologies for interpreting reflectivity measurements. Significant contributions to our reflectometry analysis tools have also been made over the years by John Ankner, Paul Kienzle, and Brian Maranville. In-house experts in computer science, like Przemek Klosowski, have provided consistent support for numerical computations at the NCNR.

PBS

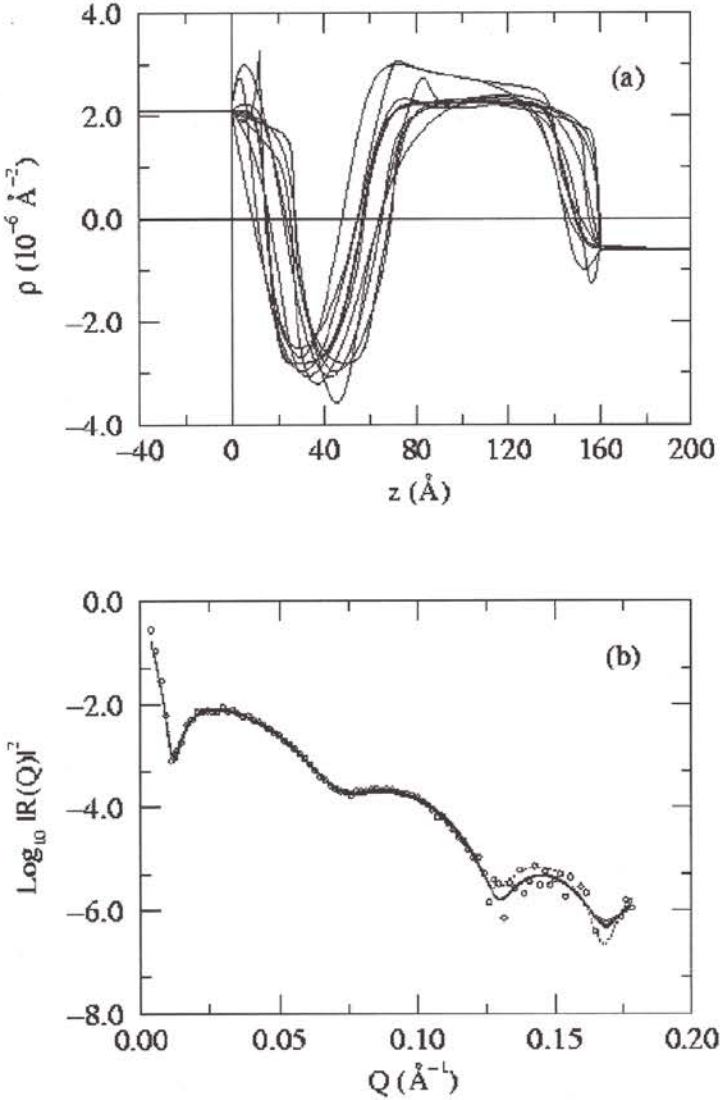

Repeated fits of reflectivity data from a Ti/TiO film system on a Si substrate in contact with an aqueous reservoir (Berk et al.). The variation among the individual fits is indicative of the accuracy attainable in the SLD profile given the truncation of the reflectivity data at a maximum value of Q and the statistical uncertainty in the data points.

PBS

TiO in situ: Wiesler, et al.

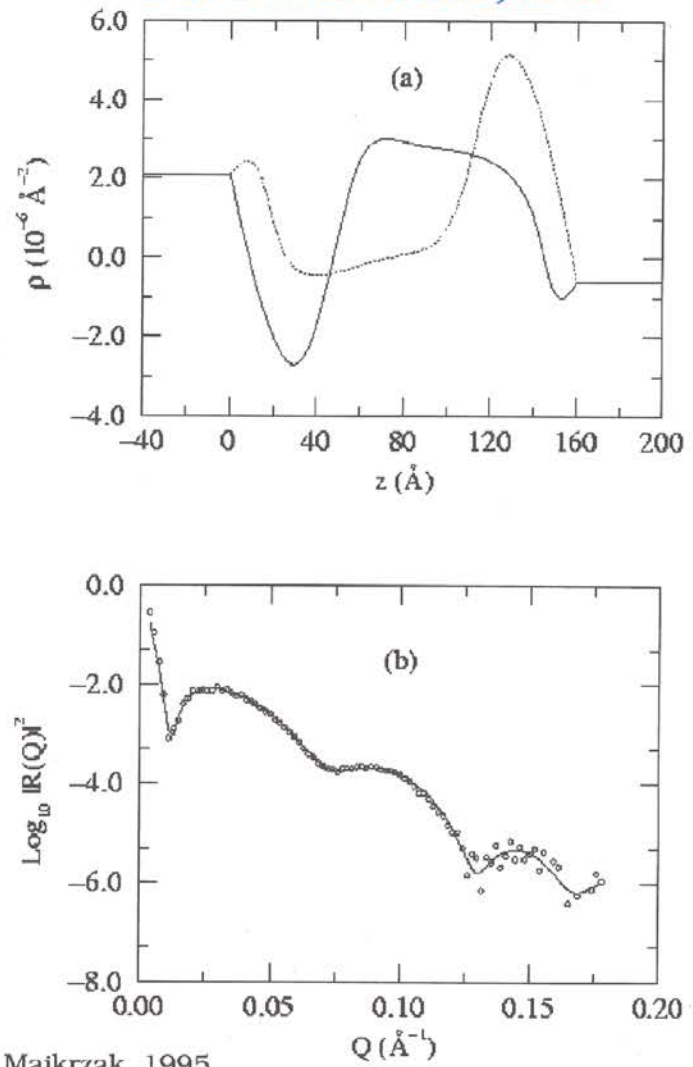

Berk & Majkrzak, 1995

It was found that if enough individual fits were performed, another "family" of fits emerged (only one of which is shown above in comparison to a representative fit of the other family shown on the previous slide) with essentially the same chi-squared goodness of fit criteria -- this alternative SLD profile is a consequence of the loss of phase information inherent when the reflectivity $|r|^2$ (proportional to the reflected *intensity*) is measured rather than the complex reflection *amplitude* r -- i.e., the non uniqueness arises from a loss of the phase information carried by the reflected wave function.

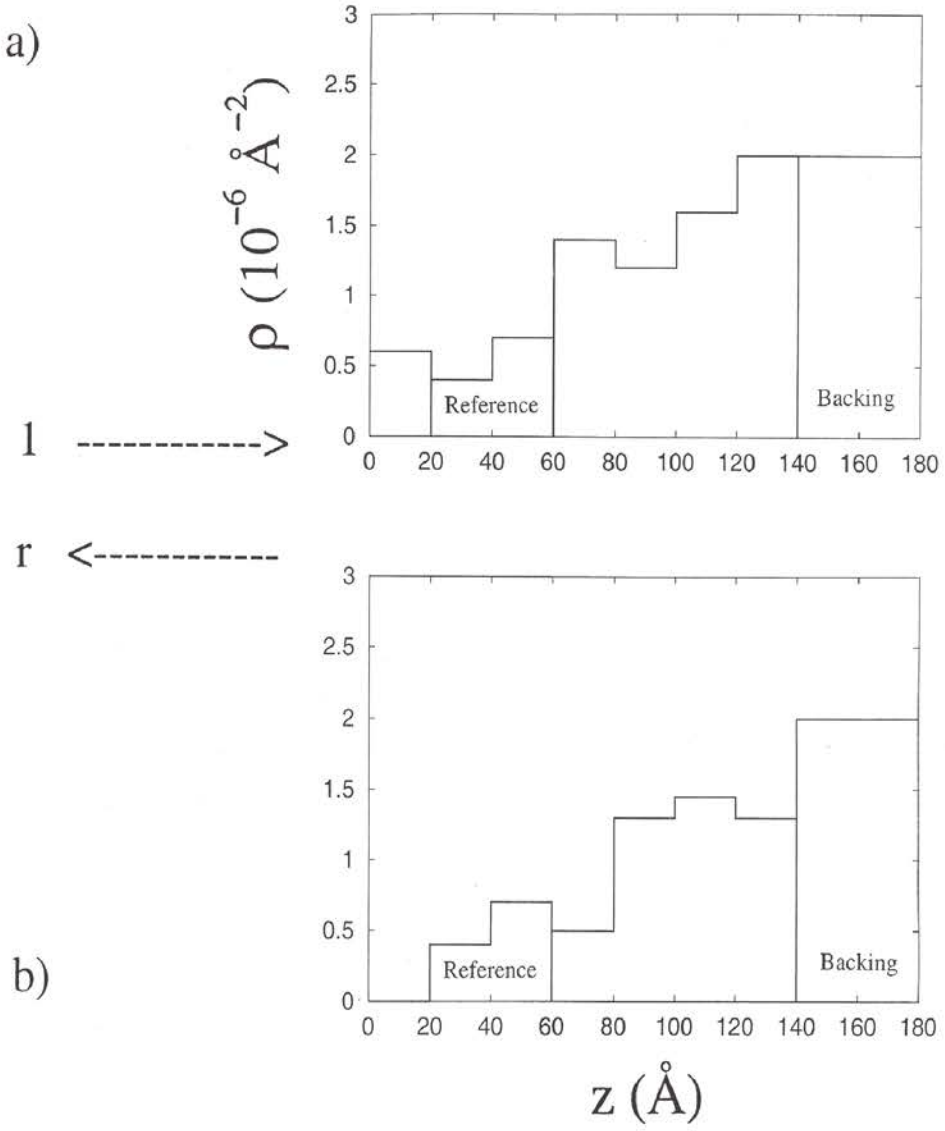

Figure 9.

Figure 10.

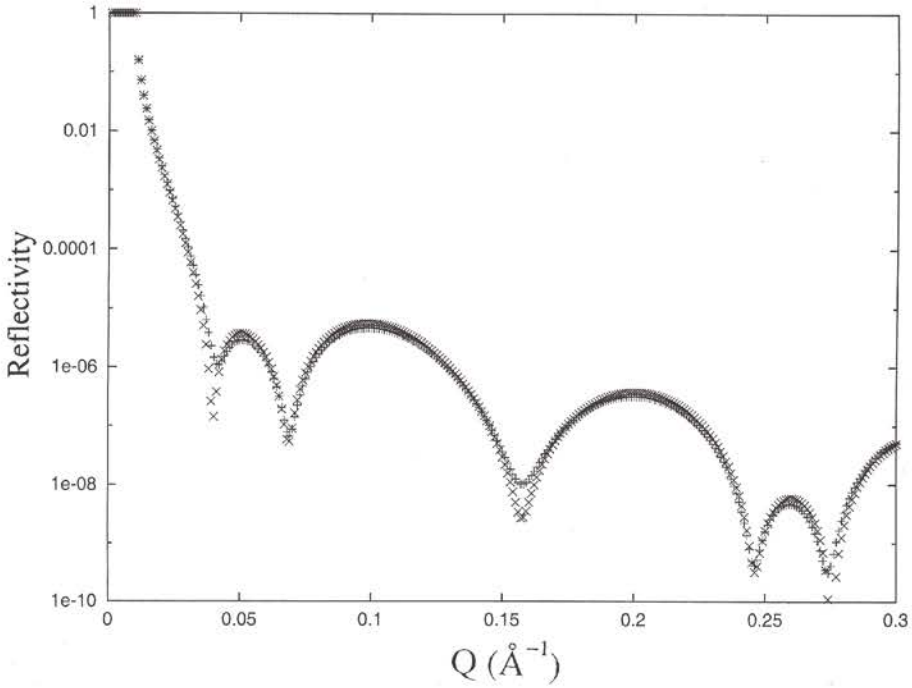

Figure 11.

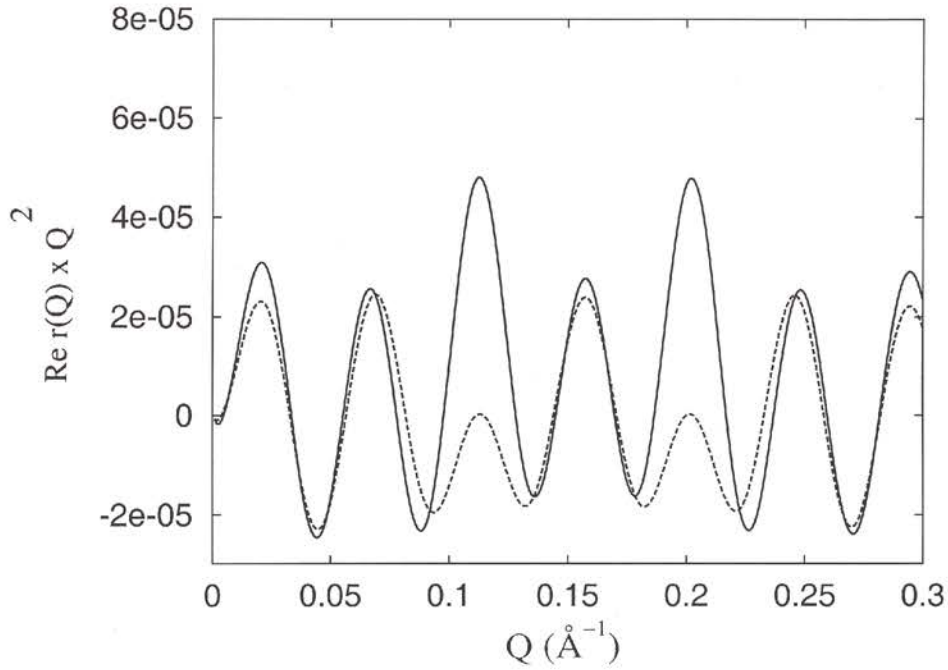

Inverting reflectivity

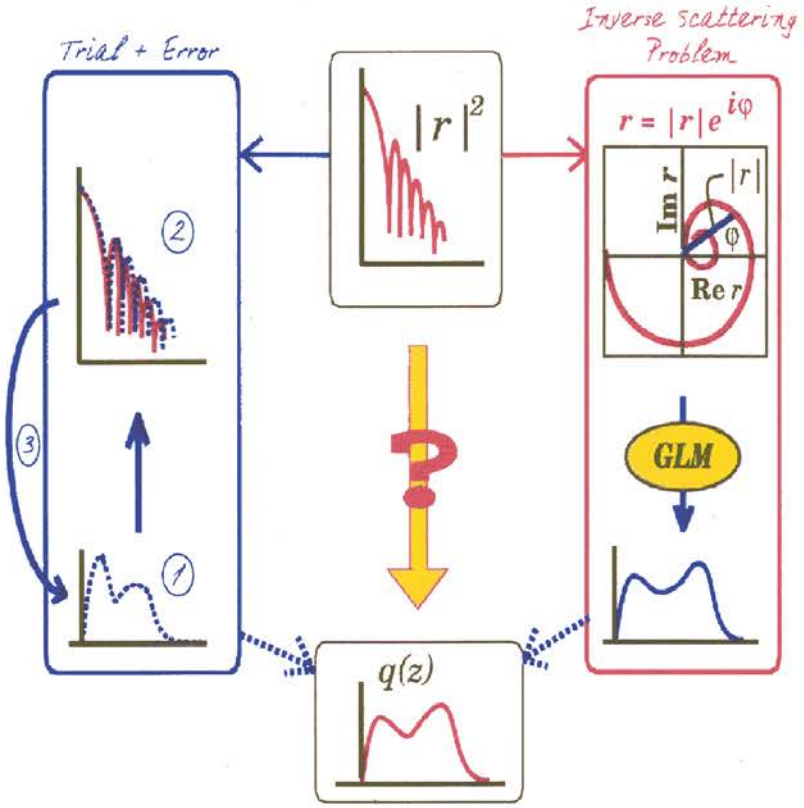

(after N.F. Berk)

Theoretically, Norm and several others, including Paul Sacks, Lipperheide, and Leeb, realized, that the one-dimensional specular reflectivity could be directly inverted **if** the reflected wave *amplitude* and not just the intensity as measured was known.

FOURIER TRANSFORM OF THE COMPLEX REFLECTION AMPLITUDE

$$\mathcal{R}(z) = \frac{1}{\pi} \mathrm{Re} \int_0^\infty r(k_z) e^{ik_z z} dk_z$$

GEL'FAND LEVITAN MARCHENKO INTEGRAL EQUATION

$$K(z,y) + \mathcal{R}(z+y) + \int_{-z}^{+z} K(z,x)\mathcal{R}(x+y)dx = 0$$

SCATTERING LENGTH DENSITY

$$\rho(z) = 2\frac{dK(z,z)}{dz}$$

GIVEN THE COMPLEX REFLECTION AMPLITUDE, THE SCATTERING LENGTH DENSITY ρ CAN BE OBTAINED FROM AN EXACT, FIRST PRINCIPLE INVERSION FOR A REAL POTENTIAL OF FINITE EXTENT — AND THE SOLUTION IS UNIQUE!

NO FITTING, NO ADJUSTABLE PARAMETERS

But how do you determine the reflection amplitude as a function of Q from measured reflected intensity? Thinking about the piece-wise continuous solution method of the Shroedinger wave equation provided the answer . . .

FORMALISM ALLOWS A COMPOSITE POTENTIAL TO BE EXPRESSED AS A PRODUCT:

$$\begin{pmatrix} A & B \\ C & D \end{pmatrix} = \begin{pmatrix} a & b \\ c & d \end{pmatrix} \begin{pmatrix} w & x \\ y & z \end{pmatrix}$$

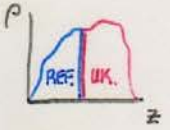

COMPOSITE (1,2,3) UNKNOWN REFERENCE (1,2,3)

$$|R(Q)|^2 = |R_1(Q)|^2,\ |R_2(Q)|^2,\ \text{and}\ |R_3(Q)|^2$$

$$\Sigma_i \equiv 2\left[\frac{1+|R_i|^2}{1-|R_i|^2}\right] = A_i^2 + B_i^2 + C_i^2 + D_i^2$$

$$A_i^2 = a^2 w_i^2 + b^2 y_i^2 + 2ab w_i y_i$$

$$C_i^2 = c^2 w_i^2 + d^2 y_i^2 + 2cd w_i y_i$$

$$B_i^2 = a^2 x_i^2 + b^2 z_i^2 + 2ab x_i z_i$$

$$D_i^2 = c^2 x_i^2 + d^2 z_i^2 + 2cd x_i z_i$$

(INDEPENDENTLY AT EACH Q)

$$\Sigma_i = \overbrace{(w_i^2 + x_i^2)}^{\text{REF.}}\alpha + \overbrace{(y_i^2 + z_i^2)}^{\text{REF.}}\beta + \overbrace{2(w_i y_i + x_i z_i)}^{\text{REF.}}\gamma$$

SOLVE FOR UNKNOWNS $\alpha, \beta,$ AND γ TO GET

$i = 1, 2, 3$

$\alpha = a^2 + c^2$

$\beta = b^2 + d^2$

$\gamma = ab + cd$

$$R_{\text{UNKNOWN}} = \frac{(\beta - \alpha) - 2i\gamma}{2 + \beta + \alpha}$$

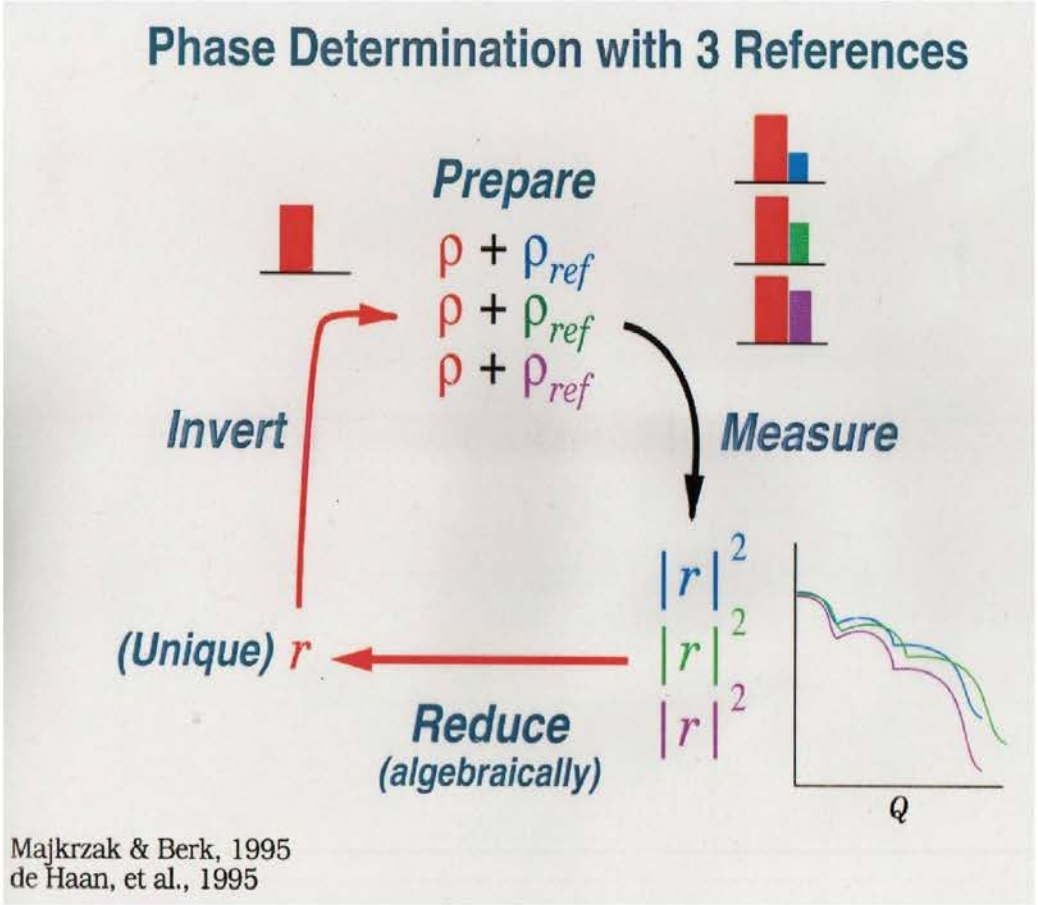

Phase determination

C.F. Majkrzak and N.F. Berk, Phys. Rev. B **52**, 10827 (1995).
V.–O. de Haan, et al., Phys. Rev. B **52**, 10830 (1995).

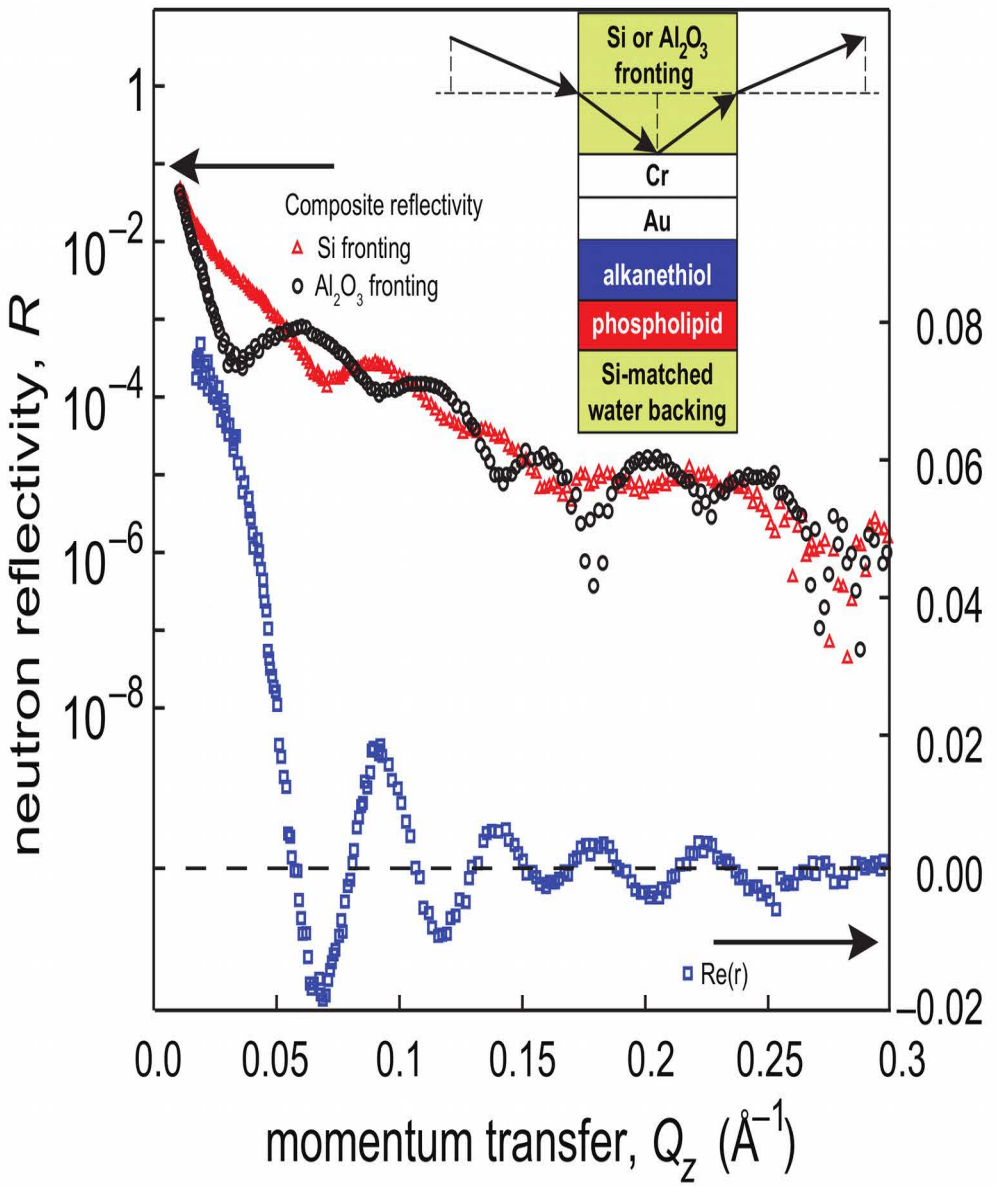
Si or Al2O3 fronting
Cr
Au
alkanethiol
phospholipid
Si-matched water backing
Composite reflectivity
Si fronting
Al2O3 fronting
Re(r)
neutron reflectivity, R
momentum transfer, Qz (Å−1)
1
10−2
10−4
10−6
10−8
0.08
0.06
0.04
0.02
0.00
−0.02
0.0
0.05
0.1
0.15
0.2
0.25
0.3

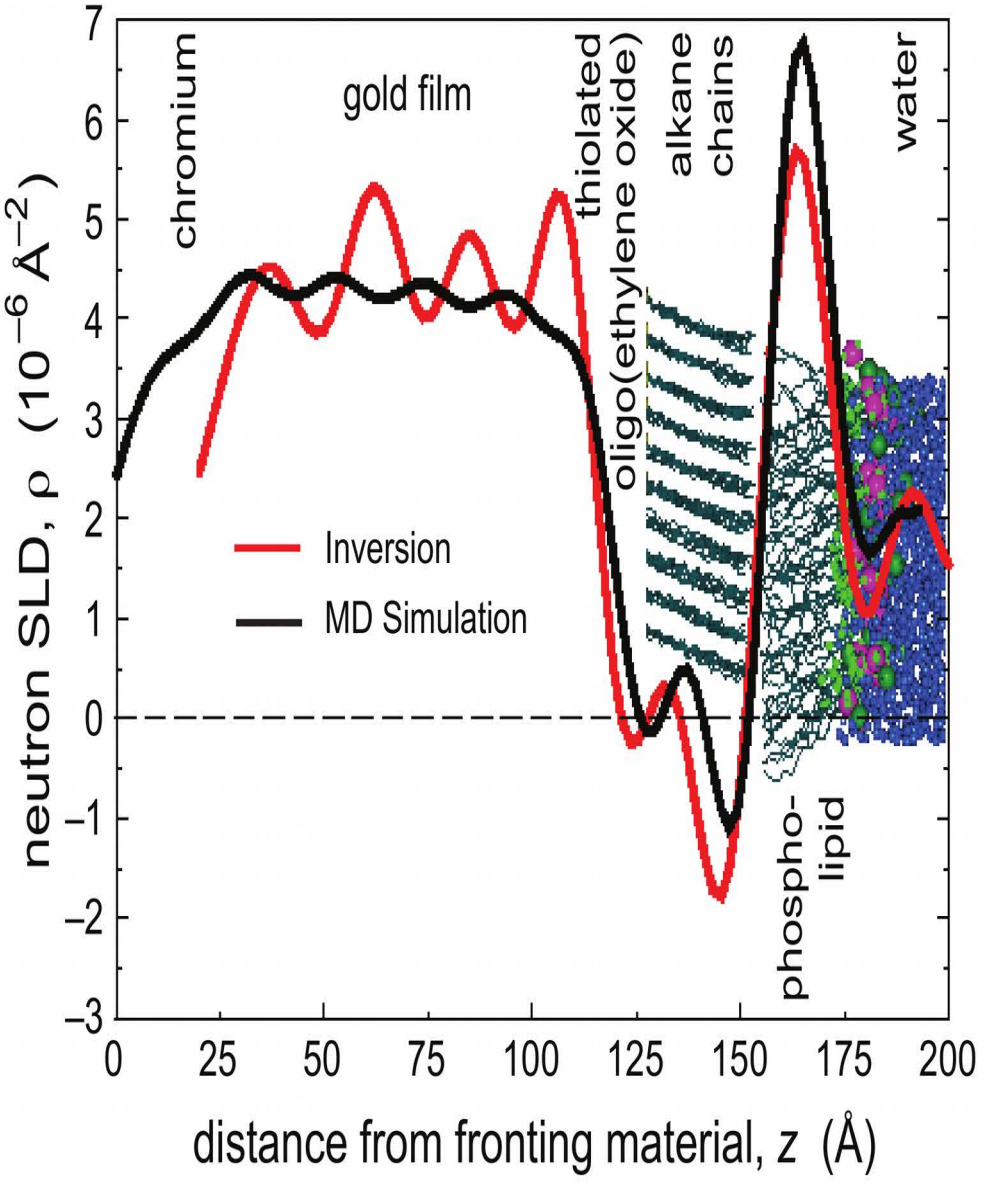
chromium
gold film
thiolated oligo(ethylene oxide)
alkane chains
water
phospho-lipid
Inversion
MD Simulation
neutron SLD, ρ (10−6 Å−2)
distance from fronting material, z (Å)
7
6
5
4
3
2
1
0
−1
−2
−3
0
25
50
75
100
125
150
175
200

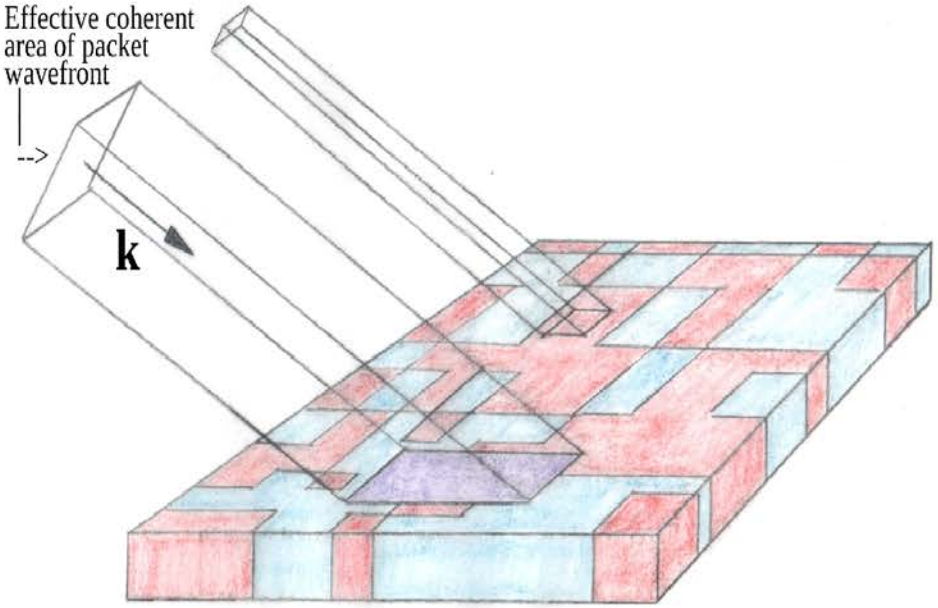

The effective transverse coherence area perpendicular to the propagation direction of the neutron wave packet is projected onto the film surface defining an area over which in-plane variations in SLD are averaged over in the specular process (note that the glancing angle of incidence enhances the projection along one in-plane direction):

$$r = (4\pi / (iQ)) \int_{-\infty}^{+\infty} \psi_{kz}(z) \langle \rho(x,y,z) \rangle_{x,y} e^{ikz} dz$$

$$\langle \rho(x,y,z) \rangle_{x,y} = (1/A) \iint_{-\infty}^{+\infty} \rho(x,y,z)\, dxdy$$

The length scale of the SLD variations must be small enough for effective averaging to occur within the projected area. (The purple shaded area is meant to represent the coherent average of separate areas of "red" and "blue" SLD.) If not, then the net measured reflected intensity $|r|^2$ is an area-weighted sum of reflectivities, each corresponding to an in-plane averaged SLD within a particular respective area, as depicted schematically in the figure above for the case of two distinct areas of different SLD (red and blue areas):

$$|r_{\text{NET MEASURED}}|^2 = (A_{\text{RED}} / A_{\text{TOTAL}})|r_{\text{RED}}|^2 + (A_{\text{BLUE}} / A_{\text{TOTAL}})|r_{\text{BLUE}}|^2$$

PHYSICAL REVIEW A **89**, 033851 (2014)

Determination of the effective transverse coherence of the neutron wave packet as employed in reflectivity investigations of condensed-matter structures. I. Measurements

Charles F. Majkrzak,* Christopher Metting, Brian B. Maranville, Joseph A. Dura, Sushil Satija, Terrence Udovic, and Norman F. Berk

Center for Neutron Research, National Institute of Standards and Technology Gaithersburg, Maryland 20899, USA

(Received 6 September 2013; revised manuscript received 22 November 2013; published 27 March 2014)

The primary purpose of this investigation is to determine the effective coherent extent of the neutron wave packet transverse to its mean propagation vector k when it is prepared in a typical instrument used to study the structure of materials in thin film form via specular reflection. There are two principal reasons for doing so. One has to do with the fundamental physical interest in the characteristics of a free neutron as a quantum object, while the other is of a more practical nature, relating to the understanding of how to interpret elastic scattering data when the neutron is employed as a probe of condensed-matter structure on an atomic or nanometer scale. Knowing such a basic physical characteristic as the neutron's effective transverse coherence can dictate how to properly analyze specular reflectivity data obtained for material film structures possessing some amount of in-plane inhomogeneity. In this study we describe a means of measuring the effective transverse coherence length of the neutron wave packet by specular reflection from a series of diffraction gratings of different spacings. Complementary nonspecular measurements of the widths of grating reflections were also performed, which corroborate the specular results. (This paper principally describes measurements interpreted according to the theoretical picture presented in a companion paper.) Each grating was fabricated by lift-off photolithography patterning of a nickel film (approximately 1000 Å thick) formed by physical vapor deposition on a flat silicon crystal surface. The grating periods ranged from 10 μm (5 μm Ni stripe, 5 μm intervening space) to several hundred microns. The transverse coherence length, modeled as the width of the wave packet, was determined from an analysis of the specular reflectivity curves of the set of gratings.

DOI: 10.1103/PhysRevA.89.033851 PACS number(s): 42.25.Kb, 37.20.+j, 03.75.Dg, 61.05.fj

Figure 13

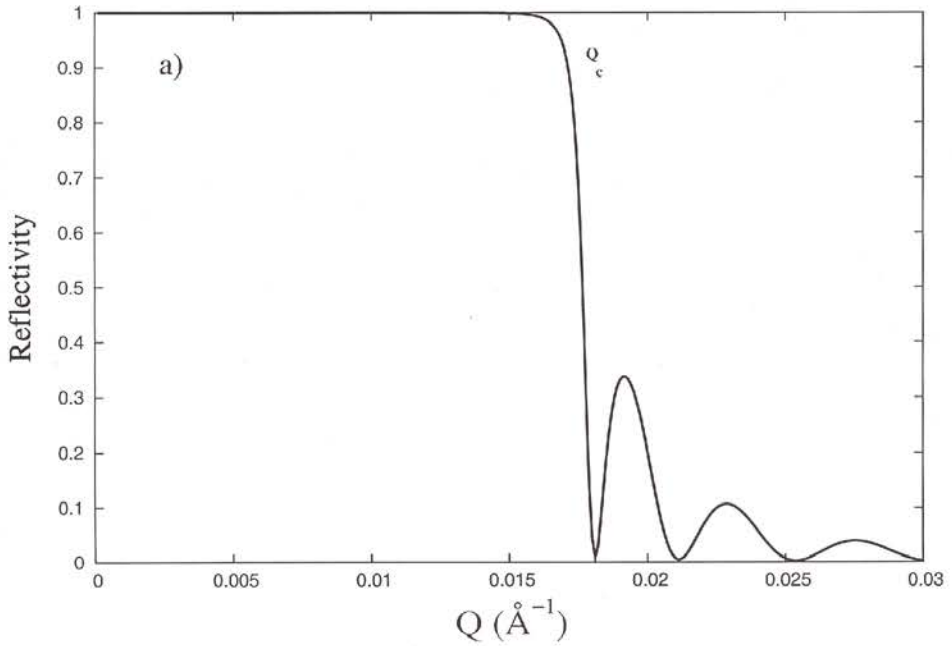

Coherent Average

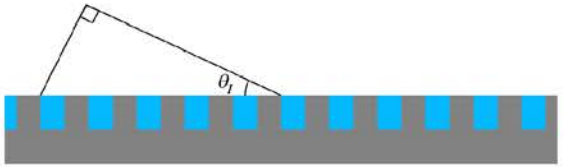

Figure 13

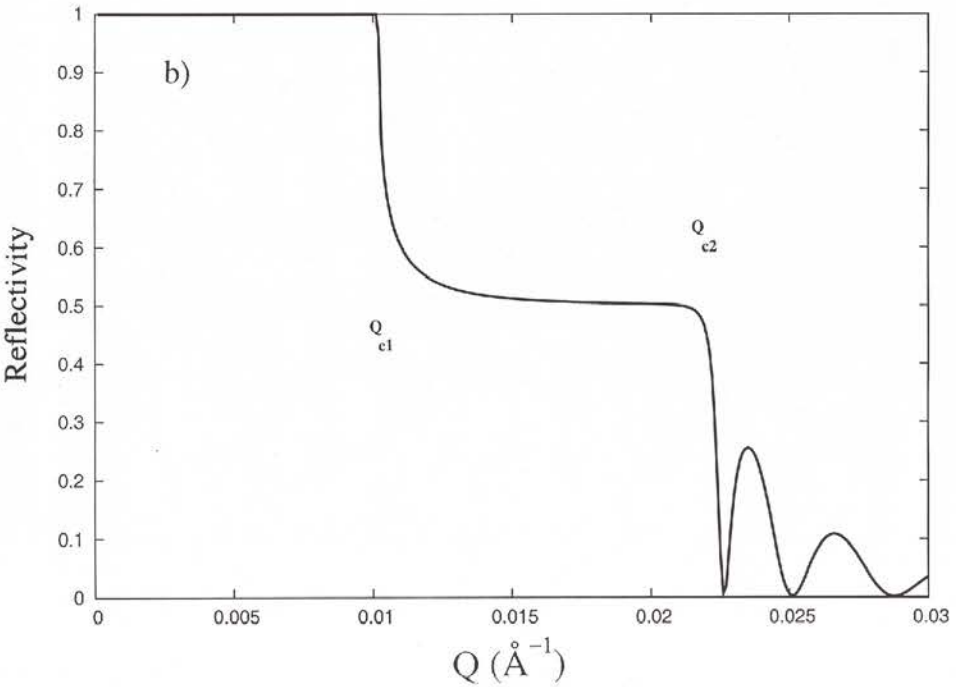

Incoherent Sum

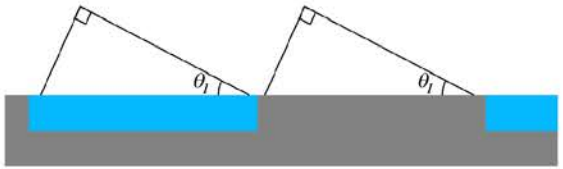

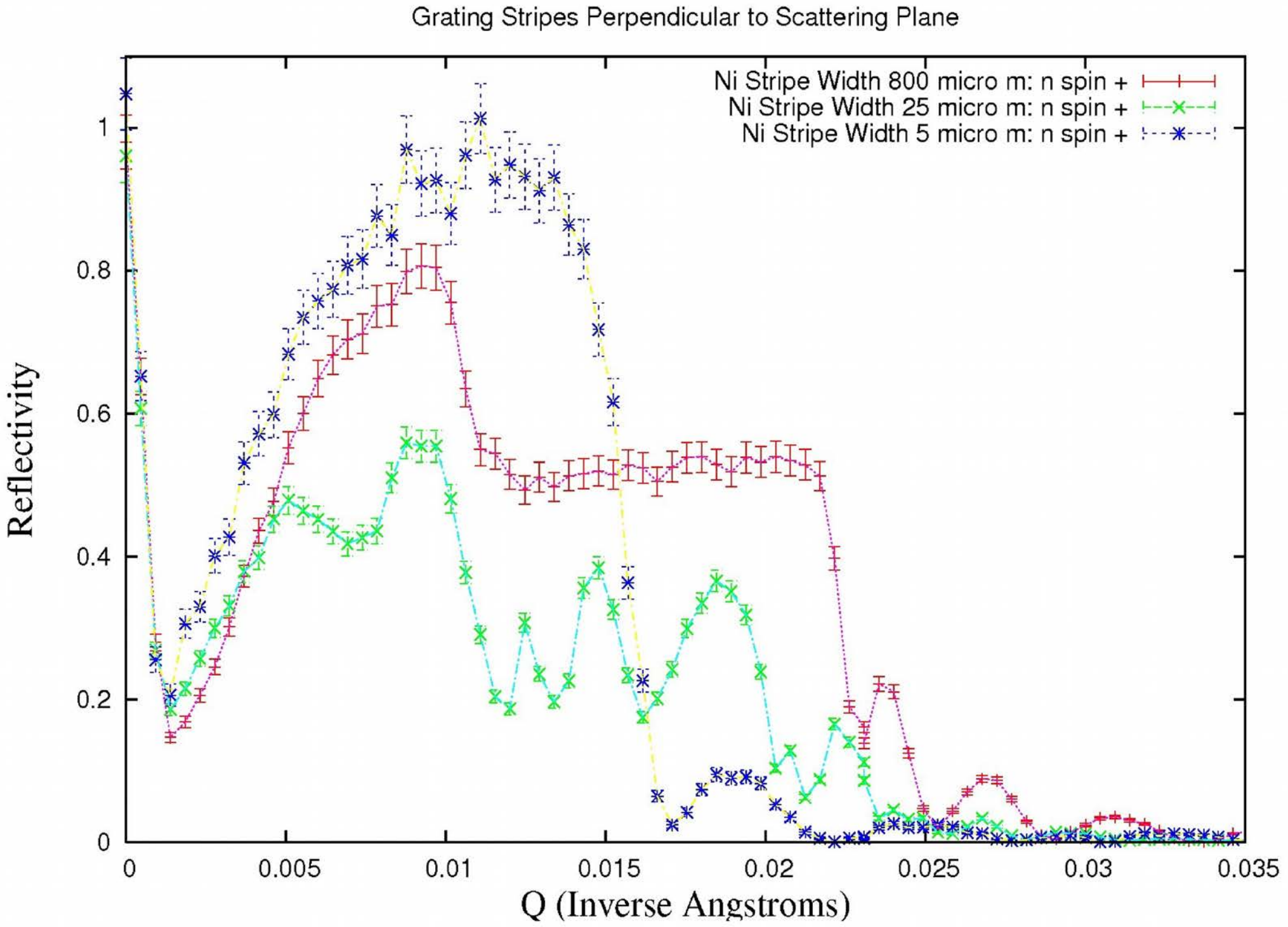
Grating Stripes Perpendicular to Scattering Plane
Ni Stripe Width 800 micro m: n spin +
Ni Stripe Width 25 micro m: n spin +
Ni Stripe Width 5 micro m: n spin +
Reflectivity
Q (Inverse Angstroms)
0
0.2
0.4
0.6
0.8
1
0
0.005
0.01
0.015
0.02
0.025
0.03
0.035

ORIGIN OF THE 2ND LENGTH SCALE ABOVE THE MAGNETIC-SPIRAL PHASE OF TB
GEHRING, PM; HIROTA, K; MAJKRZAK, CF; SHIRANE, G
PHYSICAL REVIEW LETTERS Volume: 71 Issue: 7 Pages: 1087-1090 Published: AUG 16 1993

SPATIALLY MODULATED ANTIFERROMAGNETIC ORDER IN COO/NIO SUPERLATTICES
BORCHERS, JA; CAREY, MJ; ERWIN, RW; MAJKRZAK, CF; BERKOWITZ, AE
PHYSICAL REVIEW LETTERS Volume: 70 Issue: 12 Pages: 1878-1881 Published: MAR 22 1993

Reversible tuning of the magnetic exchange coupling in Fe/V (001) superlattices using hydrogen
Hjorvarsson, B; Dura, JA; Isberg, P; Watanabe, T; Udovic, TJ; Andersson, G; Majkrzak, CF
PHYSICAL REVIEW LETTERS Volume: 79 Issue: 5 Pages: 901-904 Published: AUG 4 1997

Asymmetric magnetization reversal in exchange-biased hysteresis loops
Fitzsimmons, MR; Yashar, P; Leighton, C; Schuller, IK; Nogues, J; Majkrzak, CF; Dura, JA
PHYSICAL REVIEW LETTERS Volume: 84 Issue: 17 Pages: 3986-3989 Published: APR 24 2000

Two-stage magnetization reversal in exchange biased bilayers
Leighton, C; Fitzsimmons, MR; Yashar, P; Hoffmann, A; Nogues, J; Dura, J; Majkrzak, CF; Schuller, IK
PHYSICAL REVIEW LETTERS Volume: 86 Issue: 19 Pages: 4394-4397 Published: MAY 7 2001

Antiferromagnetic interlayer coupling in ferromagnetic semiconductor EuS/PbS(001) superlattices
Kepa, H; Kutner-Pielaszek, J; Blinowski, J; Twardowski, A; Majkrzak, CF; Story, T; Kacman, P; Galazka, RR; Ha, K; Swagten, HJM; De Jonge, WJM; Sipatov, AY; Volobuev, V; Giebultowicz, TM
EUROPHYSICS LETTERS Volume: 56 Issue: 1 Pages: 54-60 Published: OCT 2001

Interlayer spin coherence in antiferromagnetic EuTe/PbTe superlattices observed by polarized neutron diffraction
Nunez, V; Majkrzak, CF; Springholz, G; Bauer, G; Giebultowicz, TM; Kepa, H; Goldman, KI
SUPERLATTICES AND MICROSTRUCTURES Volume: 23 Issue: 1 Pages: 41-46 Published: 1998

Pinpointing chiral structures with front-back polarized neutron reflectometry
O'Donovan, KV; Borchers, JA; Majkrzak, CF; Hellwig, O; Fullerton, EE
PHYSICAL REVIEW LETTERS Volume: 88 Issue: 6 Article Number: 067201 Published: FEB 11 2002

Magnetic interactions in EuTe epitaxial layers and EuTe/PbTe superlattices
Kepa, H; Springholz, G; Giebultowicz, TM; Goldman, KI; Majkrzak, CF; Kacman, P; Blinowski, J; Holl, S; Krenn, H; Bauer, G
PHYSICAL REVIEW B Volume: 68 Issue: 2 Article Number: 024419 Published: JUL 1 2003

Magnetic-crystallographic phase diagram of the superconducting parent compound Fe1+x Te
Rodriguez, EE; Stock, C; Zajdel, P; Krycka, KL; Majkrzak, CF; Zavalij, P; Green, MA
PHYSICAL REVIEW B Volume: 84 Issue: 6 Article Number: 064403 Published: AUG 5 2011

Noncollinear spin-density-wave antiferromagnetism in FeAs
Rodriguez, EE; Stock, C; Krycka, KL; Majkrzak, CF; Zajdel, P; Kirshenbaum, K; Butch, NP; Saha, SR; Paglione, J; Green, MA
PHYSICAL REVIEW B Volume: 83 Issue: 13 Article Number: 134438 Published: APR 28 2011

Three-dimensional spatially resolved neutron diffraction from a disordered vortex lattice
Wang, X; Hanson, HA; Ling, XS; Majkrzak, CF; Maranville, BB
JOURNAL OF APPLIED CRYSTALLOGRAPHY Volume: 44 Pages: 414-417 Part: 2 Published: APR 2011

Structural evidence for an edge-contaminated vortex phase in a Nb crystal using neutron diffraction
Hanson, HA; Wang, X; Dimitrov, IK; Shi, J; Ling, XS; Maranville, BB; Majkrzak, CF; Laver, M; Keiderling, U; Russina, M
PHYSICAL REVIEW B Volume: 84 Issue: 1 Article Number: 014506 Published: JUL 20 2011

NEUTRON REFLECTIVITY STUDIES OF THE SURFACE-INDUCED ORDERING OF DIBLOCK COPOLYMER FILMS
ANASTASIADIS, SH; RUSSELL, TP; SATIJA, SK; MAJKRZAK, CF
PHYSICAL REVIEW LETTERS Volume: 62 Pages: 1852-1855 Published: APR 17 1989

WIDTH OF HOMOPOLYMER INTERFACES IN THE PRESENCE OF SYMMETRICAL DIBLOCK COPOLYMERS
RUSSELL, TP; MENELLE, A; HAMILTON, WA; SMITH, GS; SATIJA, SK; MAJKRZAK, CF
MACROMOLECULES Volume: 24 Issue: 20 Pages: 5721-5726 Published: SEP 30 1991

ORDERING OF THIN DIBLOCK COPOLYMER FILMS
MENELLE, A; RUSSELL, TP; ANASTASIADIS, SH; SATIJA, SK; MAJKRZAK, CF
PHYSICAL REVIEW LETTERS Volume: 68 Issue: 1 Pages: 67-70 Published: JAN 6 1992

HOMOPOLYMER DISTRIBUTIONS IN ORDERED BLOCK COPOLYMERS
MAYES, AM; RUSSELL, TP; SATIJA, SK; MAJKRZAK, CF
MACROMOLECULES Volume: 25 Issue: 24 Pages: 6523-6531 Published: NOV 23 1992

ENTROPY-DRIVEN SURFACE SEGREGATION IN BLOCK COPOLYMER MELTS
SIKKA, M; SINGH, N; KARIM, A; BATES, FS; SATIJA, SK; MAJKRZAK, CF
PHYSICAL REVIEW LETTERS Volume: 70 Issue: 3 Pages: 307-310 Published: JAN 18 1993

Internal Structure of Ultrathin Diblock Copolymer Brushes
Akgun, B; Ugur, G; Brittain, WJ; Majkrzak, CF; Li, XF; Wang, J; Li, HM; Wu, DT; Wang, Q; Foster, MD
MACROMOLECULES Volume: 42 Issue: 21 Pages: 8411-8422 Published: NOV 10 2009

Neutron reflectivity and atomic force microscopy studies of a lipid bilayer in water adsorbed to the surface of a silicon single crystal
Koenig, BW; Kruger, S; Orts, WJ; Majkrzak, CF; Berk, NF; Silverton, JV; Gawrisch, K
LANGMUIR Volume: 12 Issue: 5 Pages: 1343-1350 Published: MAR 6 1996

Neutron reflectivity studies of peptides in biomimetic bilayer membranes supported on planar substrates
Krueger, S; Plant, A; Meuse, K; Majkrzak, CF; Dura, J
BIOPHYSICAL JOURNAL Volume: 72 Issue: 2 Pages: WPME3-WPME3 Part: 2 Published: FEB 1997

Investigation of hybrid bilayer membranes with neutron reflectometry: Probing the interactions of melittin
Krueger, S; Meuse, CW; Majkrzak, CF; Dura, JA; Berk, NF; Tarek, M; Plant, AL
LANGMUIR Volume: 17 Issue: 2 Pages: 511-521 Published: JAN 23 2001

Hybrid bilayer membranes in air and water: Infrared spectroscopy and neutron reflectivity studies
Meuse, CW; Krueger, S; Majkrzak, CF; Dura, JA; Fu, J; Connor, JT; Plant, AL
BIOPHYSICAL JOURNAL Volume: 74 Issue: 3 Pages: 1388-1398 Published: MAR 1998

Hydration state of a single cytochrome c monolayer vectorially oriented at a soft interface investigated by neutron interferometry
Kneller, LR; Edwards, AM; Majkrzak, CF;Berk, NF; Krueger, S; Blasie, JK
BIOPHYSICAL JOURNAL Volume: 76 Issue: 1 Pages: A219-A219 Part: 2 Published: JAN 1999

Hydration state of single cytochrome c monolayers on soft interfaces via neutron interferometry
Kneller, LR; Edwards, AM; Nordgren, CE; Blasie, JK; Berk, NF; Krueger, S; Majkrzak, CF
BIOPHYSICAL JOURNAL Volume: 80 Issue: 5 Pages: 2248-2261 Published: MAY 2001

Characterization of a biomimetic polymeric lipid bilayer by phase sensitive neutron reflectometry
Perez-Salas, UA; Faucher, KM; Majkrzak, CF; Berk, NF; Krueger, S; Chaikof, EL
LANGMUIR Volume: 19 Issue: 19 Pages: 7688-7694 DOI: 10.1021/la034607f Published: SEP 16 2003

Neutron diffraction and MD simulation in conjunction for determining lipid bilayer structure
Mihailescu, M; Castro-Roman, F; White, S; Worcester, D; Majkrzak, C
BIOPHYSICAL JOURNAL Volume: 88 Issue: 1 Pages: 243A-243A Supplement: S Part: 2 Published: JAN 2005

pH-dependent conformational changes and insertion of diphtheria toxin adsorbed to lipid membranes by neutron and X-ray reflection
Kent, MS; Kim, H; Murton, J; Satija, S; McGillivray, D; Majkrzak, C; Heinrich, F; Majewski, J; Loesche, M
BIOPHYSICAL JOURNAL Pages: 587A-587A Supplement: S Published: JAN 2007

Monitoring the assembly of antibody-binding membrane protein arrays using polarised neutron reflection
Le Brun, AP; Holt, SA; Shah, DS; Majkrzak, CF; Lakey, JH
EUROPEAN BIOPHYSICS JOURNAL WITH BIOPHYSICS LETTERS Volume: 37 Issue: 5 Pages: 639-645 Published: JUN 2008

An ion-channel-containing model membrane: structural determination by magnetic contrast neutron reflectometry
Holt, SA; Le Brun, AP; Majkrzak, CF; McGillivray, DJ; Heinrich, F; Losche, M; Lakey, JH
SOFT MATTER Volume: 5 Issue: 13 Pages: 2576-2586 Published: 2009

The structural orientation of antibody layers bound to engineered biosensor surfaces
Le Brun, AP; Holt, SA; Shah, DSH; Majkrzak, CF; Lakey, JH
BIOMATERIALS Volume: 32 Issue: 12 Pages: 3303-3311 Published: APR 2011

Anesthetic Concentrations of Halothane Change the Domain Structure of Mixed Lipid Membranes
Nanda, H; Weinrich, M; Majkrzak, CF; Maranville, BB; Worcester, DL; Bezrukov, SM
BIOPHYSICAL JOURNAL Volume: 102 Issue: 3 Pages: 288A-288A Supplement: 1 Published: JAN 31 2012

Halothane Changes the Domain Structure of a Binary Lipid Membrane
Weinrich, M; Nanda, H; Worcester, DL; Majkrzak, CF; Maranville, BB; Bezrukov, SM
LANGMUIR Volume: 28 Issue: 10 Pages: 4723-4728 Published: MAR 13 2012

Enhancing the platinum atomic layer deposition infiltration depth inside anodic alumina nanoporous membrane
Vaish, A; Krueger, S; Dimitriou, M; Majkrzak, C; Vanderah, DJ; Chen, L; Gawrisch, K
JOURNAL OF VAC SCIENCE & TECH A Volume: 33 Issue: 1 Article Number: 01A148 Published: JAN 2015

NEUTRON REFLECTOMETRY STUDIES OF SURFACE OXIDATION
WIESLER, DG; MAJKRZAK, CF
PHYSICA B Volume: 198 Issue: 1-3 Pages: 181-186 Published: APR 1994

Water Uptake and Interfacial Structural Changes of Thin Film Nafion (R) Membranes Measured by Neutron Reflectivity for PEM Fuel Cells
Murthi, VS; Dura, JA; Satija, S; Majkrzak, CF
Edited by: Fuller T et al. PROTON EXCHANGE MEMBRANE FUEL CELLS 8, PTS 1 AND 2
Book Series: ECS Transactions Volume: 16 Issue: 2 Pages: 1471-1485 Published: 2008

Multilamellar Interface Structures in Nafion
Dura, JA; Murthi, VS; Hartman, M; Satija, SK; Majkrzak, CF
MACROMOLECULES Volume: 42 Issue: 13 Pages: 4769-4774 Published: JUL 14 2009

Nanoparticle concentration profile in polymer-based solar cells
Kiel, JW; Kirby, BJ; Majkrzak, CF; Maranville, BB; Mackay, ME
SOFT MATTER Volume: 6 Issue: 3 Pages: 641-646 Published: 2010

Phase-sensitive neutron reflectometry measurements applied in the study of photovoltaic films
Kiel, JW; Mackay, ME; Kirby, BJ; Maranville, BB; Majkrzak, CF
JOURNAL OF CHEMICAL PHYSICS Volume: 133 Issue: 7 Article Number: 074902
Published: AUG 21 2010

NIST Center for Neutr... x +

https://www.ncnr.nist.gov

Most Visited Release Notes Fedora Project Red Hat Free Content Sign out

NIST Center for Neutron Research

-- a national resource for industry, universities, and government agencies

Coming to the NCNR? Click Here.
Visa question?

Logon to your NCNR-IMS account

NCNR SiteMap

About the NCNR
What We Do
Informal History
Staff
Annual Report
2017 Summer School
June 19-June 23, 2017
Working at the NCNR
See differently with neutrons at NIST (video)

Facility Information
Live Data
Instrumentation
Instrument Contacts
Schedules
Center for High Resolution Neutron Scattering (CHRNS)
>Education and Outreach
Sample Environment
NCNR Staff Forms
Sample Prep Labs

User Information
Planning Your Experiment
Obtaining BeamTime
Data Reduction/Analysis
Shipping Samples
Publishing Your Results
Financial Assistance
Travel & Lodging
NCNR User Group

Other Sites
Neutron Sources
Photon Sources
Postdoctoral Opportunities
Societies & Organizations

CHRNS — *Maximizing access for the scientific community to transformative neutron scattering instrumentation*

nSoft — *A consortium for the advancement of neutron-based measurements for manufacturing of soft materials*

RECENT RESEARCH HIGHLIGHTS

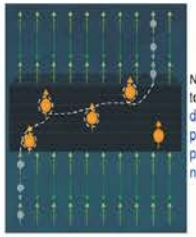

NIST collaboration heats up exotic topological insulators
details
paper in Nature Materials
press release (UCLA)
news item in IEEE Spectrum

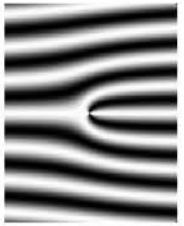

Move over, lasers: scientists can now create holograms from neutrons, too
details
paper in Optics Express
news item in Physics Today

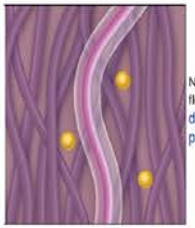

Nanoparticles can make polymers flow more easily
details
paper in Physical Review Letters

https://www.ncnr.nist.gov

NIST CENTER FOR NEUTRON RESEARCH

NCNR-IMS Login | Facility Information | User Information | CHRNS | News | About NCNR

Surfaces and Interfaces Team

Neutron Reflectometry

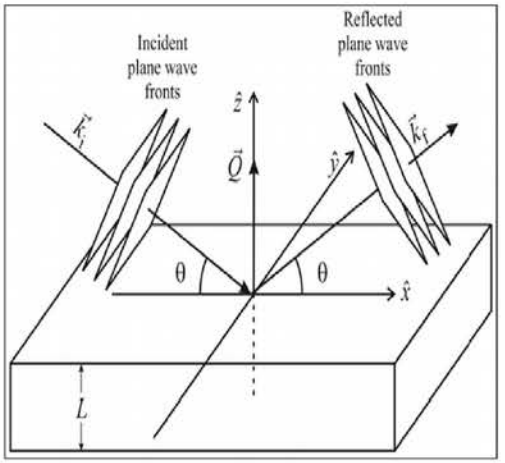

Reflectometry uses neutrons scattered at grazing angles to probe the nuclear and magnetic composition of flat samples. Common types of materials studied include biological membranes, magnetic multilayers, and polymer films. The NCNR currently operates three reflectometers - PBR, MAGIK, and NG-7 - each specially configured for different types of research. Additionally, construction is underway on CANDOR, a revolutionary new white beam reflectometer. Please visit the instrument pages (linked at right) for specific information.

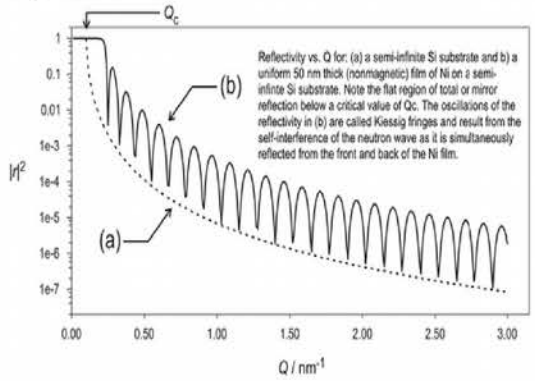

Reflectometers

- PBR - Magnetism
- MAGIK - Offspecular Capability
- NG7 - Horizontal Geometry
- CANDOR - White Beam

Data Analysis

- Online data reduction
- Raw data file explorer
- SLD Calculator
- Scatterer's Periodic Table
- Refl1D Model Fitting (Windows)
- Refl1D Model Fitting (Mac)

Reference Material

- Theory of PNR
- NR Summer School Lecture
- PNR Summer School Lecture
- PNR and Magnetic Materials
- Pynn Neutron Primer

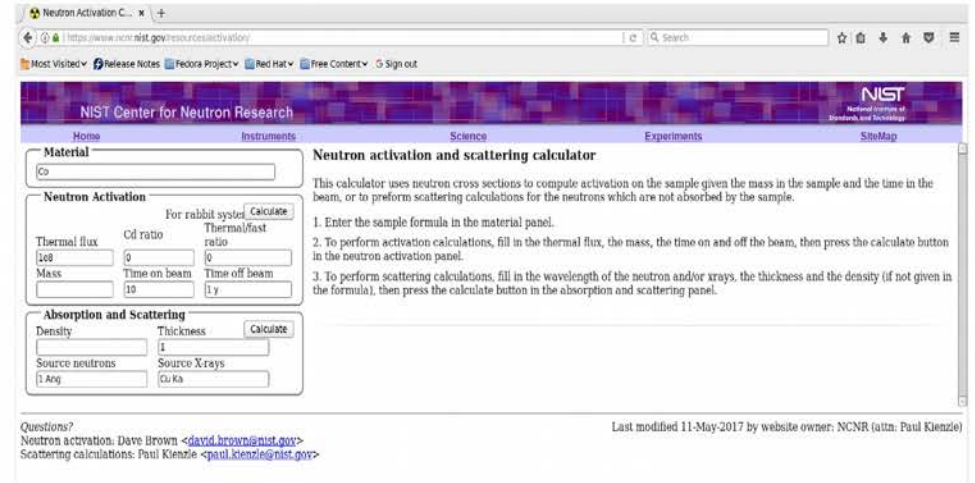

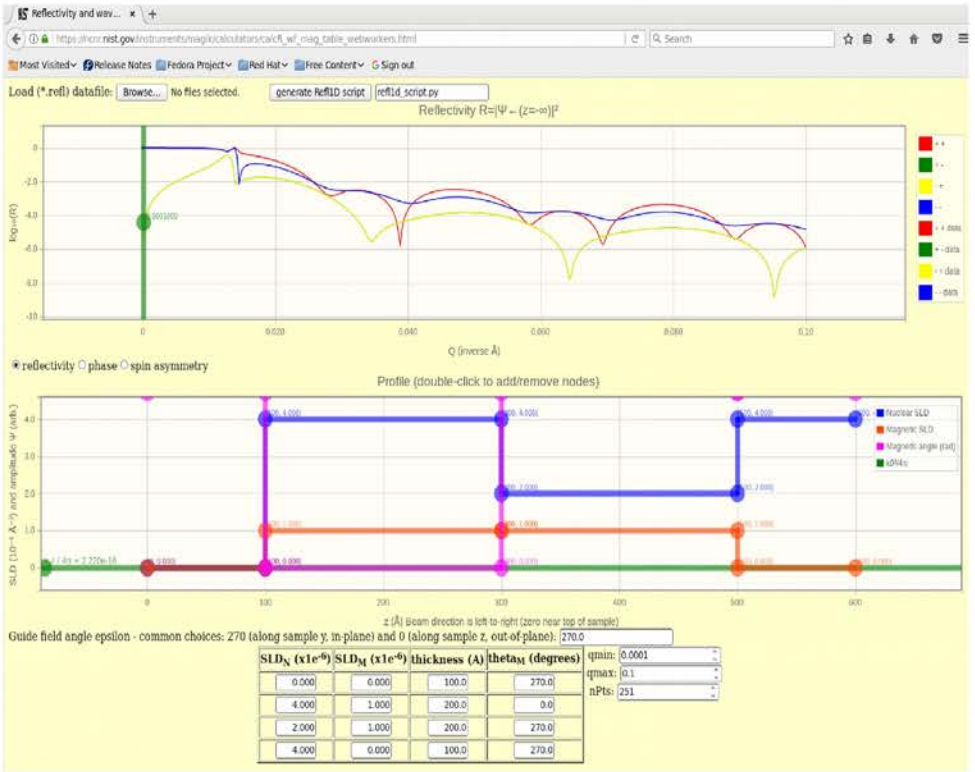

On-line programs for calculating scattering length densities and specular neutron reflectivity – fitting programs are also available. (Developed and maintained by NCNR staff, particularly Brian Maranville and Paul Kienzle.)

Volume 122 (2017) https://doi.org/10.6028/jres.122.034
Journal of Research of National Institute of Standards and Technology

Interactive, Web-Based Calculator of Neutron and X-ray Reflectivity

Brian B. Maranville

National Institute of Standards and Technology,
Gaithersburg, MD 20899, USA

brian.maranville@nist.gov

Software DOI: https://doi.org/10.18434/M3QG67

Software Version: 1.0

Key words: calculator; neutron; reflectivity; scattering.

Accepted: June 30, 2017

Published: July 12, 2017

https://doi.org/10.6028/jres.122.034

1. Summary

For many users of the neutron and X-ray reflectometry instruments at NIST, these measurements represent a relatively small and specialized part of their research portfolio. As such, providing calculation and modeling tools that are as accessible and easy-to-use as possible is a high priority of the facility. In order to meet this need, a purely web-browser-based calculator for reflectivity modeling and rudimentary fitting has been developed and provided on a publicly accessible web server.

Going to https://www.ncnr.nist.gov/instruments/magik/calculators/reflectivity-calculator.html, will load a one-page web application into the browser. Any relatively modern browser with support for ECMAScript 5 will be able to load and run the application. A calculator for magnetic samples can be found at https://www.ncnr.nist.gov/instruments/magik/calculators/magnetic-reflectivity-calculator.html.

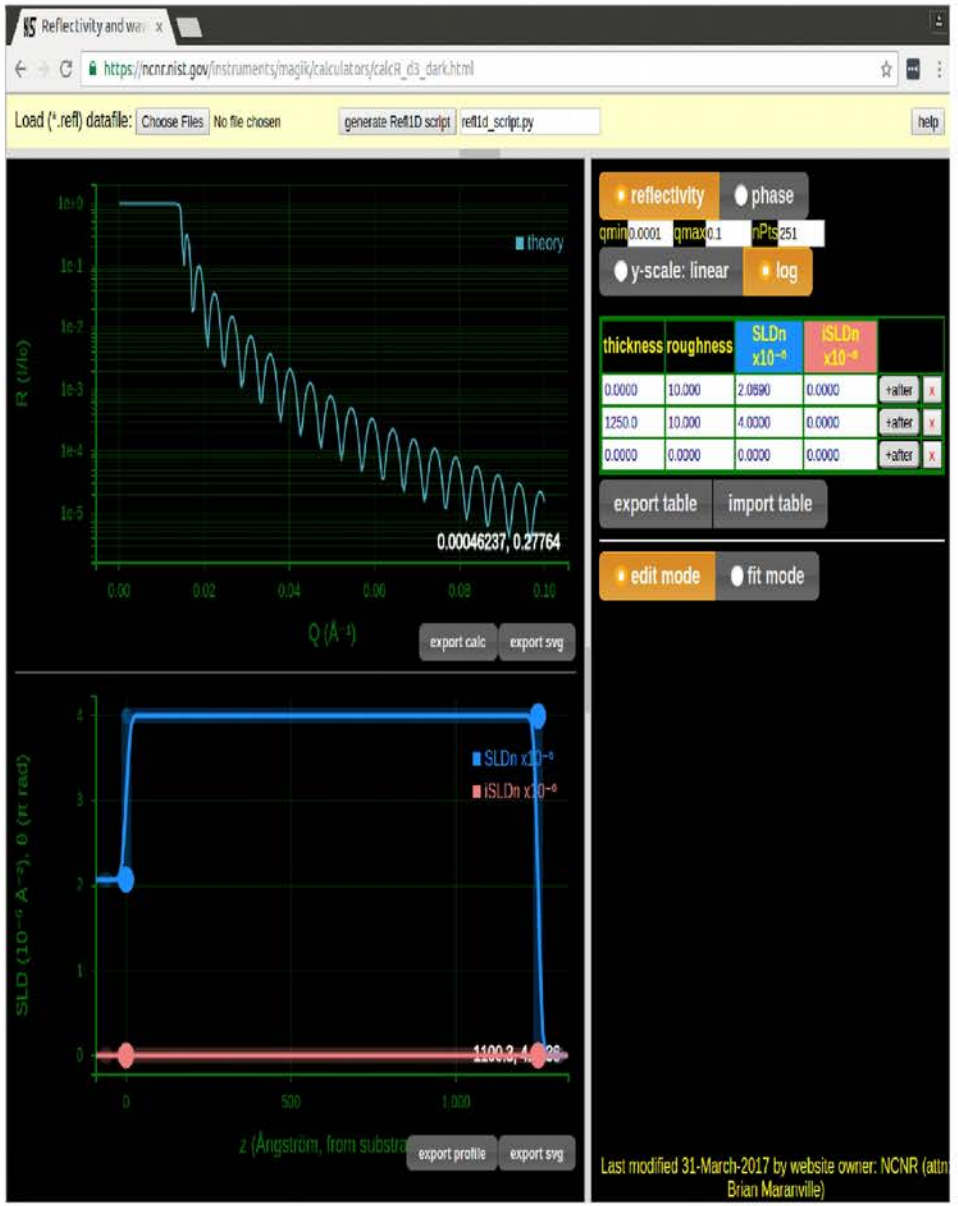

Fig. 1. Screenshot of non-magnetic reflectivity calculator.

Volume 122 (2017) https://doi.org/10.6028/jres.122.034
Journal of Research of National Institute of Standards and Technology

Fig. 2. Screenshot of magnetic reflectivity calculator.

Bibliography / References

Optics, 3rd Ed., by E. Hecht, Addison-Wesley, 1998.

Neutron Optics, by V.F. Sears, Oxford University Press, 1989.

Principles of Optics, 6th Ed., by M. Born and E. Wolf,
Pergamon Press, 1987.

Quantum Mechanics, 2nd Ed., by E. Merzbacher, Wiley, 1970.

“Structural Investigations of Membranes in Biology by Neutron Reflectometry”, C.F.Majkrzak, N.F.Berk, S.Krueger, and U.A.Perez-Salas, Chapter 12 in *Neutron Scattering in Biology*, Edited by J.Fitter, T.Gutberlet, and J.Katsaras, (Springer, Berlin, 2006) p.225-263.

“Polarized Neutron Reflectometry”, C.F.Majkrzak, K.V.O'Donovan, and N.F.Berk, Chapter 9 in *Neutron Scattering from Magnetic Materials*, Edited by T.Chatterji, (Elsevier, Amsterdam, 2006) p.397-471.

“Phase-Sensitive Neutron Reflectometry”, C.F.Majkrzak, N.F.Berk, and U.A.Perez-Salas,
Langmuir **19**, 7796 – 7810 (2003).

B.J.Kirby et al., Phase-sensitive specular neutron reflectometry . . .,
Current Opinion in Colloid & Interface Science **17** (2012) 44-53.

C.F.Majkrzak et al., *J. Appl. Phys.* **110** (2011).

www.ncnr.nist.gov -- look here for information about neutron reflectometry in general as well as in specific studies highlighted in past and current annual reports for the facility.